



Design, Optimization and Comparison of Permanent Magnet Motors for a Low-Speed Direct-Driven Mixer

Florence Libert

ROYAL INSTITUTE OF TECHNOLOGY
DEPARTMENT OF ELECTRICAL ENGINEERING
ELECTRICAL MACHINES AND POWER ELECTRONICS

Stockholm 2004

Submitted to the School of Computer Science, Electrical Engineering and Engineering Physics, KTH, in partial fulfilment of the requirements for the degree of Technical Licentiate.

Copyright © Florence Libert, Sweden 2004

Printed in Sweden

Universitetsservice US AB

TRITA-ETS-2004-12

ISSN 1650-674X

ISRN KTH/R-0412-SE

ISBN 91-7283-901-5

Abstract

Induction motors are commonly coupled to a gearbox when an application requires a low speed and a high torque. The gearbox is costly, needs maintenance and decreases the efficiency of the drive. Therefore, taking away the gearbox is very advantageous. This can be made possible by using a permanent magnet (PM) synchronous motor running directly at low speed, so called direct-drive PM synchronous motor.

In this thesis, low-speed direct-drive PM motors are investigated for a 4.4 kW, 50 rpm mixer used for wastewater treatment. The thesis begins with an overview of different existing low-speed direct-driven applications. It concentrates then on a few topologies that are promising for the considered application: five different radial-flux PM machine configurations with surface-mounted or buried permanent magnets and two Torus axial-flux PM machine configurations.

The designs of the PM machines are conducted by solving an optimization problem. The goal is to minimize the active weight of the machine, while fulfilling the requirements on the outer dimensions, the efficiency and the cost. The design process, based on analytical calculations as well as finite-element simulations, is described taking the particularities of each topology into account.

Designs of low-speed radial-flux PM machines with high pole numbers are first calculated with conventional distributed windings and one slot per pole per phase. The results obtained for different PM machine configurations are compared. To improve further the designs, concentrated windings are investigated for PM machines with high pole numbers. Concentrated winding layouts offering high winding factors and limiting the rotor losses

as well as the noise and vibrations of the machine are identified and sorted out. Some interesting concentrated winding layouts are combined with the different radial-flux PM machine configurations and further investigated with FEM simulations.

The design of axial-flux PM motors is treated separately in the thesis. It was found that the Torus axial-flux PM machines are not satisfying the requirements of the application. Therefore multi-disk axial-flux PM machines are investigated.

Finally, the investigated theoretical designs suitable for the application are compared and their advantages and drawbacks are emphasized.

Acknowledgments

The work presented in this thesis has been carried out at the division of Electrical Machines and Power Electronics (EME), Department of Electrical Engineering (ETS), Royal Institute of Technology (KTH). It is an ongoing project within the Permanent Magnet Drives (PMD) research program of the Competence Centre in Electric Power Engineering. As one of the pilot projects within PMD, the main objective is to investigate and develop new concepts of electrical drives in close cooperation with industrial partners. The main industrial partner involved in this project is ITT Flygt.

Since I started to work on my Ph.D., several people have been involved in the project. Hereby, I kindly acknowledge them.

I thank first of all my project leader, Dr. Juliette Soulard, for her guidance, support, enthusiasm and trust. I thank also to Dr. Jörgen Engström from ITT Flygt, for following the project, helping and making useful suggestions. I am also very grateful to my supervisor, Prof. Chandur Sadarangani for his friendly approach in our discussions throughout the project.

Besides my leaders and supervisor, there are many people that helped me with my work:

I thank the staff of ITT Flygt, especially Jürgen Mökander, Ulf Carlsson, Dr. Lars Uby and Gert Hallgren for their help on questions dealing with the mixer.

I thank Dr. Thomas Bäckström, Freddy Magnussen, Prof. Hans-Peter Nee, Tech. Lic. Mats Leksell, Tech. Lic. Maddalena Cirani and Dr. Peter Thelin, for interesting discussions.

Two persons were of great help during this project. The first one is Stephan Meier. I began my project using some parts of his master thesis work. Stephan also critically read the thesis and made it easier to read for non French speakers. The second is Tech. Lic. Robert Chin, who always succeeds giving an interesting answer to my sometimes tricky questions. Many thanks!

I am grateful to Peter Lönn, who was helping me with my various computer problems, so stupid they could be sometimes.

I might not have started this work if the working environment at EME were not so great. Therefore, I would like to thank the whole personal at EME as well as the former employees for contributing to make EME as it is.

Special thanks to Maddalena, Ruslan, Stefan and Sylvain for their friendship.

Very special thanks to my office-mate Robert, my boyfriend's office-mate Karsten, and to my across-the-corridor office-neighbor Eva. They are always friendly, cheerful and "cool"...

Thanks a lot to my parents for your support and care. Sorry if you do not always understand or know what I am doing here (mais je travaille, recherche, et trouve... un petit-ami ;o)

Finally, I would like to thank again my "sambo" Stephan for his help, support and love...

Florence Libot

Stockholm,
November 2004

Contents

1	Introduction	1
1.1	Permanent magnet synchronous machines	1
1.2	Low-speed direct-drive applications	1
1.3	The project application: The banana-blade mixer	2
1.4	Goal of the project	4
1.5	Content of the thesis	5
2	PM machines for low-speed direct drives	7
2.1	Radial-flux PM synchronous machine	7
2.1.1	Surface-mounted PM machines with inner rotor	8
2.1.2	Surface-mounted PM machines with outer rotor	9
2.1.3	Inset PM machines	10
2.1.4	Buried PM machines	10
2.2	Axial-flux PM machines	13
2.3	Transverse-flux PM machines	15
2.4	Line-Start PM, modular PM and induction PM machines . .	16
2.4.1	Line-Start PM machines	16
2.4.2	Modular PM machines for variable speed operation . .	17
2.4.3	Induction PM machines	18
2.5	The investigated motor configurations	19
3	Properties of low-speed radial-flux PM motors	21
3.1	Geometrical properties: Dimensions of the motors	21
3.1.1	Inner-rotor SMPM motors and inset PM motors	22
3.1.2	Outer-rotor SMPM motors	23
3.1.3	Buried PM motors	24
3.2	Magnetic properties	24
3.2.1	Analytical calculation of the flux density in the airgap	24
3.2.2	Analytical calculation of the flux density in the teeth .	33
3.3	Electrical properties	34

3.3.1	Inductances	35
3.3.2	Resistance of one phase of the stator winding	36
3.3.3	The external voltage	37
3.3.4	Induced voltage	37
3.3.5	Ampere-turns per slot	38
3.3.6	Angle β	39
3.3.7	Number of conductors per slot	41
3.4	Summary	42
4	Optimization procedure and comparison of designs with distributed windings	43
4.1	The design procedure	43
4.1.1	Objective function	45
4.1.2	Design variables and their ranges	45
4.1.3	Given constants	47
4.1.4	Constraints	48
4.2	Results and comparison of designs with distributed windings	50
4.2.1	Influence of some of the constraints	50
4.3	Comparison of the configurations	52
4.3.1	Weight and pole number	53
4.3.2	Torque ripple	56
4.3.3	Iron losses	60
4.3.4	Summary	60
5	Concentrated windings	61
5.1	Irregularly distributed teeth	62
5.1.1	Winding factor	62
5.1.2	Influence on the torque ripple	64
5.2	Combinations of pole and slot numbers	64
5.2.1	Winding layouts and winding factors	65
5.2.2	MMF and harmonics	73
5.2.3	Torque ripple	74
5.2.4	Magnetic noise	77
5.3	Summary	79

6	Results and comparison of designs with concentrated windings	81
6.1	SMPM motors	82
6.2	Outer-rotor SMPM motors	85
6.3	Tangentially-magnetized PM motors	88
6.4	Choice of a design	91
6.5	Conclusions	91
7	Design and results of axial-flux PM motors	93
7.1	Main features of the Torus AFPM motor	93
7.1.1	Dimensions of the motor	93
7.1.2	Flux densities	95
7.1.3	Windings	97
7.2	Design	99
7.2.1	The design procedure	99
7.2.2	The design constraints	101
7.3	Results	102
7.3.1	Torus AFPM machine	102
7.3.2	Multi-disk Torus AFPM machine	103
7.3.3	Comparison with the investigated RFPM motors . . .	106
7.4	Summary	107
8	Conclusions and future work	109
8.1	Conclusions	109
8.2	Suggestions for future work	110
	Bibliography	111
	Glossary of symbols and acronyms	117
A	Direct-driven machines manufacturers	121
A.1	Wind turbines	121
A.2	Other applications	121
B	Finite element methods simulations	123
B.1	2D-FEM simulations	123
B.2	3D-FEM simulations	125

C Optimization	127
C.1 A simple example	127
C.2 Optimization program for the motor design	127
C.2.1 How to deal with the integer variables	128
C.2.2 How to deal with the non-linearities	129
D Thermal study	131

1 Introduction

1.1 Permanent magnet synchronous machines

Nowadays, electrical motors account for 65 % of the worldwide energy consumption. As environmental concern increases, electrical drives with higher efficiency are desirable. Thus, replacing conventional induction machines with Permanent Magnet (PM) synchronous machines has recently gained great interest, as the price of PM materials decreases. Indeed, PM machines have no rotor winding resulting in lower copper losses, and therefore they feature a higher efficiency than the induction machines.

For low-speed applications, below 500 rpm, PM machines may further eliminate the need of a gearbox. To adapt the speed and torque of the machine, a gearbox is traditionally coupled to a standard induction machine. It is advantageous to take away this mechanical element, because it is costly, decreases the drive efficiency and needs maintenance. Low-speed (or high-speed) drives without gearbox are called direct drives, since the machines are directly coupled to the load.

1.2 Low-speed direct-drive applications

Today, low-speed PM direct drives are mostly used for two applications, wind turbines and boat propulsion (figure 1.1). Direct drives for wind turbine generators are widely studied [1], [2], [3], [4], [5], [6]. For wind turbines, a direct-drive generator makes it possible to avoid the noisy gearbox and to reduce the travels aimed to oil the gearbox of remote turbines. Some manufacturers already produce wind turbines with direct-drive generators, such as Lagerwey, Jeumont Industry or Enercon (appendix A).

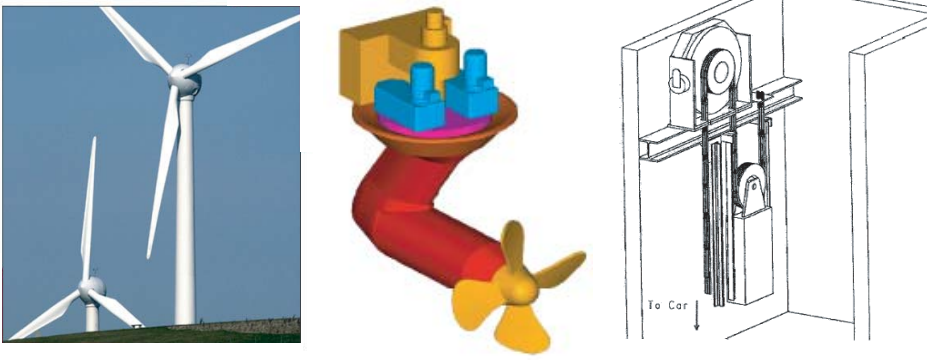


Figure 1.1: Some direct-drive applications: Wind turbines from Jeumont Industry, ABB's Azipod for boat propulsion (appendix A) and Kone's elevator without machine room [7].

For boat propulsion, direct drives offer the possibility of light pods that contain the motor and are easy to maneuver [8], [9]. Direct drives are also successfully used for elevators [7], [10], where they make it possible to get rid of the whole machine room. More detailed examples of direct-drive applications are given in chapter 2, and some low-speed direct-drive manufacturers are listed in appendix A.

1.3 The project application: The banana-blade mixer

In this thesis, the work will mainly focus on a mixer from ITT Flygt. Their banana-blade mixer is used in wastewater treatment plants to stir big volumes of liquid. The mixer is driven by an induction motor coupled to a gearbox (figure 1.2). It runs at 50 rpm, 4.4 kW. Its total weight is 245 kg, where the propeller accounts for 92 kg and the motor for 22 kg. The characteristics of the two-pole motor are given in table 1.1. The gearbox has an efficiency of around 90 % at 4 kW, which decreases to 80-85 % at lower power (1.5 kW).

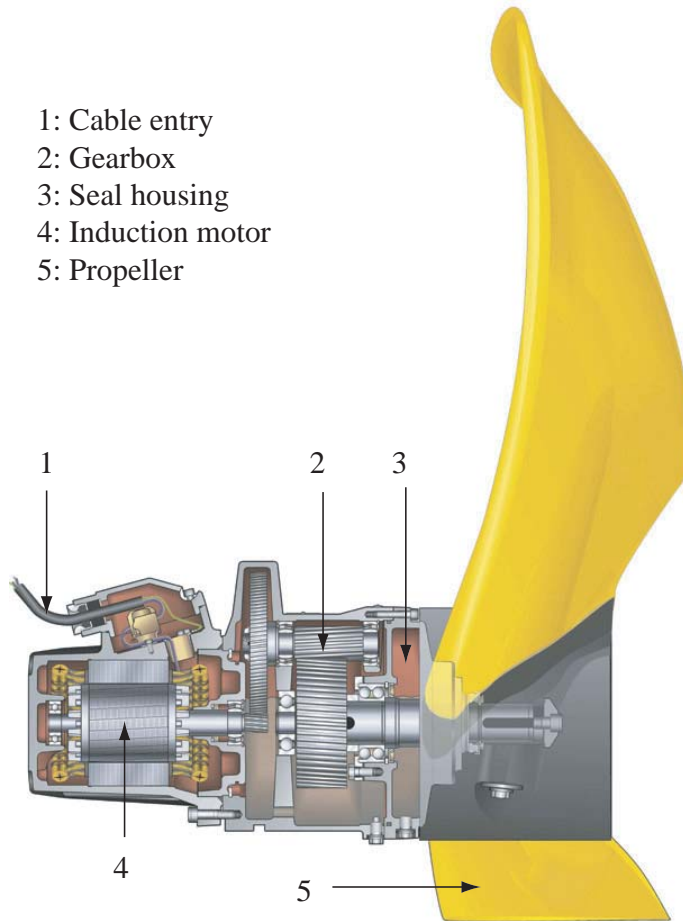


Figure 1.2: ITT Flygt's banana-blade mixer [11].

Table 1.1: Characteristics of the 2-pole induction motor.

Length	95 mm
Outer diameter	180 mm
Bore diameter	94 mm
Weight	22 kg
Power factor	0.92
Efficiency	81 %
Nominal current	8.6 A
Voltage	400 V
Frequency	50 Hz

1.4 Goal of the project

The goal of the project is to define suitable PM drives for low-speed applications to replace induction drives with gearbox (figure 1.3). The focus will be on the banana-blade mixer described previously. The PM solution should compete with the induction motor and its gearbox. It should also fulfill the specifications described in table 1.2 and have a competitive price. Most PM motors are synchronous so they require to be inverter-fed to be able to start when connected. The presence of the inverter allows variable speed that may lead to large improvements of the total efficiency of the mixer.

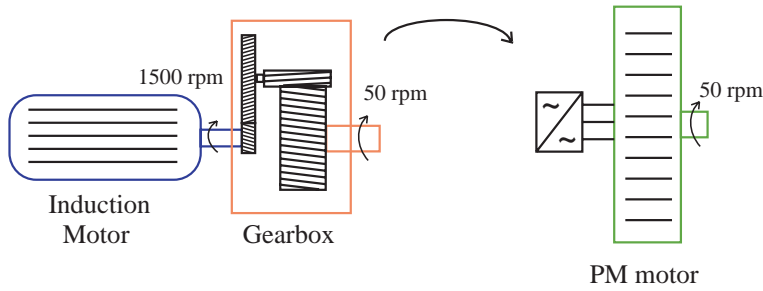


Figure 1.3: Description of the targeted PM drive.

Table 1.2: Design specifications of the direct-drive system.

Maximum outer diameter	500 mm
Maximum length	500 mm
Maximum weight	150 kg
Minimum efficiency	73 %
Nominal torque	840 Nm
Nominal speed	50 rpm

The maximum outer stator diameter is chosen so that it does not exceed 20 % of the mixer's propeller diameter. Thus, the motor does not disturb the fluid behavior near the mixer's blades. The maximum length should not exceed the length of the induction motor and the gearbox.

1.5 Content of the thesis

A low-speed PM motor features many poles, which makes its design unconventional. Already the choice of the number of poles is a challenge. The design procedure should then make it possible to find the number of poles that gives the best design. The choice of the winding type is also an important issue. Therefore a whole chapter is dedicated to concentrated windings for low-speed PM machines. Finally, the design of axial-flux PM motors is treated separately due to the important differences with the designs of radial-flux machines.

Different topologies of PM machines are adapted for low-speed direct drives. They are described in chapter 2 with their advantages and drawbacks. An overview of investigations, prototypes, and existing products that use direct drives is presented as well.

Chapter 3 deals with the geometrical, magnetic and electric properties of low-speed PM motors. The geometrical structures of the different motor designs are first described. Then the focus is on the calculation of the flux density in the airgap and teeth, which depends on the rotor configuration. Finally some details on the calculations of motor inductances and number of conductors are given. The influence of the saliency of the motor is emphasized.

In chapter 4, the design procedure for the radial-flux PM machines is described. It is based on an optimization program that is first explained. Then some results obtained by running the design procedure are provided. They allow a comparison between the different investigated configurations.

The concentrated windings for low-speed high-pole number PM machines are investigated in chapter 5. Indeed, these windings could improve the designs. The drawbacks of concentrated windings are also studied.

In chapter 6, the optimized designs with concentrated windings are presented and compared to each other and to the designs with distributed windings.

Chapter 7 deals with axial-flux PM machines. The design procedure and the results are presented and compared with the characteristics of the radial-flux PM machines from chapter 6.

The main results from this design study of PM direct drives for the banana-blade mixer are given in chapter 8. At the end of the thesis, the possible future work is presented.

2 PM machines for low-speed direct drives

In this chapter, the different PM machines that are suitable for low-speed direct-drive applications are presented. Each configuration is shortly described and its advantages and drawbacks are emphasized. Examples of both academic work and industrial applications are provided.

2.1 Radial-flux PM synchronous machine

Radial-flux PM synchronous machines (RFPM) are the most conventional PM machines. They are widely used for direct-drive applications.

Figure 2.1 shows two views of a RFPM machine with the direction of the flux and current flows. The flux flows radially in the machine while the current flows in the axial direction.

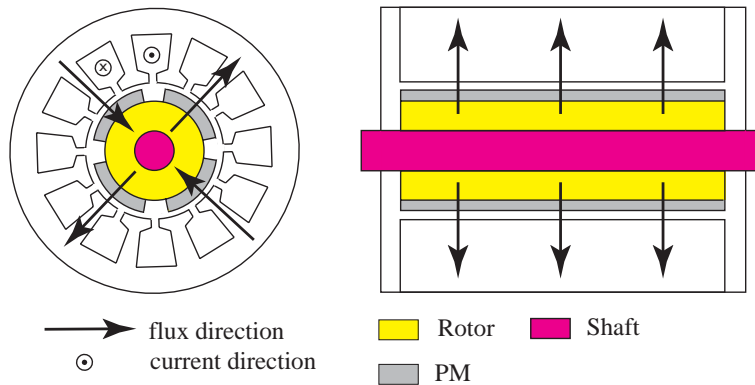


Figure 2.1: RFPM machine with flux and current flows.

RFPM machines are the easiest and cheapest to manufacture among the PM machines, as they are the most commonly used and their stators are similar to the ones of the induction machines. However, they are much bigger than the axial-flux and transverse flux machines in terms of active weight and axial length [12]. Different possible configurations of RFPM are described below.

2.1.1 Surface-mounted PM machines with inner rotor

For these machines, the permanent magnets are placed on the rotor surface, as shown in figure 2.2. This is the most commonly used configuration.

The main advantage of the Surface-Mounted PM (SMPM) machine is its simplicity and consequently its lower construction cost compared to other PM machines. The main drawback is the exposition of the permanent magnets to demagnetisation fields. Furthermore, the magnets are subject to centrifugal forces that can cause their detachment from the rotor. However, as these forces increase with the rotational speed, they are low in the studied low-speed applications.

The main direct-drive application of the inner-rotor SMPM machine is ship propulsion, as the shape of the machine (small diameter, large length) fits to the pod requirements [13], [14]. SMPM generators have also been used in the first direct-driven wind turbines [15], [16].

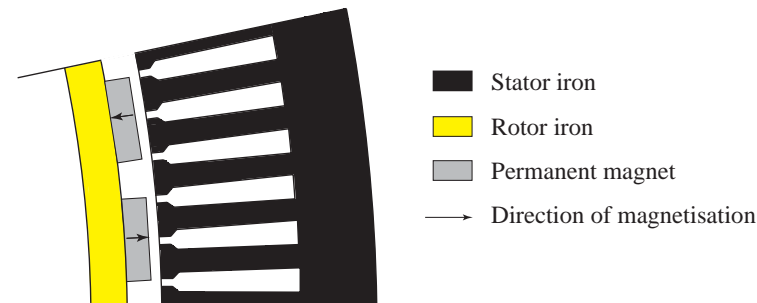


Figure 2.2: Cross-section of a surface-mounted PM motor with inner rotor (one pole pair).

2.1.2 Surface-mounted PM machines with outer rotor

The machine consists of a stationary wound stator located in the centre of the machine while the magnets are mounted along the inner circumference of the rotor (figure 2.3).

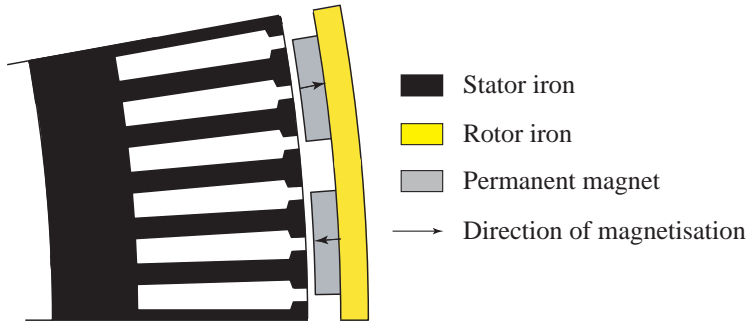


Figure 2.3: Cross-section of a surface-mounted PM motor with outer rotor (one pole pair).

Some advantages of this configuration are:

- The rotor diameter is larger than for conventional radial-flux machines, which allows a higher number of poles.
- During the rotation of the outer rotor, the centrifugal forces exert a pressure on the permanent magnets making their detachment more improbable.
- The structure is well adapted to wind turbines, as the hub carrying the blades can be fixed directly to the outer rotor.

This type of machine has been studied by J. Chen and W. Wu and two prototypes of 20 kW, with 36 and 48 poles respectively were constructed [6], [17], [18]. Outer-rotor generators are commonly used in small wind turbines (up to 30 kW), like for example the 7.5 kW turbine of Bergey, the turbines from Westwind or from Genesys (refer to appendix A).

2.1.3 Inset PM machines

As the SMPM machines, the inset PM machines have permanent magnets mounted on the rotor surface. However, the gaps between the permanent magnets are partially filled with iron, as shown in figure 2.4. This configuration is referred to as inset PM machine. The iron between the permanent magnets creates a saliency and gives a reluctance torque in addition to the torque from the magnets. No example of inset PM machine for low-speed direct-drive applications was found. Therefore it will be of interest to study the influence of the reluctance torque on the performance of the machine and to compare it to the SMPM machine designs.

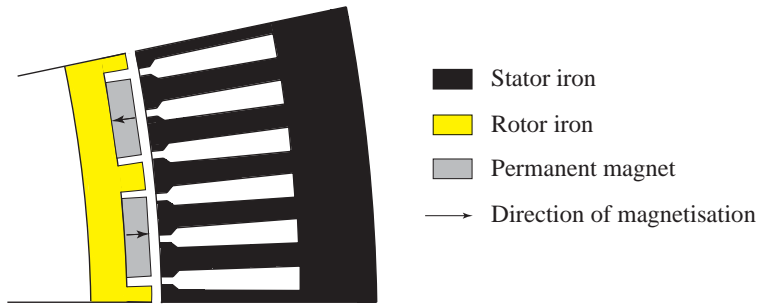


Figure 2.4: Cross-section of an inset PM motor (one pole pair).

2.1.4 Buried PM machines

Another way to place the permanent magnets in the rotor is to bury them inside the rotor lamination. An advantage of the buried PM machine configurations compared to the surface PM machines is the possibility to concentrate the flux generated by the permanent magnets in the rotor and thus achieve high airgap flux densities. Moreover, the buried permanent magnets are well protected against demagnetisation and mechanical stress.

Many different possibilities for the placement of the permanent magnets in the rotor are conceivable, but this thesis concentrates on the two configurations described below.

V-shaped permanent magnets

In this configuration (figure 2.5), two permanent magnets per pole are placed in a certain angle taking the form of a "V". Between the ends of the V-shaped permanent magnets and the airgap, there are two iron bridges.

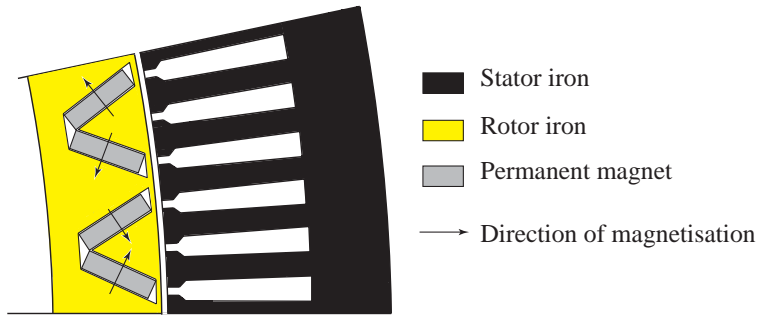


Figure 2.5: Cross-section of a V-shaped buried PM motor (one pole pair).

The main drawback of rotors with V-shaped PMs is the presence of the iron bridges. The minimal thickness of the bridges being fixed by mechanical constraints, a large part of the permanent magnet flux leaks through these bridges instead of crossing the airgap and contributing to the torque. Besides, the V-shaped rotor is not very easily adapted for high pole numbers: the higher the pole number, the smaller the place available for the permanent magnets and the smaller the angle between the two V-shaped magnets. Therefore, the iron between the permanent magnets can easily get saturated if the angle is too little. Another drawback of the V-shaped PM configuration is the high number of permanent magnets, which increases the production cost.

Such machines were studied in [19], where a 45 kW, 600 rpm synchronous motor with V-shaped PMs was constructed for an application in the pulp and paper industry.

Tangentially-magnetized permanent magnets

In this second buried PM configuration (figure 2.6), referred to as tangentially-magnetized PM, the rotor consists of different pieces of iron and permanent magnets that are fixed together on a non-ferromagnetic shaft. With a ferromagnetic shaft, a large portion of the flux generated by the permanent magnets would leak through the shaft.

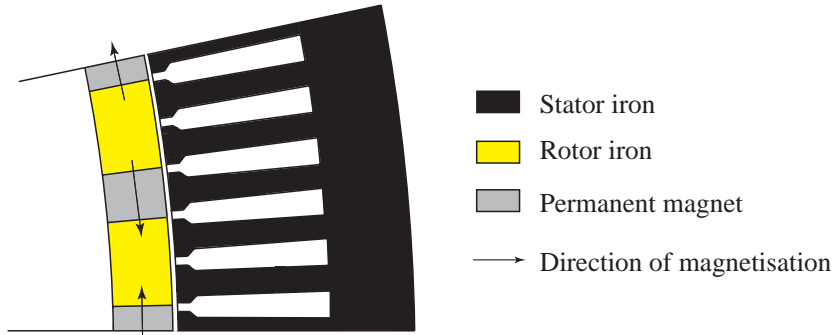


Figure 2.6: Cross-section of a tangentially-magnetized PM motor (one pole pair).

The tangentially-magnetised PM motor has the drawback that many pieces of iron and permanent magnets have to be manipulated if the number of poles is high. Therefore, some production difficulties can arise. However, this motor does not contain any iron bridges compared to the configuration with V-shaped PM and the flux leakage is thus very low.

A design of a tangentially-magnetized PM machine was presented in [16]. However, the study emphasizes more the choice of the type of windings than the advantages of this rotor configuration.

2.2 Axial-flux PM machines

The axial-flux PM (AFPM) machine is another possible solution for low-speed direct-drive applications. This machine features a large diameter and a relatively short axial length compared to a radial-flux PM machine. As suggested by its name and figure 2.7, the flux from the PMs flows axially while the current flows in the radial direction.

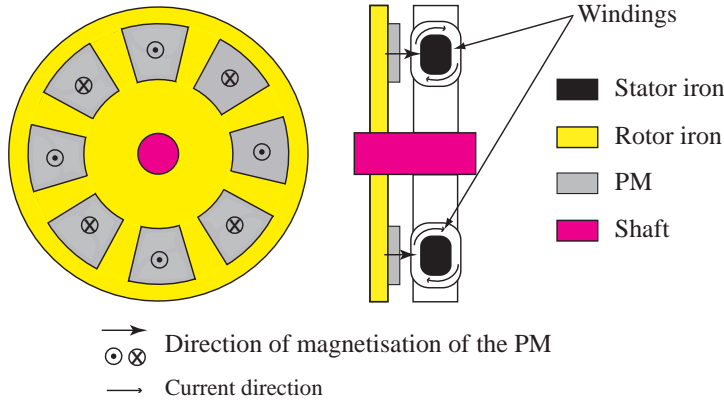


Figure 2.7: AFPM machine with flux and current flows.

Different kinds of AFPM exist, but for low-speed applications the most commonly studied topology is the Torus machine [20]. Therein, the stator is placed between the two external rotors that are rigidly connected to the mechanical shaft. The permanent magnets are placed opposite to each other on the two rotors and the stator windings are toroidal (figure 2.8), [21]. The stator can be slotless. The main benefits of the Torus machine are:

- The machine is compact and lightweight with a short axial length.
- Good ventilation and cooling of the stator windings.
- Absence of slots and large effective airgap, which leads to a negligible cogging torque, reduced high-frequency losses and also a low acoustic noise.
- Possibility to stack together many stator and rotor discs, which gives a higher effective airgap surface.

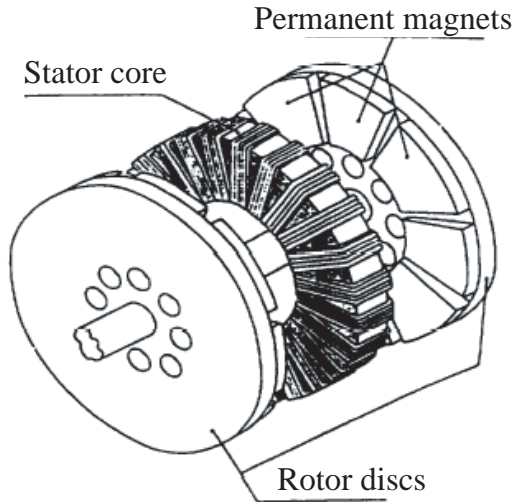


Figure 2.8: Torus machine [20].

The main drawback of this kind of machine is its complex assembly due to axial forces.

Other AFPM machine configurations are the double-sided with internal PM disk machines, single-sided machines, ironless double-sided machines, and multidisk machines. These are described in [22]. The different configurations are compared in [12] for a nominal speed of 1000 rpm.

AFPM machines were studied using prototypes in [3], [8], [10], [23], [24], [25]. The applications are small wind turbines, ship propulsion and elevators. Different companies already produce AFPM machines as the wind turbine producer Jeumont Industry, the motor fabricant Lynx Motion Technology Corporation, and the elevator producer Kone that established the concept of an elevator without a machine room thanks to the use of axial-flux PM motors [7].

2.3 Transverse-flux PM machines

The basic arrangement of a transverse-flux PM machine (TFM) is shown in figure 2.9. This type of machine suits well for low-speed direct-drive applications because of a small pole pitch. Nevertheless, it is not very common yet.

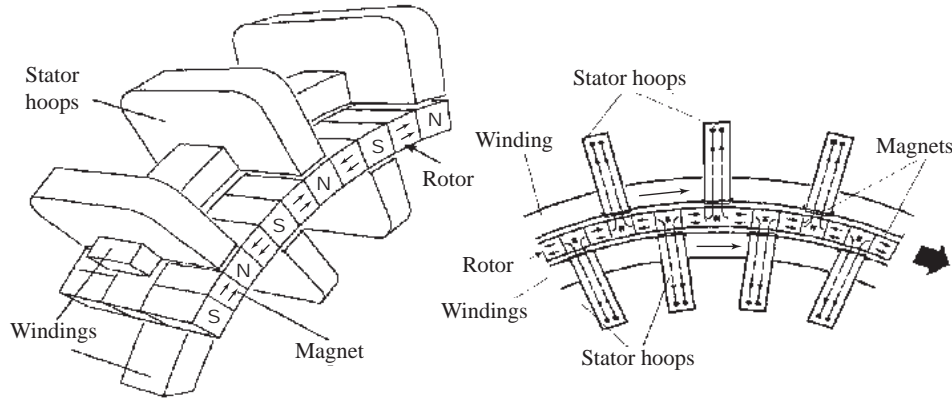


Figure 2.9: Transverse-flux PM machine [26].

The advantage of the TFM is the high specific torque that allows the compactness of the machine. The major drawbacks are the poor power factor at high specific torque and the complexity of the structure which leads to high manufacturing costs.

A prototype of a TFM for an electrical vehicle was built and tested in Germany [27] in 1997. The same year, Rolls-Royce International Research and Development was planning a prototype of a 20 MW, 180 rpm TFM for ship propulsion [26].

2.4 Line-Start PM, modular PM and induction PM machines

2.4.1 Line-Start PM machines

A Line-Start PM motor (LSPM) is a synchronous PM motor with a squirrel cage in the rotor (figure 2.10). The squirrel cage, as it is the case for an induction machines, allows the motor to start without any inverter. The LSPM motor is thus directly connected to the mains. It starts asynchronously thanks to the squirrel cage and operates at steady state synchronously.

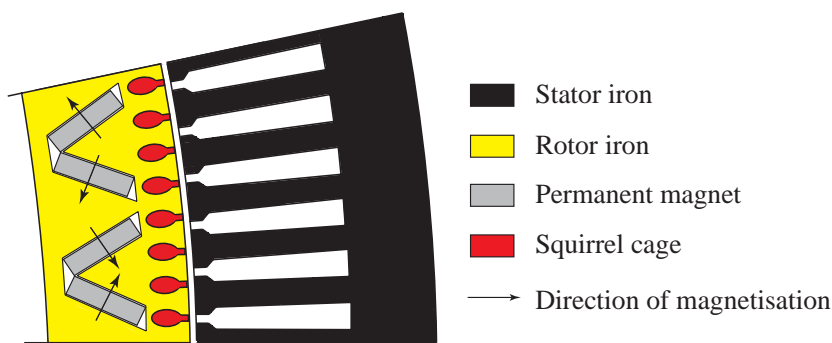


Figure 2.10: Line-Start PM machine (one pole pair).

LSPM motors are intended for replacing induction motors, having the advantage of a much higher efficiency and power factor, but a decreased starting capability and higher costs. These motors are not very common yet, since their design is tricky and they are more expensive than induction machines. They have been investigated for replacing induction motors in pumps [28]. No example of a low-speed direct-drive LSPM machine has been found.

2.4.2 Modular PM machines for variable speed operation

The modular PM machine is used for variable speed wind turbine generators. As its name points out, the machine consists of different modules. Every rotor module comprises one pole. The stator modules are composed of an E-shaped core, whose two slots contain a single coil of the winding (figure 2.11). Each coil is then connected to a single-phase rectifier bridge and operates independently.

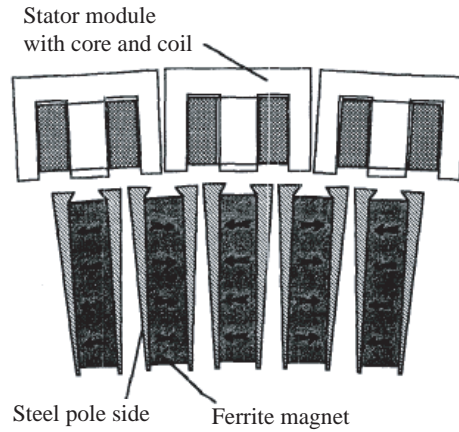


Figure 2.11: Stator and rotor arrangement of a modular PM machine [29].

The advantages of this configuration are mostly its easy assembly, the simple cooling, and the simple coil shape. A drawback is the high reactance of the coils, causing the need for several capacitors to compensate the reactive voltage drop. Some additional eddy-current losses may also arise due to the design structure.

This kind of machine was studied by E. Spooner with the conception of a prototype with 26 poles [29], [30], [31]. O. Carlson studied a 40 kW, 48-pole prototype [2]. The goal was to apply this modular concept for wind turbine generators in the power range of several megawatt.

2.4.3 Induction PM machines

The induction PM machine was studied at the university of Darmstadt for wind turbine applications [32]. No prototype was built. The work was mostly based on Finite Element Methods (FEM) simulations. The generator consists of two rotating parts, the rotor with a squirrel cage in the center and a ring that supports the permanent magnets (see figure 2.12).

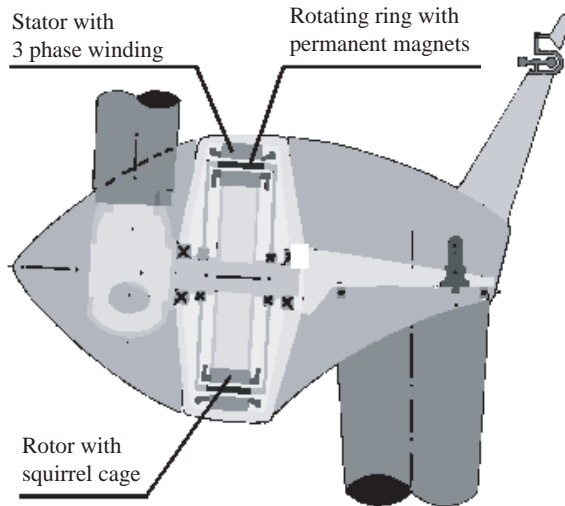


Figure 2.12: Induction PM generator [32].

An advantage of the induction PM generator for wind turbines is the possibility to connect the generator via a transformer directly to the grid, without any power electronics. The slip of the induction machine puts less stress on the blades than with a synchronous generator. However, the mechanical construction is complex due to the two rotating parts.

2.5 The investigated motor configurations

In this thesis, designs of SMPM motors with inner or outer rotors, inset PM motors, buried V-shaped PM motors and tangentially-magnetized PM motors, as well as Torus AFPM motors are investigated (figure 2.13). These motors are not self-starting and need a converter for start-up.

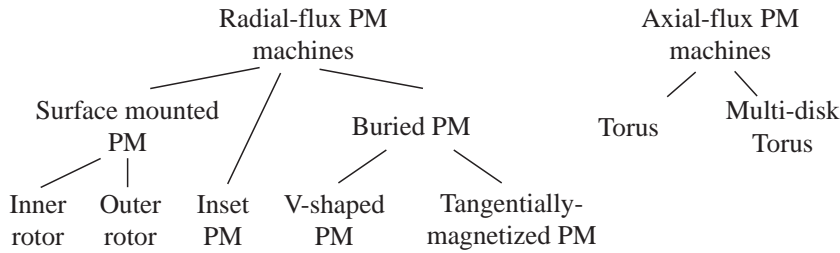


Figure 2.13: The investigated motor configurations.

Transverse-flux motors are not studied because their technology is too different from the one of the radial-flux machines. It is investigated in another project of the department for a direct-driven wind generator.

The modular PM and induction PM machines (such as those described previously) are intended for the special use in wind turbines and therefore they are not considered.

The possibility of a Line-Start PM motor was studied at the beginning of the project and rapidly abandoned because it was impossible to fulfill the requirements. In order to achieve the required nominal speed with a supplied frequency of 50 Hz, 120 poles are needed. These are difficult to fit in a stator with an outer diameter of 500 mm. The results of the studied V-shaped PM motors presented in chapter 4 confirm the impossibility of a LSPM motor design for the mixer.

3 Properties of low-speed radial-flux PM motors

This chapter focuses on the description and modelling of the geometrical, magnetic and electric properties needed for the design of low-speed PM motors. The design process is described subsequently in chapter 4.

- The geometric properties are the different dimensions and areas of the motors.
- The magnetic properties are the flux densities in the airgap and in the teeth.
- The electric properties are the inductances, resistances, ampere-turns and number of conductors per slot.

Most of these properties depend on the motor configuration.

3.1 Geometrical properties: Dimensions of the motors

The geometrical parameters of the different motor configurations are presented in this section. All radial-flux PM motors with inner rotors have the same stator structure as described in section 3.1.1.

3.1.1 Inner-rotor SMPM motors and inset PM motors

Figure 3.1 shows the geometry of a SMPM motor including the parameters of the geometrical dimensions. These dimensions are expressed in equations (3.1) to (3.6), where Q_s is the number of stator slots. The parameter k_{open} is the ratio of the stator slot opening to the slot width (3.6). The teeth are straight, which means that the tooth width b_{ts} is constant all along the tooth.

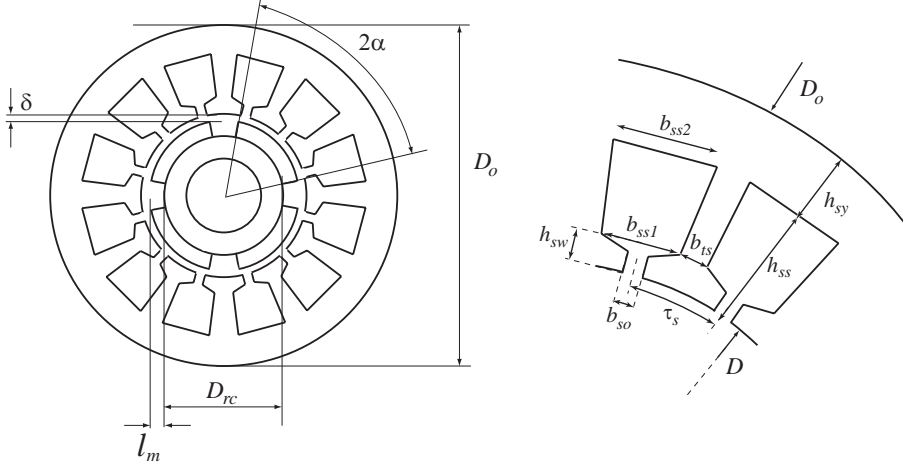


Figure 3.1: Definition of the geometrical parameters for the SMPM designs.

$$D = D_{rc} + 2l_m + 2\delta \quad (3.1) \quad h_{sy} = \frac{1}{2}(D_o - D - 2h_{ss}) \quad (3.4)$$

$$\tau_s = \pi \frac{D}{Q_s} \quad (3.2) \quad b_{ss2} = \pi \frac{D + 2h_{ss}}{Q_s} - b_{ts} \quad (3.5)$$

$$b_{ss1} = \pi \frac{D + 2h_{sw}}{Q_s} - b_{ts} \quad (3.3) \quad k_{open} = b_{so}/b_{ss1} \quad (3.6)$$

The inner stator diameter D is very large compared to the slot pitch τ_s . Therefore, b_{ss1} , b_{ss2} and b_{ts} , which actually are arcs of circle, are approximated as straight lines in equations (3.3) and (3.6). The slot area A_{sl} is given by equation (3.7).

$$A_{sl} = \frac{1}{2} (b_{ss1} + b_{ss2}) * (h_{ss} - h_{sw}) \quad (3.7)$$

According to the equations, the two-dimensional geometrical structure of the stator can be described entirely with the following parameters: D_{rc} , l_m , δ , h_{sw} , b_{ts} , D_o , h_{ss} , k_{open} and Q_s . Adding the number of poles p , the half pole angle α and the active length L , the whole three-dimensional geometry can be described (without considering the end-windings).

3.1.2 Outer-rotor SMPM motors

The geometrical parameters of the outer-rotor designs are defined in figure 3.2. The equations of the inner-rotor SMPM motor are adapted to this particular configuration and become equations (3.8) to (3.13).

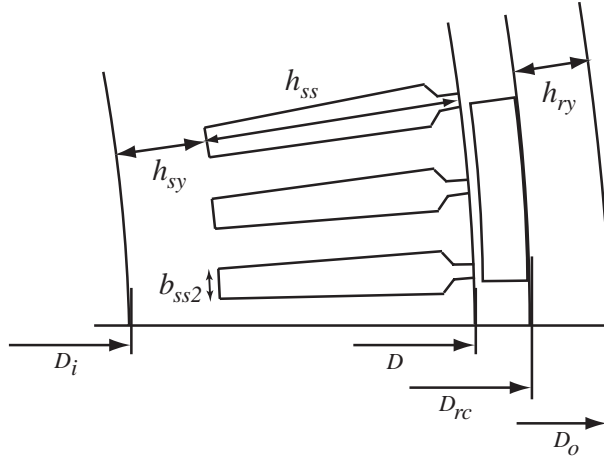


Figure 3.2: Definition of the geometrical parameters for the outer-rotor SMPM motors.

$$D = D_{rc} - 2l_m - 2\delta \quad (3.8) \quad h_{sy} = \frac{1}{2}(D - D_i - 2h_{ss}) \quad (3.11)$$

$$b_{ss1} = \pi \frac{D - 2h_{sw}}{Q_s} - b_{ts} \quad (3.9) \quad h_{ry} = \frac{1}{2}(D_o - D_{rc}) \quad (3.12)$$

$$b_{ss2} = \pi \frac{D - 2h_{ss}}{Q_s} - b_{ts} \quad (3.10) \quad k_{open} = \frac{b_{so}}{b_{ss1}} \quad (3.13)$$

3.1.3 Buried PM motors

For the buried designs, the geometrical parameters of the stator are expressed as for the inner-rotor SMPM motors. The rotor parameters for the V-shaped PM and tangentially-magnetized PM motor designs are described in figure 3.3.

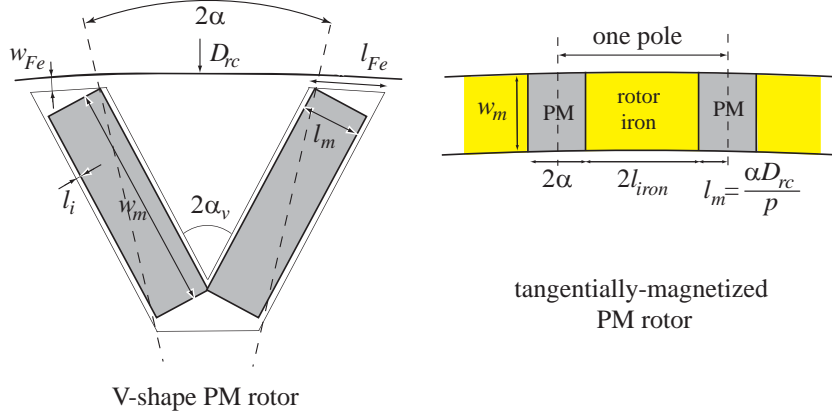


Figure 3.3: Definition of the parameters for the buried PM rotor geometries.

The inner stator diameter D is not dependent on the thickness of the permanent magnets. The position of the permanent magnets can be deduced from the magnet thickness l_m , the half pole angle α and the angle in the V α_v . The airgap around the permanent magnets and the thickness of the iron bridges are set to $l_i = 0.2 \text{ mm}$ and $w_{Fe} = 0.54 \text{ mm}$ respectively.

3.2 Magnetic properties

3.2.1 Analytical calculation of the flux density in the airgap

The amplitude of the fundamental airgap flux density \hat{B}_δ , has to be calculated with accuracy since the design procedure relies on it. The calculation of \hat{B}_δ varies for the different investigated configurations.

Surface-mounted PM motors

For the SMPM motor designs, the airgap flux density is assumed to have a rectangular shape as wide as the permanent magnet width and a maximum value B_m . Figure 3.4 shows the flux density in the airgap simulated with FEM and the analytical estimation.

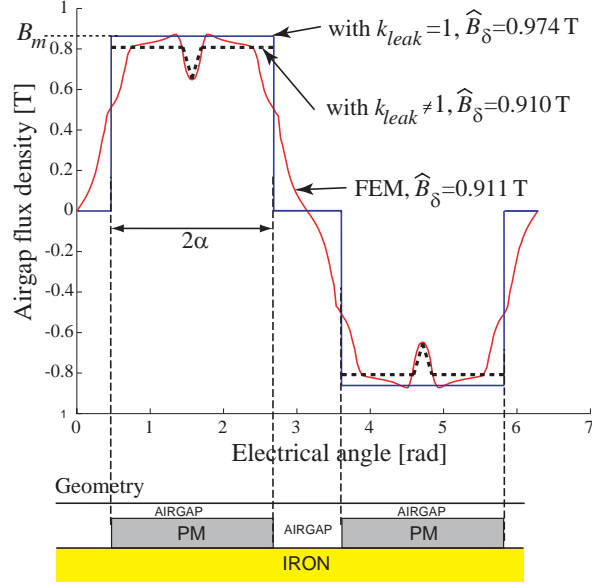


Figure 3.4: Analytically calculated and FEM simulated airgap flux densities, example of a 60-pole SMPM motor.

B_m is calculated as follows:

$$B_m = \frac{B_r k_{leak}}{1 + \frac{\mu_r \delta k_C}{l_m}} \quad (3.14)$$

where B_r is the remanence flux density of the magnet, μ_r the relative magnet permeability and k_C the Carter factor [33].

$$k_C = \frac{\tau_s}{\tau_s - \frac{(k_{open} b_{ss1})^2}{b_{ss1} k_{open} + 5\delta}} \quad (3.15)$$

The factor k_{leak} takes the magnetic leakage between two neighboring permanent magnets into account. Indeed, assuming that the flux density has

a rectangular shape and neglecting the leakage, can cause a difference of around 10 % between the analytically calculated and FEM simulated fundamental airgap flux densities. This can be seen in figure 3.4.

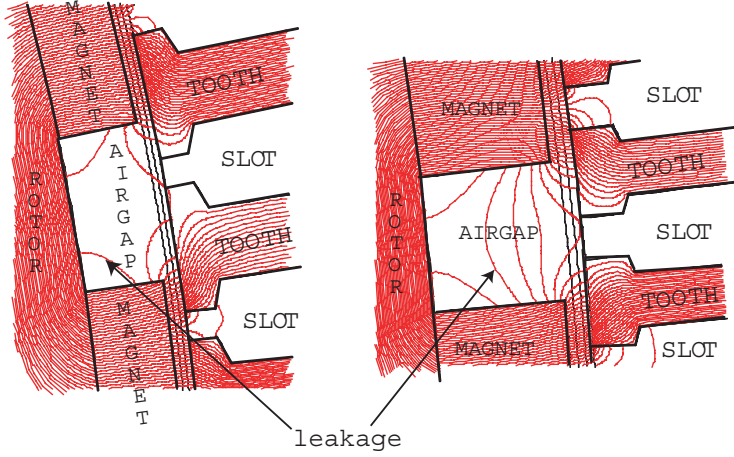


Figure 3.5: Flux lines for SMPM motors with $p = 40$ and $p = 70$.

Figure 3.5 shows the leakage between two permanent magnets for two different pole numbers (100 flux lines are plotted). The higher the number of poles, the lower the distance between the permanent magnets and consequently the reluctance gets lower, thus increasing the leakage. The magnetic leakage between the permanent magnets is also notably dependent on the magnet height and the airgap length, but this has been neglected in order to keep a simple model. Magneto-static FEM simulations are used to define the factor k_{leak} as a function that depends linearly on the pole number (figure 3.6). The leakage factor is defined as the percentage of the flux lines that pass through the airgap (3.16). Appendix B describes how the FEM simulations were conducted.

$$k_{leak} = \frac{100 - \text{number of leakage flux lines}}{100} \quad (3.16)$$

$$k_{leak} = \begin{cases} \frac{100 - (7p/60 - 0.5)}{100} & \text{for SMPM motors} \\ \frac{100 - (7p/60 - 3)}{100} & \text{for outer-rotor SMPM motors} \\ \frac{100 - (p/10)}{100} & \text{for inset PM motors} \end{cases}$$

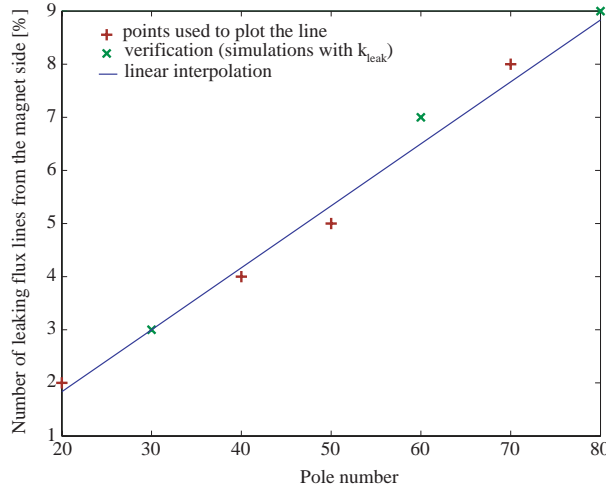


Figure 3.6: Flux lines leaking from the permanent magnets as a function of the number of poles, for SMPM motors.

Furthermore, the influence of the slot opening on the airgap flux is taken into account, as can be seen in figure 3.4. The width of the drop is approximated as the slot opening width, whereas the depth is set proportional to the width.

Table 3.1 presents the analytical results obtained for the amplitude of the fundamental airgap flux density compared to the FEM results for different geometries. The difference between analytical and FEM values does not exceed 2%.

Table 3.1: Comparison of analytical and FEM values of the flux density in the airgap of SMPM motor designs.

Pole number	20	30	40	50	60	70	80
$\hat{B}_{\delta,an}$ [mT]	990.1	956.5	946.7	942.9	945.7	948.2	880.7
$\hat{B}_{\delta,FEM}$ [mT]	974.2	943.9	937.2	931.1	935.3	930.1	872.9
Relative error [%]	1.6	1.3	1.0	1.3	1.1	1.9	0.9

Inset PM motors

For the inset PM motor designs, the method used for the SMPM motors to calculate the flux density has to be adapted since there is even more flux leakage between two permanent magnets. Instead of crossing the airgap, a significant part of the magnetic flux leaks through the iron pieces (figure 3.7).

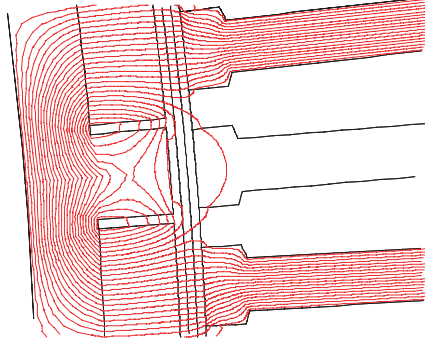


Figure 3.7: Flux leakage through the iron piece in an inset PM motor.

The maximum value of the airgap flux density B_m is calculated with equation (3.14). k_{leak} is obtained by using FEM simulations as in the SMPM motor designs. According to [34], the flux leakage through the iron pieces is negligible if the gap between the magnet and the iron piece is more than twice the airgap length. The waveform of the airgap flux density in figure 3.8 is based on this assumption. The influence of the slot opening is also taken into account.

The difference between the FEM simulated and analytically calculated values of the fundamental airgap flux density is less than 3% for pole numbers between 20 and 70, as shown in table 3.2.

Table 3.2: Comparison of analytical and FEM values of the fundamental airgap flux density for inset PM motor designs.

Pole number	20	30	40	50	56	60	70
$\vec{B}_{\delta,an}$ [mT]	943.4	877.5	887.4	891.1	954.1	890.8	885.5
$\vec{B}_{\delta,FEM}$ [mT]	928.4	873.9	891.2	901.0	958.4	906.6	906.2
Relative error [%]	1.6	0.4	-0.4	-1.1	-0.4	-1.7	-2.3

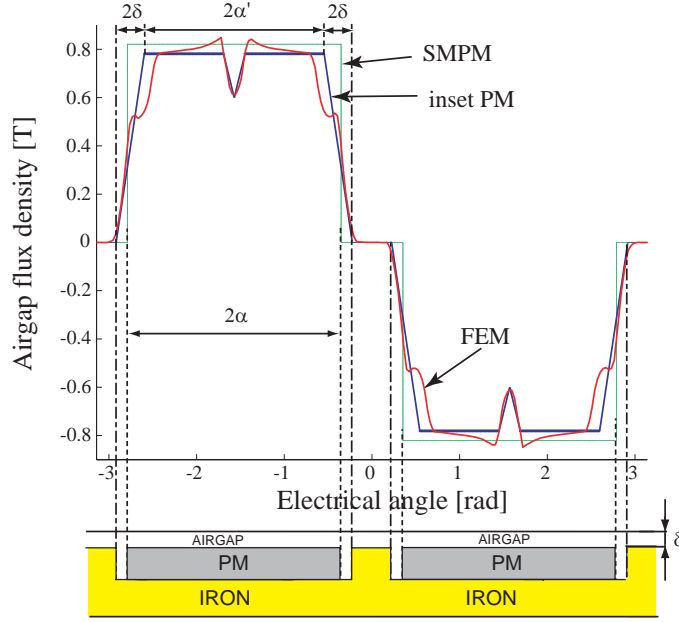


Figure 3.8: FEM simulated and analytically calculated airgap flux densities of an inset PM motor.

V-shaped buried PM motors

The maximum of the airgap flux density B_m for the V-shaped buried PM motor is calculated using equation (3.17), which is derived in [35]. Figure 3.3 describes the different notations used in the formula.

$$B_m = \frac{B_r - B_{sat} \frac{w_{Fe}}{w_m} \left(1 + \mu_r \frac{l_i}{l_m}\right)}{\left(\frac{2\alpha D_r}{pw_m} + 2 \frac{w_{Fe}}{l_{Fe}} \cdot \frac{k_C \delta}{w_m}\right) \left(1 + \mu_r \frac{l_i}{l_m}\right) + \mu_r \frac{k_C \delta}{l_m}} \quad (3.17)$$

where B_{sat} is the flux density in the saturated iron bridges.

The fundamental airgap flux density is then calculated as for the SMPM motor designs.

Table 3.3: Comparison of analytical and FEM values of the fundamental airgap flux density for V-shaped PM motor designs.

Pole number	20	30	40	50	60
$\hat{B}_{\delta,an}$ [T]	1.10	1.11	1.10	1.12	0.864
$\hat{B}_{\delta,FEM}$ [T]	1.06	1.08	1.09	1.10	0.877
Relative error [%]	3.8	2.7	0.9	1.8	-0.1

Tangentially-magnetized PM motors

The tangentially-magnetized PM motor configuration is not very conventional. Thus, the calculation of B_m has been determined from the Ampere's law and the equivalent lumped circuit of the motor (figure 3.9). The considered part of the permanent magnet is seen as a constant magneto-motive force source $H_m l_m$, in series with a constant internal reluctance \mathfrak{R}_m . H_m is the coercive magnetic field intensity of the magnet.

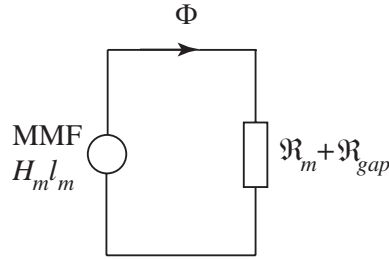


Figure 3.9: Equivalent magnetic circuit for half a pole (half a PM and air-gap for half iron width).

$$H_m l_m = \frac{B_r}{\mu_0 \mu_r} l_m \quad (3.18)$$

and

$$\mathfrak{R}_m = \frac{l_m}{\mu_0 \mu_r L w_m} \quad (3.19)$$

The airgap reluctance is equal to:

$$\mathfrak{R}_{gap} = \frac{\delta k_C}{\mu_0 L l_{iron}} \quad (3.20)$$

with

$$l_{iron} = \left(\frac{\pi}{2} - \alpha \right) \frac{D_{rc}}{p} \quad (3.21)$$

Assuming that the permeability of iron is infinite, the following equation can be obtained from the equivalent lumped circuit:

$$H_m l_m = (\mathfrak{R}_m + \mathfrak{R}_{gap}) \Phi \quad (3.22)$$

where the flux Φ is:

$$\Phi = B_m L l_{iron} \quad (3.23)$$

Finally B_m is given by:

$$B_m = \frac{B_r}{1 + \frac{\mu_r \delta k_C w_m}{l_m l_{iron}}} \cdot \frac{w_m}{l_{iron}} \quad (3.24)$$

The approximation used to calculate the fundamental airgap flux density is described in figure 3.10. As illustrated in the figure, a factor $k_{leak\alpha}$ is introduced to correct the pole angle. It is determined from FEM simulations:

- $k_{leak\alpha} = 1$ for $B_m \leq 0.9 \text{ T}$
- $k_{leak\alpha} = 0.9$ for $0.9 \text{ T} < B_m \leq 1 \text{ T}$
- $k_{leak\alpha} = 0.8$ for $1 \text{ T} < B_m$

Table 3.4 shows how accurate the analytical calculations are, compared with the respective FEM values.

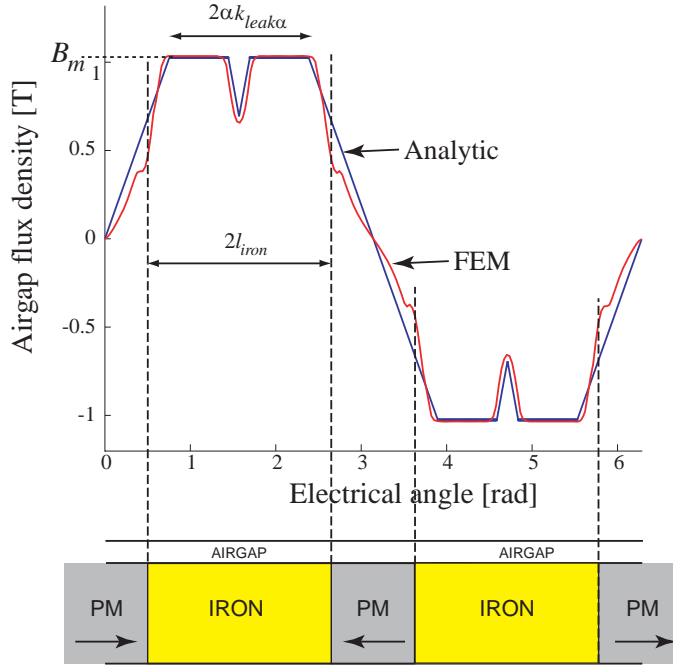


Figure 3.10: FEM simulated and analytically calculated flux densities in the airgap for a tangentially-magnetized PM motor.

Table 3.4: Comparison of analytical and FEM values of the fundamental airgap flux density for tangentially-magnetized PM motors.

Pole number		30	40	50	60	70
$k_{leak\alpha} = 0.8$ $1 \text{ T} < B_m$	$\hat{B}_{\delta,an} [\text{T}]$	1.06	1.10	1.10	1.09	1.03
	$\hat{B}_{\delta,FEM} [\text{T}]$	1.09	1.06	1.12	1.11	0.99
	Relative error [%]	-2.7	3.8	-1.8	-1.8	4.0
$k_{leak\alpha} = 0.9$ $0.9 \text{ T} < B_m \leq 1 \text{ T}$	$\hat{B}_{\delta,an} [\text{T}]$	1.10	1.03	0.98	0.99	0.96
	$\hat{B}_{\delta,FEM} [\text{T}]$	1.08	1.03	0.93	0.97	0.96
	Relative error [%]	2.0	0	5.3	2.0	0
$k_{leak\alpha} = 1$ $B_m \leq 0.9 \text{ T}$	$\hat{B}_{\delta,an} [\text{T}]$	1.05	1.00	0.93	0.89	0.92
	$\hat{B}_{\delta,FEM} [\text{T}]$	1.01	1.00	0.91	0.84	0.88
	Relative error [%]	4.0	0	2.2	5.9	4.5

3.2.2 Analytical calculation of the flux density in the teeth

It is important to obtain a correct analytical value of the flux density created by the permanent magnets in the teeth. If the value turns out to be higher than expected, the teeth can be very saturated which means a high magnetic leakage.

The flux density in the teeth B_{ts} is calculated from the PM flux flowing through the airgap, the width of a tooth b_{ts} and the number of teeth through which the flux is flowing (2 for $q = 1$). Equation (3.25) gives the flux density in a tooth for a SMPM motor. The factor $k_{leaktooth}$ is used to take into account the part of leakage flux, flowing through the tooth shoe only.

$$B_{ts} = \frac{B_m 2\alpha_p^2 \left(\frac{D}{2} - \delta\right) \cdot (1 - k_{leaktooth})}{2b_{ts}} \quad (3.25)$$

$$k_{leaktooth} = \frac{17p/56 - 13/14}{100} \quad (3.26)$$

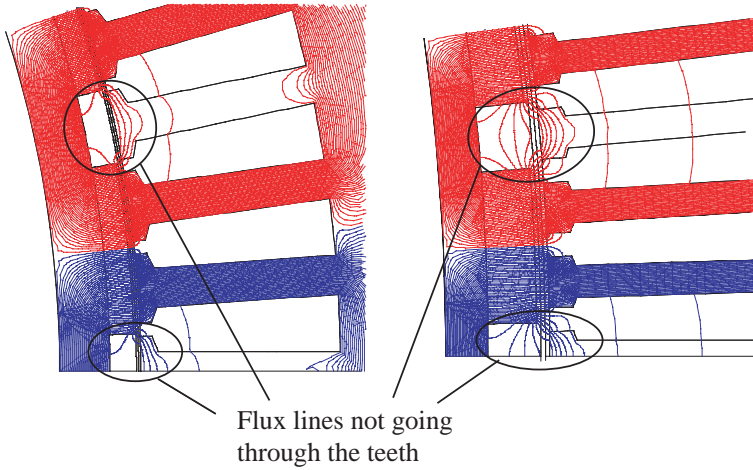


Figure 3.11: Flux lines for SMPM motors with $p = 30$ and $p = 70$.

Figure 3.11 reveals the flux lines that are used for the calculation of the leakage factor (the total number of flux lines is 100). For the 30-pole motor, eight flux lines are not flowing through the teeth, whereas it is twenty flux

lines for the 70-pole motor. The factor $k_{leaktooth}$, given in equation (3.26), is then determined as a function of the pole number by linear interpolation, using the FEM simulation results as those of figure 3.11. Table 3.5 shows the obtained results for different geometries of SMPM motors.

Table 3.5: Comparison of analytical and FEM values of the flux density in the teeth for SMPM motors.

Pole number	20	30	40	50	60	70	80
$\hat{B}_{ts,an}$ [T]	1.6	1.6	1.6	1.6	1.6	1.6	1.6
$\hat{B}_{ts,FEM}$ [T]	1.55	1.59	1.59	1.59	1.59	1.59	1.62
Relative error [%]	3.1	0.6	0.6	0.6	0.6	0.6	-1.3

3.3 Electrical properties

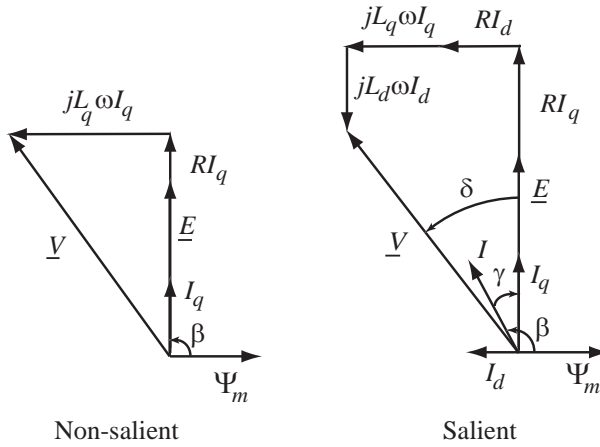


Figure 3.12: Phasor diagrams for salient and non-salient PM machines at rated speed.

The phasor diagrams for non-salient and salient PM machines at rated speed are represented in figure 3.12. SMPM motors are non-salient. The others, buried and inset PM designs, are salient. In this section, it will be shown how the different parameters of the phasor diagram are calculated, which comprise:

- The d- and q- axis inductances, L_d and L_q
- The resistance of one phase of the stator winding R
- The external voltage V
- The induced voltage E
- The ampere-turns, $n_s I$
- The angle β between the flux from the permanent magnets Ψ_m or the d- axis, and the current I

From the phasor diagram, the number of conductors per slot n_s can then be calculated as shown in the following.

3.3.1 Inductances

SMPM motors

For a non-salient synchronous motor the d- and q- axis synchronous inductances are equal and

$$L_d = L_q = L_l + L_{md} = L_l + L_{mq} \quad (3.27)$$

where L_l is the leakage inductance and L_{md} and L_{mq} are the d- and q- axis magnetizing inductances respectively. The calculation of these inductances are detailed in [36].

$$L_l = p q n_s^2 L \mu_0 \lambda_1 \quad (3.28)$$

$$L_{md} = \frac{3}{\pi} (q n_s k_{w1})^2 \frac{\mu_0}{\delta k_C + \frac{l_m}{\mu_r}} (D - \delta) L \quad (3.29)$$

where λ_1 is the specific permeance coefficient of the slot opening and depends on the slot geometry [33]; q is the number of slots per pole per phase and k_{w1} is the fundamental winding factor. If the number of slots per pole per phase is equal to 1, then the winding factor k_{w1} is 1. Other winding configurations are discussed in chapter 5.

Inset PM motors

For the inset PM motor designs, the d-axis magnetizing inductance is calculated with the same equation as for the SMPM motor (3.29). The q-axis magnetizing inductance is calculated with:

$$L_{mq} = \frac{3}{\pi} (q n_s k_{w1})^2 \frac{\mu_0}{\delta k_C} (D - \delta) L \quad (3.30)$$

Tangentially-magnetized PM motors

Since there could not be found any analytical expression of the q-axis inductance, the saliency is checked with FEM simulations. The d-axis inductance is calculated as for the SMPM motor. Two FEM simulations at different load conditions are run, one with only q-axis current and one with only d-axis current. The ratio of the simulated voltages in phase A gives the saliency (L_q/L_d). This method has been first checked on inset PM motor designs. For tangentially-magnetized PM motors, the saliency (L_q/L_d) was found to be around 4 for two different designs. Therefore, the q-axis inductance has been roughly approximated as $4L_d$. Although this approximation might not be very accurate for other tangentially-magnetized PM motor designs, the calculation of the q-axis inductance was not improved. Indeed, an inaccurate value of the q-axis inductance causes a reluctance torque that is not optimized. The torque might then be underestimated. However, this does not penalize the tangentially-magnetized PM motor configuration, as will be seen in the next chapter.

3.3.2 Resistance of one phase of the stator winding

It is assumed that all the coils in one phase are coupled in series. The phase resistance is calculated as:

$$R = \rho_{cu} \frac{(pL + (D + h_{ss})\pi k_{coil}) n_s^2 q}{f_s A_{sl}} \quad (3.31)$$

f_s is the slot fill factor. The end-windings are taken into account by introducing the term $D\pi k_{coil}$, [37].

3.3.3 The external voltage

Since all the investigated motor configurations are not self-starting, power electronic devices are essential to start the motor and make it rotate at the right speed.

Figure 3.13 shows a diagram of a simple drive that suits the application. A diode rectifier is coupled to a 3-phase inverter via a filter capacitor. The output line-to-line voltage V_{LL} of the inverter, which is also the voltage applied to the motor, can be estimated as [38]:

$$V_{LL} = 0.612m_a V_d \quad (3.32)$$

where m_a is the amplitude modulation ratio of the inverter and V_d the rectified DC voltage across the filter capacitor ($V_d = 400$ V). From equation (3.32), a phase voltage V of around 70 V is obtained assuming a low amplitude modulation ratio ($m_a = 0.5$). This is the worst case as the current and the losses in the inverter increase with the decreasing voltage. This voltage is used to calculate the number of conductors per slot of the motor.

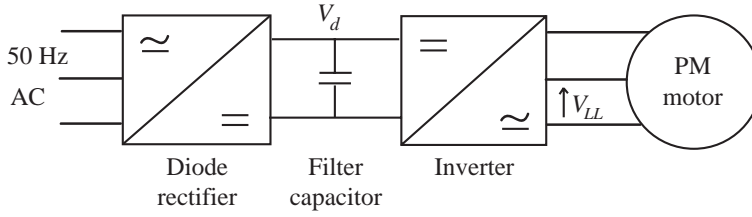


Figure 3.13: Possible drive for PM motors.

3.3.4 Induced voltage

The induced phase voltage E is deduced from Faraday's law:

$$E(t) = \frac{d\Psi_m}{dt} = N_s \frac{d\phi_m}{dt} \quad (3.33)$$

The maximum fundamental of the magnet flux $\hat{\phi}_m$ linked to one turn of the coil is:

$$\hat{\phi}_m = \frac{2}{\pi} \hat{B}_\delta L(D - \delta) \frac{\pi}{p} \quad (3.34)$$

N_s is the number of turns per phase which are in series:

$$N_s = \frac{p}{2} q n_s \quad (3.35)$$

Finally the rms-value of the induced voltage can be calculated as:

$$E = \frac{1}{\sqrt{2}} \omega k_{w1} q n_s \hat{B}_\delta L (D - \delta) \quad (3.36)$$

3.3.5 Ampere-turns per slot

Current loading

The peak value of the fundamental current loading \hat{S}_1 is calculated from the torque equation:

$$\hat{S}_1 = \frac{4T}{\pi (D - \delta)^2 L \hat{B}_\delta k_{w1} k_{cor} \sin \beta} \quad (3.37)$$

where β is the angle between Ψ_m and I . β depends on the saliency. For a non-salient geometry as the SMPM motor, β is $\frac{\pi}{2}$. For a salient geometry, the method applied to calculate β is described in section 3.3.6.

The correction factor k_{cor} is used to compensate the losses and leakages that are not analytically calculated, such as the flux leakage through the slots. This factor is obtained from FEM simulations at load conditions, for the different motor configurations. It assures that the demanded nominal torque is reached in the FEM simulations and thus enables a fair comparison between the different motor configurations.

Table 3.6: Correction factor k_{cor}

Motor design	SMPM	Outer-rotor SMPM	Inset PM	Tangentially-magnetized PM
k_{cor}	0.95	0.94	1	0.99

Table 3.6 provides the factor for the studied motor configurations. For the inset PM motors and tangentially-magnetized PM motors, the current loading is calculated with equation (3.37), that does not take the contribution of the reluctance torque into account. Therefore, k_{cor} is equal or almost equal to one. The reluctance torque, which is around 5% of the nominal torque, compensates already the leakages that k_{cor} was introduced for.

Ampere turns and current density

From the fundamental peak current loading and the ampere-turns (3.38), the current density J can be calculated.

$$n_s \hat{I} = \hat{S}_1 \tau_s \quad (3.38)$$

$$J = \frac{n_s I}{A_{sl} f_s} \quad (3.39)$$

3.3.6 Angle β

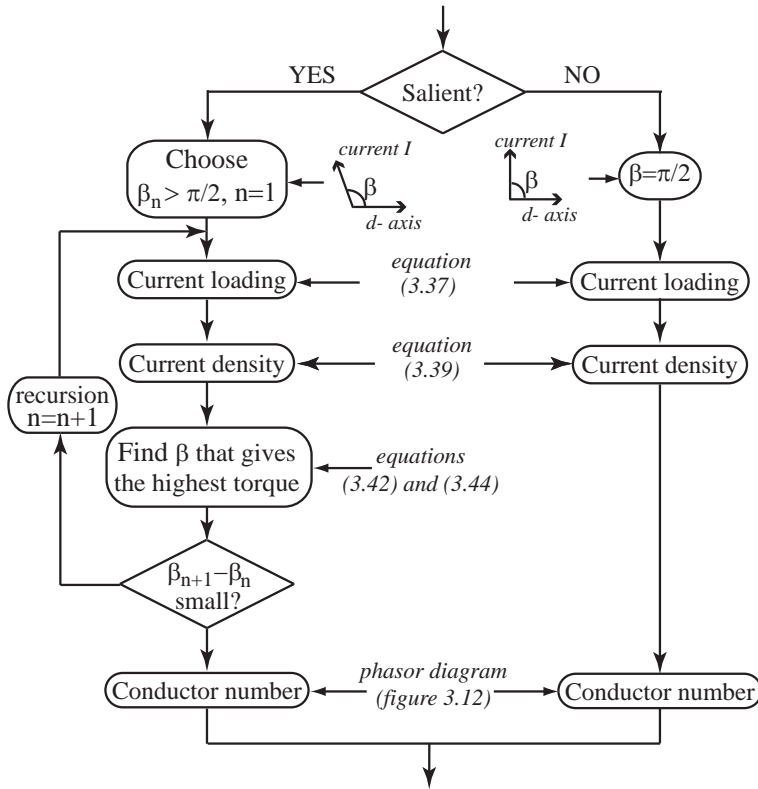


Figure 3.14: Chart description of how to determine β depending on the saliency.

For a salient machine, the d-axis current generates a reluctance torque in addition to the torque created by the permanent magnets. Thus, the torque equation becomes:

$$T = \frac{3p}{2} [\Psi_m I_q + (L_d - L_q) I_d I_q] \quad (3.40)$$

The contribution of the reluctance torque to the total torque can be adjusted with the angle β . Indeed, the d- and q- axis currents depend on β :

$$\begin{cases} I_d = \hat{I} \cos \beta \\ I_q = \hat{I} \sin \beta \end{cases} \quad (3.41)$$

For non-salient machines, the d-axis current does not contribute to the torque, therefore β is chosen as $\frac{\pi}{2}$.

For a salient machine, the angle β is chosen so that it gives the maximum torque for a given current.

$$\frac{dT}{d\beta} = 0 \quad (3.42)$$

By inserting equations (3.40) and (3.41) into equation (3.42), a second order equation is obtained:

$$2(L_d - L_q) \hat{I}^2 \cos^2 \beta + \hat{\Psi}_m \hat{I} \cos \beta - (L_d - L_q) \hat{I}^2 = 0 \quad (3.43)$$

In this equation, the inductances depend on the square of the number of conductors per slot. These are unknown as is also the nominal current I . However, the value of the ampere-turns per slot is known from the required torque (3.38). The second order equation can therefore be transform into equation (3.44), which can be solved for β .

$$2(L'_d - L'_q) (n_s \hat{I})^2 \cos^2 \beta + \frac{p}{2} q \hat{\phi}_m (n_s \hat{I}) \cos \beta - (L'_d - L'_q) (n_s \hat{I})^2 = 0 \quad (3.44)$$

where L'_d , L'_q and $\hat{\phi}_m$ are independent of the number of conductors per slots and depend only on the dimensions:

$$L_d = L'_d n_s^2 \quad L_q = L'_q n_s^2 \quad (3.45)$$

The determination of the angle β needs a recursive process, since the current loading depends on it (3.37). The recursion is described in figure 3.14. Different values of β are tested in the recursive process in order to find the minimum current together with the angle β that provides the required torque. Knowing the angle β and the d- and q- axis currents, the number of conductors per slot can be calculated using the phasor diagram at nominal speed.

3.3.7 Number of conductors per slot

As equations (3.29), (3.30) and (3.31) imply, the inductances and resistances depend on the square of the number of conductors per slot, whereas the induced voltage is linearly dependent on the number of conductors per slot (3.33):

$$\begin{aligned} L_d &= n_s^2 L'_d & L_q &= n_s^2 L'_q \\ R &= n_s^2 R' & E &= n_s E' \end{aligned} \quad (3.46)$$

Non-salient motor designs

For the non-salient motors, the vector diagram in figure 3.12 gives the following equation:

$$\hat{V}^2 = \left(\hat{E} + RI_q \right)^2 + (L_d \omega I_q)^2 \quad (3.47)$$

Using the same method as for calculating β , the equation becomes:

$$\hat{V}^2 = \left(n_s \hat{E}' + n_s^2 R' I_q \right)^2 + \left(n_s^2 L'_d \omega I_q \right)^2 \quad (3.48)$$

$$\hat{V}^2 = n_s^2 \left(\hat{E}' + R' (n_s I_q) \right)^2 + n_s^2 \left(L'_d \omega (n_s I_q) \right)^2 \quad (3.49)$$

Finally, as $I_q = \hat{I}$ ($\beta = \pi/2$), the number of conductors per slot can be calculated as:

$$n_s = \frac{\hat{V}}{\sqrt{\left(\hat{E}' + R' n_s \hat{I} \right)^2 + \left(L'_d \omega n_s \hat{I} \right)^2}} \quad (3.50)$$

Salient motor designs

For the salient motors, the vector diagram of figure 3.12 gives the following equation:

$$\hat{V}^2 = \left(\hat{E} + RI_q + L_d \omega I_d \right)^2 + (-L_q \omega I_q + RI_d)^2 \quad (3.51)$$

Therefore, the number of conductors per slot can be derived as:

$$n_s = \frac{\hat{V}}{\sqrt{\left(\hat{E}' + R' (n_s \hat{I}) \sin\beta + L_d \omega (n_s \hat{I}) \cos\beta\right)^2 + \left(n_s \hat{I}\right)^2 \left(-L_q' \omega \sin\beta + R' \cos\beta\right)^2}} \quad (3.52)$$

3.4 Summary

Analytical models to design low-speed radial-flux PM synchronous motors have been presented. These models were validated with FEM simulations. Improvements were conducted by introducing correction factors when required. In the next chapter, the method to include these models in an optimization process is described.

4 Optimization procedure and comparison of designs with distributed windings

In the following, the procedure for designing radial-flux PM motors for low-speed applications is presented. The goal is to find a design for a 4.4 kW, 50 rpm motor with a limited size and a low weight. The resulting designs with $q=1$ are then compared to each other.

4.1 The design procedure

The geometry of a SMPM motor is completely described with 12 parameters, as seen in section 3.1.1. To find these unknown parameters, an optimization problem has been defined. Hence, the design of radial-flux PM motors is conducted by solving an optimization problem, applying sequential quadratic programming methods [39]. The goal of the optimization is to minimize the weight of the motor and fulfill the requirements from table 1.2 and the constraints that guarantee the required mechanical, thermal, and magnetic behaviors. Appendix C gives some definitions related to optimization and some explanations about how the optimization problem was defined.

The chart in figure 4.1 shows the different steps followed during the design procedure, from the choice of the initial design variables to the calculation of the active weight. It includes the influence of the different constraints as well as appropriate references (to sections and equations). The active weight and the constraints need to be expressed as a function of the design variables. The objective function along with the variables and constraints are given in the following sections.

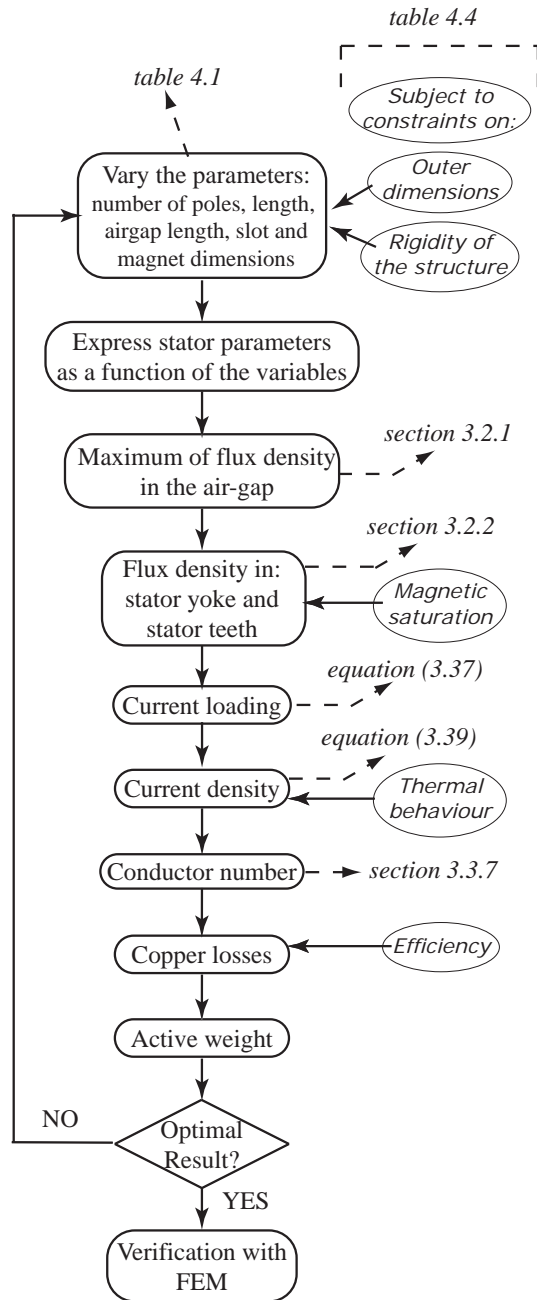


Figure 4.1: Followed procedure to optimize the design of low-speed PM motors.

4.1.1 Objective function

The objective function is the expression, depending on the design variables, that is to be maximized or minimized. Different objective functions are possible, for example:

- The permanent magnet weight, contributing considerably to the total motor cost.
- The copper losses corresponding to the efficiency.
- The active motor weight, being important for the practicability of the motor. For example, a light motor is easy to transport and install. The active motor weight contributes also to the cost of the machine.
- A weighted combination of the three previous functions.

The chosen objective function is the active weight of the motor. It is to be minimized. The copper losses and the permanent magnet weight are limited by means of constraints.

The reasons for this choice are as follow. Primarily, it was considered more challenging to fulfill the motor weight requirements than to achieve a high efficiency, as the induction motor and the gearbox together have a quite low efficiency. Besides, a low motor weight is a better sales argument than a high motor efficiency. The permanent magnet weight is on the other hand not convenient as objective function because the machine weight is then not minimized.

4.1.2 Design variables and their ranges

The design variables of the optimization problem are the number of poles, the number of slots per pole per phase, geometrical parameters that define the stator teeth and the magnets, the rotor diameter, the airgap length and the machine length. The variables and their ranges are given in table 4.1.

The followings remarks complete the table:

- The expression for the minimum length of the airgap was found in [40].
- An upper limit is set for the thickness of the permanent magnets to avoid too high flux leakage between two neighboring permanent magnets.
- The expression of the lower limit of the half pole angle was taken from [19].
- The lower limits for the stator tooth width and the ratio of the stator slot opening to the slot width (k_{open}) are set with the intention to avoid too thin teeth and slot openings that would be impossible to manufacture.
- For the tangentially-magnetized PM motor, the design variables that describe the permanent magnets are the half pole angle $\alpha = \frac{l_m p}{D_{rc}}$ and the magnet thickness w_m .

Table 4.1: Design variables and their ranges

Variable	Symbol	Range
Number of poles	p	$p \geq 20$ and p is even
Number of slots per pole per phase	q	$q \leq 1$
Rotor diameter	D_{rc}	$D_{rc} \leq D_o$
Airgap length	δ	$0.0002 + 0.003\sqrt{\frac{DL}{2}} \leq \delta [m]$
Magnet thickness: surface, V-shaped	l_m	$2\text{ mm} \leq l_m \leq 8\text{ mm}$
tangentially-magnetized	w_m	$2\text{ mm} \leq w_m$
Half pole angle in electrical degrees	α	$0.7\pi/2 \geq \alpha$
Outer stator diameter	D_o	$D_o \leq 500\text{ mm}$
Stator tooth width	b_{ts}	$b_{ts} \geq 2.5\text{ mm}$
Stator slot height	h_{ss}	$h_{ss} \geq 0$
Stator slot opening over slot width	k_{open}	$0.2 \leq k_{open}$
Slot wedge height	h_{sw}	$h_{sw} \geq 1\text{ mm}$
Machine length	L	$100\text{ mm} \leq L \leq 500\text{ mm}$
V-angle between magnets	α_v	$\alpha_v \leq \pi$

4.1.3 Given constants

The constants given in table 4.2 are used in the design procedure. The considered permanent magnet material is Neodymium Iron Boron (NdFeB).

Table 4.2: Constants.

Motor	Rated speed	50 rpm
	Rated torque	840 Nm
	Rated power	4.4 kW
Permanent magnet	Remanence flux density	1.08 T
	Relative permeability	1.03
Iron	Stacking factor of the stator iron laminations	1
Winding	Stator slot fill factor	f_s [table 4.3]
	End-winding factor	k_{coil} [table 4.3]
	Copper temperature	80 °C
Material properties	Magnet density	7500 kg/m ³
	Iron density	7750 kg/m ³
	Copper density	8920 kg/m ³
	Copper resistivity at 20 °C	1.72e − 8 Ω/m
Flux density in the rotor yoke		1.4 T

The end-winding factor k_{coil} used in equation (3.31) and the slot fill factor f_s depend on the type of winding. These values are given in table 4.3 for distributed windings as well as concentrated windings with single or double layer [37], [41].

Table 4.3: Winding constants.

	Distributed winding	Concentrated 1-layer winding	Concentrated 2-layer winding
k_{coil}	1.6 Q_s/p	1.46	0.93
f_s	0.45	0.60	0.60

The magnetization curve of the iron material (LOSIL500) used in the FEM simulations is given in figure 4.2.

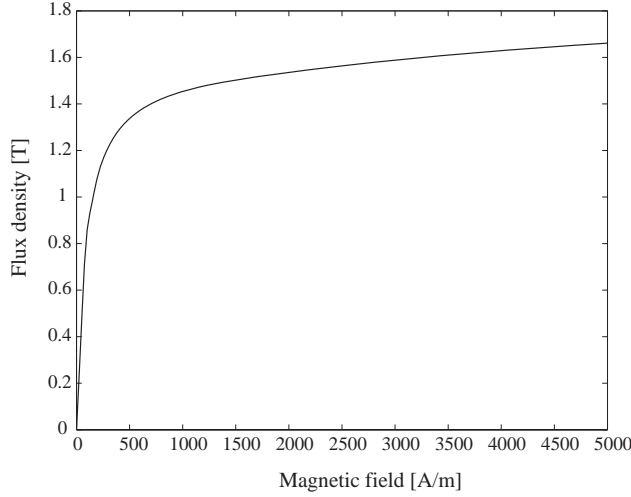


Figure 4.2: Magnetization curve of the iron material (Losil500).

For the SMPM and inset PM motors, the flux density in the rotor yoke B_{ry} is set constant in order to limit the number of design variables. In this way, B_{ry} determines the inner rotor diameter D_i (4.1), which thus does not need to be a design variable.

$$D_i = D_{rc} - \frac{B_m 2\alpha_p^2 (D - \delta)}{B_{ry}} \quad (4.1)$$

4.1.4 Constraints

The design constraints are described in table 4.4. They guarantee the required mechanical, thermal and magnetic behaviors. A constraint is set on the maximum weight of the permanent magnets and on the maximum copper losses. In addition to these constraints, it is checked for each design that the permanent magnets are not subject to a too high negative magnetic field that reduces their flux density and irreversibly demagnetize them. The followed method is described in [36] and does not take the influence of the temperature into account.

In the next section, the optimization results obtained with these constraints are presented.

Table 4.4: Constraints.

Objective of the constraints	Description of the constraint	Equation	Reference
guarantee the rigidity of the mechanical structure	stator yoke height at least half the slot height	$h_{sy} \geq h_{ss}/2$	[19]
	slot width between 0.15 and 0.5 times the slot height	$0.15h_{ss} \leq b_{ss2} \leq 0.5h_{ss}$	[19]
	tooth width at least 30 % of the slot pitch	$b_{ts} \geq 0.3\tau_s$	[19]
	slot opening width at least 2 mm	$b_{ss1}k_{open} \geq 2\text{ mm}$	
	slot opening height at least 2 mm	$h_{so} \geq 2\text{ mm}$	
avoid magnetic saturation	flux density in stator teeth under 1.6 T	$B_{ts} \leq 1.6\text{ T}$	from the iron
	flux density in stator yoke under 1.4 T	$B_{sy} \leq 1.4\text{ T}$	magnetization
	flux density in rotor yoke under 1.4 T	$B_{ry} \leq 1.4\text{ T}$	curve
	fundamental airgap flux density under 1.1 T	$\hat{B}_\delta \leq 1.1\text{ T}$	
prevent high temperature and	winding temperature set to 80 °C	$T_{cu} = 80\text{ °C}$	Appendix D
guarantee a minimal efficiency	copper losses under 700 W	$P_{cu} \leq 700\text{ W}$	figure 4.4
limit the price	magnet weight under 5.5 kg	$m_{mag} \leq 5.5\text{ kg}$	figure 4.3
limit the machine weight	machine weight under 150 kg	$m_{tot} \leq 150\text{ kg}$	table 1.2

4.2 Results and comparison of designs with distributed windings

In this section, the results obtained by following the design optimization procedure are presented. The designs that will be compared have a distributed stator winding with either $q = 1$ or $q = 2$. In the first part, explanations regarding the choice of some constraints will be given. In the second part, the different designs will be compared.

4.2.1 Influence of some of the constraints

Maximum permanent magnet weight

Since the price of PM material is high compared to the rest of the machine materials, the weight of the permanent magnets should be limited as much as possible. However, the lower their weight, the higher will be the total active weight (figure 4.3). A lower flux from the permanent magnets is indeed compensated by a higher armature reaction, resulting in bigger slots and consequently a bigger stator. As a compromise, the maximum permanent magnet weight is chosen as 5.5 kg.

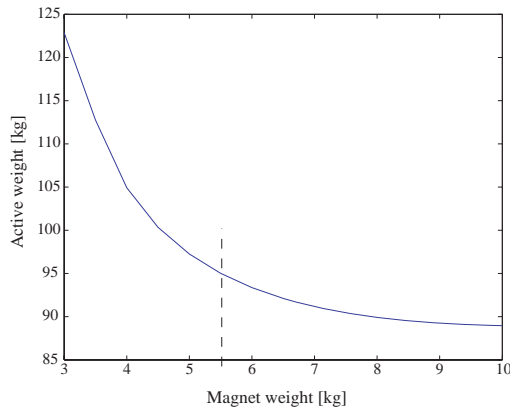


Figure 4.3: Active weight as a function of the permanent magnet weight for optimized 60-pole SMPM motors.

Maximum copper losses

The copper losses should be as low as possible to assure a good efficiency. However, the lower the copper losses, the higher will be the active weight of the machine (figure 4.4). A compromise has to be found between efficiency and active weight of the machine. The limit for the copper losses is set to 700 W.

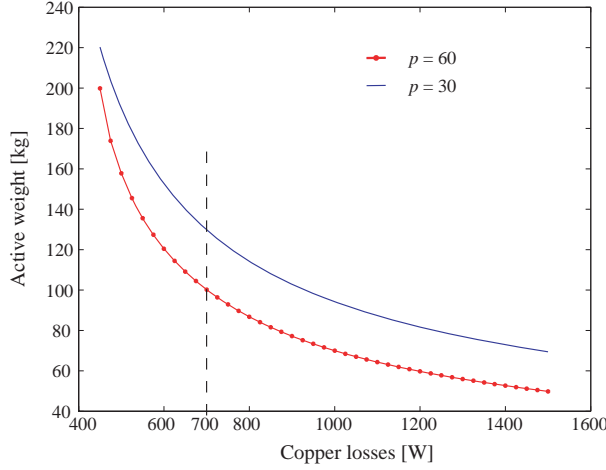


Figure 4.4: Active weight of optimized SMPM motor designs as a function of the copper losses.

Constraints on the rigidity of the structure

In [19], a 45 kW, 600 rpm buried V-shaped PM motor was investigated. The same constraints on the rigidity of the structure as in [19] were considered. These constraints are thus not optimized for the specific design requirements. Figure 4.5 gives an idea of what happens without constraints on the rigidity of the structure. It shows two designs of a 50-pole SMPM machine obtained by following the optimization procedure. The first one respects all the constraints described previously. The second one does not respect the constraints on the rigidity of the structure. The teeth are very long and thin and the stator back is very thin. In this case, the flux leakage through the teeth is slightly higher. The second design is also much shorter.

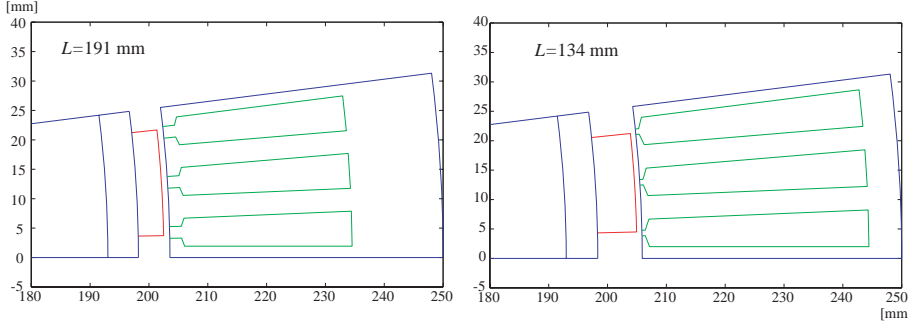


Figure 4.5: Two optimized designs of a 50-pole SMPM motor, with and without the mechanical constraints on the structure.

Copper temperature

The copper temperature is determined by the copper losses, the environmental temperature and the cooling of the motor. The copper temperature was chosen equal to 80°C as described in appendix D. Figure 4.6 shows the active weight as a function of the copper temperature for optimized 60-pole SMPM motors. The higher the copper temperature, the higher the resistivity of the copper and thus the copper resistance. This implies that the slot area must become bigger for constant copper losses. Therefore the active weight increases with an increasing copper temperature. If the estimation of the copper temperature were incorrect, the curve of figure 4.6 shows how it would affect the active weight of the motor.

4.3 Comparison of the configurations

In this section, the obtained designs from the optimization program for different radial-flux PM motors are compared to each other. First, the active weight as a function of the pole number is provided for the different configurations. Then, the torques of several selected machines, computed with FEM simulations, are analyzed.

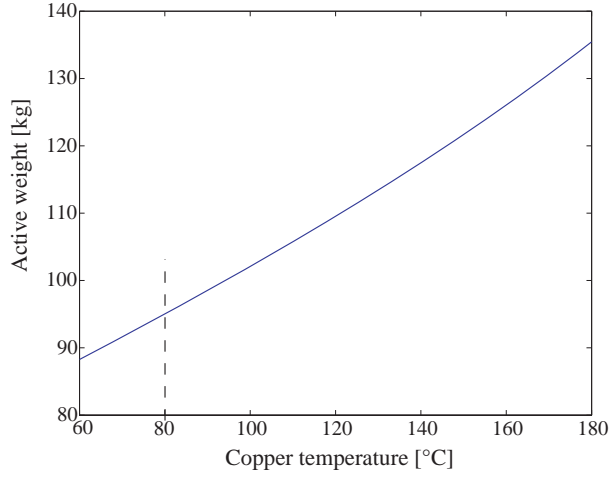


Figure 4.6: Active weight as a function of the copper temperature for optimized 60-pole SMPM motor designs.

4.3.1 Weight and pole number

Figure 4.7 shows the dependency of the total active weight on the number of poles for different optimized designs. In the following, the resulting curves are discussed.

Influence of the constraints

The total active weight of the inset PM and tangentially-magnetized PM motors reaches a minimum at a pole number of 70 and 60 respectively. This is due to the constraints that guarantee the rigidity of the structure (table 4.4). As soon as the limit on one or more of these constraints is reached, the active weight increases. For the inset PM designs for example, the tooth width reaches its lower limit. Consequently, the length of the motor is increased to fulfill the torque requirement and the active weight increases.

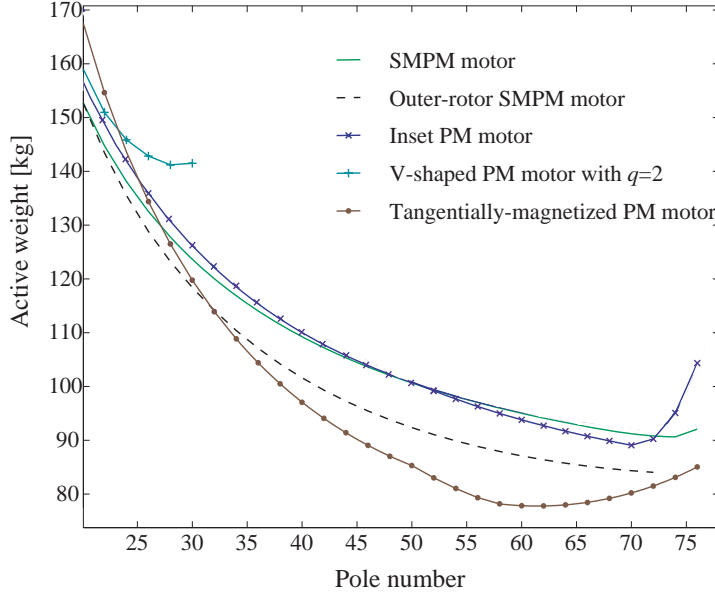


Figure 4.7: Active weight as a function of the number of poles for different optimized designs.

Flux concentration

The topology that is the lightest for a pole number over 34 is the tangentially-magnetized PM motor. This is due to the fact that the flux concentration in the rotor allows a higher flux density in the airgap and thus a lower machine length (table 4.5). Therefore, the flux concentration is a non-negligible advantage.

Table 4.5: Comparison of different motor configurations with $p = 50$.

	SMPM	Outer rotor SMPM	Inset PM	Tangentially- magnetized PM
B_δ [T]	0.911	0.857	0.906	1.12
L [mm]	191	179	199	144

V-shaped PM motors

Optimized designs of V-shaped PM motors with $q = 1$ were investigated with FEM simulations. The obtained torque ripples were extremely high (over 100 % of the nominal torque). This may be explained by the high harmonic content in the airgap flux density, notably the amplitude of the fifth harmonic that is over 25 % of the fundamental. By choosing $q = 2$, the torque ripple becomes more reasonable. However there were no solutions found for pole numbers higher than 30, as the teeth become too numerous, too narrow and saturated (figure 4.7). Thus, V-shaped PM motor designs are not suitable for low-speed direct drives.

Comparison inner/outer rotor

As can be seen in figure 4.7, the outer-rotor SMPM motor configuration is lighter than the inner-rotor SMPM motor. Indeed, an outer-rotor geometry allows a larger inner stator diameter and thus decreases the current loading needed to obtain the required torque (3.37).

Comparison of SMPM and inset PM motors

Figure 4.7 also reveals that the SMPM and the inset PM motor configurations have almost the same weight for equal permanent magnet weight and copper losses. The inset PM rotor is heavier than the SMPM rotor due to the iron pieces placed between the permanent magnets. However, the inset PM motor is slightly lighter than the SMPM motor for pole numbers over 50. This is due to the reluctance torque that contributes around 5 % to the required nominal torque. This allows a lighter stator, and explains why the inset PM motor can be lighter than the SMPM motor.

Choice of the pole number

Figure 4.7 can be used to choose an optimal pole number. However, it should be kept in mind that the number of permanent magnets and the production cost increase with a higher pole number. Therefore a compromise should be found between the weight and the number of magnets.

For pole numbers higher than 50, the active weight decreases slower due to the constraints on the structure. A minimum weight under 80 kg is reached for the 60-pole tangentially-magnetized PM motor design.

4.3.2 Torque ripple

The torque is pulsating because of:

- The variation of permeance in the airgap, generating the cogging torque.
- The interaction between the airgap flux and the space harmonics in the magneto-motive force (MMF) depending on the winding layout.
- The interaction of the airgap flux with the current harmonics. The current harmonics generated by voltage harmonics are neglected here, as the supplied voltage is assumed to be ideally sinusoidal.

The torque ripple is obtained from a time-step constant-speed FEM simulation (Appendix B). The simulated designs have the same winding layout (distributed winding, $q = 1$) and have almost the same airgap length. Table 4.6 provides the ratio between the torque ripple and the mean torque for three different pole numbers and different motor topologies. The corresponding curves are displayed in figure 4.8. The ratio between the cogging torque and the mean torque for different 50-pole motor designs are provided in table 4.7.

Table 4.6: Ratio between the torque ripple and the mean torque in %.

	SMPM	Outer-rotor SMPM	Inset PM	Tangentially- magnetized PM
$p = 30$	19	28	24	70
$p = 50$	16	27	20	46
$p = 70$	10	26	22	47

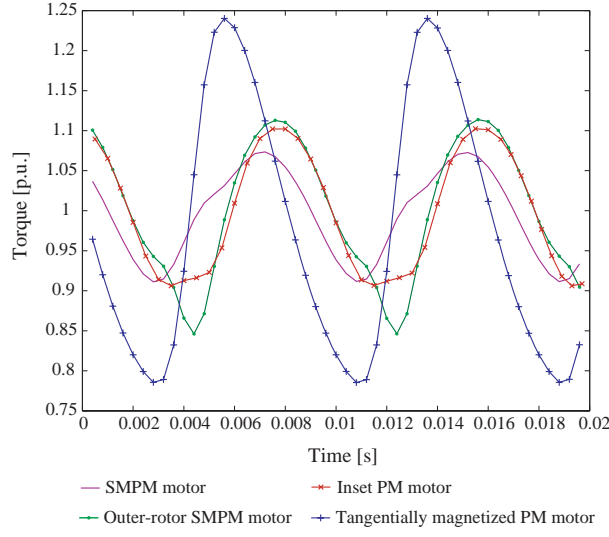


Figure 4.8: FEM simulated torque for different configurations of 50-pole PM motors, at nominal load.

Table 4.7: Ratio between the cogging torque and the mean torque in %.

	SMPM	Outer-rotor SMPM	Inset PM	Tangentially- magnetized PM
$p = 50$	3.9	4.2	2.6	12.9

The torque ripple varies between different configurations and pole numbers. The SMPM motor designs have the lowest torque ripple. The very high torque ripple of the tangentially-magnetized PM motors can partly be explained by their higher cogging torque (table 4.7). As stated before, the airgap flux plays also an important role in the torque pulsation. Therefore, the relevant low-order harmonics in the airgap flux density are provided in table 4.8. The difference of harmonic contents reflects well the difference in the torque ripple if the contribution of the cogging torque is kept in mind. For example, the torque ripple of the SMPM motor with 30 poles is higher than the ripples of the 50- and 70-pole SMPM motors. This is reflected in the amplitudes of their 3^{rd} , 5^{th} and 7^{th} harmonics in the airgap flux density, which are also higher.

Table 4.8: Relative values of the 3^{rd} , 5^{th} and 7^{th} harmonics in the airgap flux density in %.

		SMPM	Outer-rotor SMPM	Inset PM	Tangentially- magnetized PM
3^{rd} harmonic	$p = 30$	5.0	0	1.5	16.1
	$p = 50$	5.0	0	0.8	13.1
	$p = 70$	4.5	0	1.5	14.6
5^{th} harmonic	$p = 30$	15.2	18.9	17.9	8.7
	$p = 50$	13.6	17.0	17.9	12.7
	$p = 70$	13.4	16.0	18.1	12.2
7^{th} harmonic	$p = 30$	9.0	9.0	10.9	4.5
	$p = 50$	4.5	5.6	7.2	2.3
	$p = 70$	1.0	1.9	3.6	0.8

Table 4.9: Torque ripple and low-order harmonics in the airgap flux density of two 50-pole SMPM motors with different pole angles

Torque ripple [%]	2α [el. °]	Harmonic no. [%]					Active weight [kg]
		3^{rd}	5^{th}	7^{th}	9^{th}	11^{th}	
22.7	120	0	16.1	3.5	0	6.4	101.2
16.3	126	5	13.6	4.5	2.2	4.9	100.7

The harmonic contents in the airgap flux-density can be influenced by varying the pole angle. A pole angle of 120 electrical degrees allows to eliminate the third harmonic, as it was done for the outer-rotor SMPM motors in table 4.8. Table 4.9 shows the influence of the pole angle (2α) on the harmonics in the airgap flux-density and on the torque ripple of 50-pole SMPM motors. The active motor weight is given to indicate which design was the calculated optimal solution. As can be seen, the motor with a pole angle of 120 electrical degrees has higher 5^{th} and 11^{th} harmonics than the other simulated design and also a higher torque ripple. Therefore, the torque ripple of SMPM motors can be optimized by finding a pole angle that gives a compromise between the amplitudes of the 3^{rd} and 5^{th} harmonics.

For the outer-rotor SMPM motor, the calculated optimal design has a pole angle that is lower than 120 electrical degrees, which should be avoided according to table 4.10. Indeed, both the 3^{rd} and the 5^{th} harmonics are very high for low pole angles, causing a high torque ripple. For outer-rotor SMPM motors, the lower limit of the pole angle in the optimization program is therefore changed to 120 electrical degrees to avoid very high torque ripples.

Table 4.10: Torque ripple and low-order harmonics in the airgap flux density of three 50-pole outer-rotor SMPM motors with different pole angles

Torque ripple [%]	2α [el. °]	Harmonic no. [%]					Active weight [kg]
		3^{rd}	5^{th}	7^{th}	9^{th}	11^{th}	
49.7	110.4	8.8	19.6	13.2	4.0	6.6	89.7
26.7	120	0	17	5.6	0	6.6	90.5
27.0	126	5.3	15	7.2	3.0	5.6	91.8

For the tangentially-magnetized PM motors, the pole angle is also influencing the torque ripple. However, no torque ripple lower than 40 % of the nominal torque was found by trying different values of pole angles and decreasing the cogging torque as much as possible.

For all investigated motor configurations, the torque ripple was found to be relatively high (over 10 %), even though the pole angle was optimized for a low torque ripple.

The torque ripple can be decreased by skewing the machine, which was not investigated in this thesis. Another solution that will be investigated in chapter 5 is to use a concentrated winding with a good combination between the pole number and the slot number. The influence of different stator tooth widths on the torque ripple is also considered in chapter 5.

4.3.3 Iron losses

The iron losses are calculated using FEM simulations as described in appendix B. No big difference between the different designs can be noticed and iron losses of about 120 W have been found, which is around one sixth of the value of the copper losses.

4.3.4 Summary

Different motor configurations were compared for stators with distributed windings with $q = 1$ and $q = 2$. Several interesting aspects have been pointed out.

The V-shaped PM motors are not adapted for high pole numbers (over 30) because of a too high torque ripple.

Inner- and outer-rotor SMPM motor, inset PM motor and tangentially-magnetized PM motor designs fulfill the given constraints. The calculated active weights are between 80 and 100 kg, which is far below the limit of 150 kg. Since the inset PM motor is nearly equivalent to the SMPM motor in terms of active weight and performance, it will not be studied further.

However, all designs have the same drawback: a very high torque ripple. The torque ripple was not taken into account when defining the constraints, because it is difficult to calculate analytically. Nevertheless, it should be as small as possible to guarantee the motor a maximum life time. Therefore, the motor designs need to be improved. A good way to decrease the torque ripple, besides skewing, is the use of concentrated windings.

Concentrated windings for inner- and outer-rotor SMPM motors as well as tangentially-magnetized PM motors are studied in the next chapters. V-shaped PM motor and inset PM motor designs are not considered further.

5 Concentrated windings

In this thesis, a concentrated winding is a winding that is concentrated around the teeth. It has no overlapping end-windings. Several advantages make the concentrated windings interesting:

- Their end-windings are much shorter than those of distributed windings. As a consequence, the copper losses are lower.
- They can be mounted very easily around the teeth since the end-windings are not overlapping. This simplifies the production and reduces the cost.
- Some configurations enable a low torque ripple.

However, concentrated windings have also some drawbacks. The number of poles and the number of slots have to be chosen carefully. Otherwise, the winding factor may be low, the torque ripple and the rotor losses high and the machine may be very noisy.

Concentrated windings are not a recent discovery; they are first mentioned in a patent from the year 1895, [42]. In the nineties they were used in sub-fractional power machines with a reduced number of phases. The studies for larger three-phase machines started in 2002 to become very trendy. In 2002, J. Cros and P. Viarouge showed how to find winding layouts that have high winding factors [43]. The applied methods were to use an irregular teeth distribution or to find a good combination of pole and slot numbers. Winding factors for motors with up to 22 poles were presented. The same year, Th. Koch and A. Binder compared two designs of PM machines for electric traction, one with $p = 28$, $q = 0.25$ and irregularly distributed teeth, one with $p = 28$, $q = 0.5$ and double-layer windings [44]. In 2003,

F. Magnussen calculated the winding factors for one-layer and double-layer windings up to 16 poles and compared some designs [37]. In [45], three designs were compared with 14 poles and 42, 21 and 15 slots. Torque ripple, losses and thermal behavior were investigated. In [46], D. Ishak looked at the combinations of poles and stator slots linked by the relation $p = Q_s \pm 2$. Concentrated windings were also studied in combination with soft magnetic composite (SMC) materials by A.G Jack [41], [47]. Different pole-slot number combinations were compared for an 8-pole motor in [47]. Some multi-phase concentrated windings were investigated in [48] and [49].

Concentrated windings are appropriate for PM machines with high pole numbers and therefore highly interesting for low-speed direct drives. As mentioned previously, some pole-slot number combinations were studied for pole numbers lower than 20. In this chapter, the main goal is to find winding configurations that give high winding factors for pole numbers higher than 20. Winding configurations with high torque ripples, excessive rotor losses or noise should be avoided. The method with irregularly distributed teeth described in [43] is tested first and then pole-slot number combinations for pole numbers over 20 are investigated. Some hints are given to avoid bad combinations.

5.1 Irregularly distributed teeth

A first possibility to obtain a high winding factor with a concentrated winding is to have an irregular distribution of teeth [43]. The windings investigated in this part have a number of slots per pole per phase equal to 0.5, which is easier to handle because of the symmetries in these windings.

5.1.1 Winding factor

The fundamental winding factor can be calculated using the MMF waves. Figure 5.1 shows the MMF wave created by the stator currents at the instant where the current in phase A is maximal and equal to the rated peak current \hat{I} . The currents in phases B and C are equal to $-\hat{I}/2$. In the first case, the

teeth are of equal size, in the second case the teeth are irregularly distributed. The fundamental winding factor k_{w1} is equal to the ratio of the amplitude of the MMF harmonic corresponding to the number of poles, divided by the fundamental of the MMF of the distributed winding with $q = 1$. The winding factor has been calculated for different cases of irregularly distributed teeth with $q = 0.5$. Table 5.1 presents the obtained results for different ratios between the smaller tooth width b_{t1} and the wider one b_{t2} .

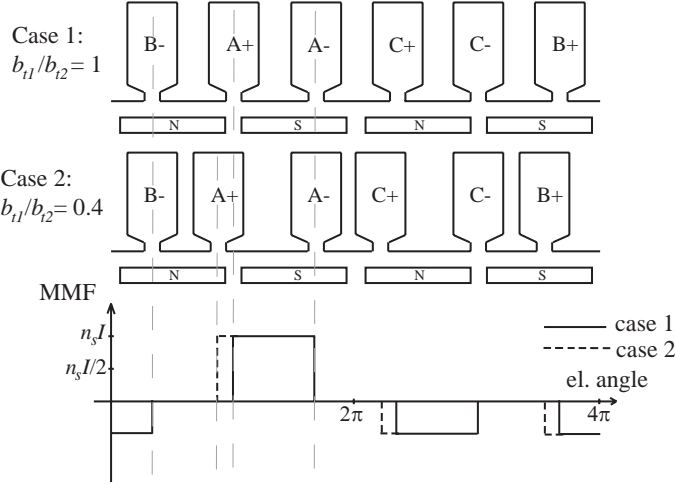


Figure 5.1: Calculation of the winding factor for two different cases of irregularly distributed teeth with $q = 0.5$.

Table 5.1: Winding factors for different cases of irregularly distributed teeth with $q = 0.5$.

Tooth ratio b_{t1}/b_{t2}	1	0.8	0.7	0.6	0.5	0.4
Winding factor	0.866	0.894	0.909	0.924	0.940	0.956

5.1.2 Influence on the torque ripple

The load torques of a 64-pole SMPM motor were computed for different teeth distributions at the same current loading. The results are given in table 5.2. As can be seen, the special teeth distribution allows not only a better winding factor but also a lower torque ripple. However, the lowest torque ripple for a tooth ratio of 0.4 is still quite high with 13 % of the nominal torque. The tooth ratio was not checked under 0.4 as the teeth are already very saturated and thin for this value. As will be shown in the next section, lower torque ripples can be achieved with a good slot-pole number combination, and regularly distributed teeth.

Table 5.2: Torque values for different teeth distribution.

Tooth ratio b_{t1}/b_{t2}	Winding factor k_{w1}	Torque [p.u.]	Torque ripple [%]
1	0.866	0.90	49
0.8	0.894	0.94	46
0.6	0.924	0.98	32
0.4	0.956	1.00	13

5.2 Combinations of pole and slot numbers

The aim of this section is to sort out the different winding layouts and possible slot-pole number combinations in order to simplify the choice of a layout. For this purpose, the winding factors of the investigated concentrated windings, the harmonic contents of the respective MMFs, their torque ripples and radial magnetic forces are calculated and analyzed for some promising slot-pole number combinations.

5.2.1 Winding layouts and winding factors

Determination of the winding layout for a double-layer winding

Double-layer windings have been investigated since they have better properties such as shorter end-windings and more sinusoidal back-EMF waveforms compared to single-layer windings [37], [46]. For different slot-pole number combinations, the winding layout, i.e. the placement of the conductors of each phase in the slots, is determined. The method presented in [43] describes how to obtain the layout that gives the highest winding factor for a given pole number p and slot number Q_s . The method is based on the decomposition of the number of slots per pole per phase q . It is similar to the method used for the large synchronous machines with a fractional value of q [40]. The method is described in figure 5.2 using $Q_s = 24$ and $p = 26$ as an example.

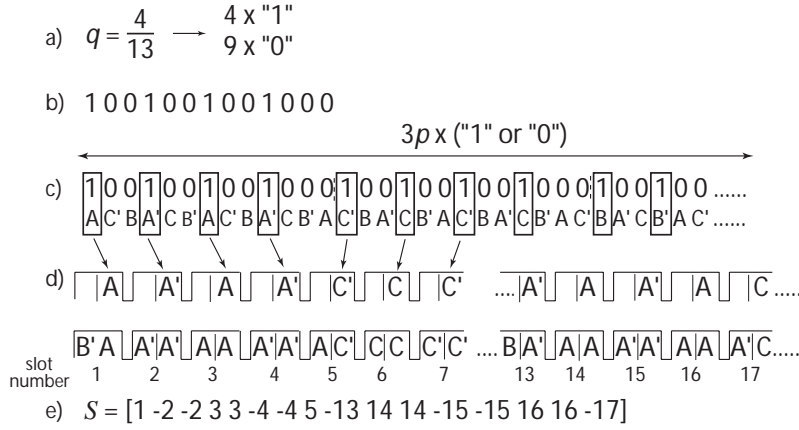


Figure 5.2: Determination of the winding layout for $Q_s=24$ and $p = 26$.

- a) The number of slots per pole per phase q is written as a fraction which is cancelled down to its lowest terms: $q = n/d = 4/13$ where n and d are integers.
- b) A sequence of $d - n = 9$ zeros ("0") and $n = 4$ ones ("1") is found, the ones being distributed in the sequence as regularly as possible.

- c) The found sequence is repeated $3p/d = Q_s/n = 6$ times. It is compared to the layout of the distributed winding with $3p$ slots and $q = 1$.
- d) Those conductors from the distributed winding that correspond to the "1" are kept and form one layer of the double-layer concentrated winding. The second winding layer is obtained by writing the corresponding return conductor on the other side of the tooth for every obtained conductor, i.e. A' for A.
- e) A vector S is written to describe the layout of phase A. It will be used to calculate the winding factor. Thereby, the slots are numbered from 1 to Q_s . The vector S consists of the numbers corresponding to these slots that contain conductors of the phase A. If both layers of one slot contain conductors of phase A, the number of the slot is written twice in the vector. S has thus $2Q_s/3$ elements. For conductors A', a minus is added to the corresponding slot number.

Method used to calculate the winding factor

The winding factor is calculated using the EMF phasors [37]. The corresponding EMF phasor \vec{E}_i of conductor i is:

$$\vec{E}_i = \text{sign}(S(i)) e^{j \frac{\pi p}{Q_s} |S(i)|} \quad (5.1)$$

The fundamental winding factor k_{w1} can then be calculated:

$$k_{w1} = \frac{1}{n_l Q_s / 3} \left| \sum_{i=1}^{2Q_s/3} \vec{E}_i \right| \quad (5.2)$$

where i is an element of S and n_l is the number of layers ($n_l = 2$).

For the example with $Q_s = 24$ and $p = 26$, the sum of the EMF phasors is:

$$\begin{aligned} \sum_{i=1}^{16} \vec{E}_i = & e^{j \frac{\pi p}{Q_s}} + 2e^{-2j \frac{\pi p}{Q_s}} + 2e^{3j \frac{\pi p}{Q_s}} + 2e^{-4j \frac{\pi p}{Q_s}} + e^{5j \frac{\pi p}{Q_s}} + e^{-13j \frac{\pi p}{Q_s}} \\ & + 2e^{14j \frac{\pi p}{Q_s}} + 2e^{-15j \frac{\pi p}{Q_s}} + 2e^{16j \frac{\pi p}{Q_s}} + e^{-17j \frac{\pi p}{Q_s}} \end{aligned} \quad (5.3)$$

This results in a winding factor of 0.95.

Calculation of the winding factor

Winding factors for machines from 4 to 80 poles and 6 to 90 slots are calculated. This represents a total of 935 pole-slot number combinations. Figures 5.4 and 5.5 show the fundamental winding factors calculated for double-layer concentrated windings with p between 20 and 80, and Q_s between 15 and 90, with Q_s being a multiple of 3. The method presented above to find the winding layout with the highest winding factors does not need to be applied for every single combination. Indeed, winding factors of some pole-slot number combinations can be found directly:

- Some combinations do not give a balanced three-phase winding. It is the combinations where the denominator d ($q = n/d$) is a multiple of the number of phases. They are colored red in figures 5.4 and 5.5.
- Combinations with the same number of slots per pole per phase have equal winding factors. These winding layouts consist of the same basic sequence reproduced a certain number of times to fill the required number of slots (see table 5.3)
- For each Q_s , i.e. each line of the table, there is a periodicity of $2Q_s$: The winding layout and factors of the pole-slot number combinations with Q_s slots and $p + 2kQ_s$ poles ($k=0,1,2,\dots$) are identical. This is easily shown with equations (5.2) and (5.4):

$$\forall i : e^{j \frac{p\pi}{Q_s} S(i)} = e^{j \frac{p\pi}{Q_s} S(i)} \underbrace{e^{j 2\pi S(i)}}_{=1} = e^{j \frac{\pi(p+2Q_s)}{Q_s} S(i)} \quad (5.4)$$

- For each Q_s , i.e. each line of the table, there is a symmetry around kQ_s ($k = 1,2,3,\dots$). Pole-slot number combinations with $p = Q_s - k$ and $p = Q_s + k$, ($k = 1,2,3,\dots$) have an identical layout and winding factor.

This is proved below:

$$\begin{aligned}
 \left| \sum_i e^{j \frac{p \pi S(i)}{Q_s}} \right| &= \left| \sum_i \cos \frac{p \pi S(i)}{Q_s} + j \sum_i \sin \frac{p \pi S(i)}{Q_s} \right| \\
 &= \left[\left(\sum_i \cos \frac{p \pi S(i)}{Q_s} \right)^2 + \left(\sum_i \sin \frac{p \pi S(i)}{Q_s} \right)^2 \right]^{1/2} \quad (5.5)
 \end{aligned}$$

For $p = Q_s - k$, the sum of cosinus and sinus terms can be rewritten as:

$$\begin{aligned}
 \sum_i \cos \frac{\pi(Q_s - k)S(i)}{Q_s} &= \sum_i \left(\cos(\pi S(i)) \cos \frac{\pi k S(i)}{Q_s} + \underbrace{\sin(\pi i) \sin \frac{\pi k S(i)}{Q_s}}_{=0} \right) \\
 &= \sum_i \cos \frac{\pi(Q_s + k)S(i)}{Q_s} \quad (5.6)
 \end{aligned}$$

$$\begin{aligned}
 \sum_i \sin \frac{\pi(Q_s - k)S(i)}{Q_s} &= \sum_i \left(\underbrace{\sin(\pi S(i)) \cos \frac{\pi k S(i)}{Q_s}}_{=0} - \sin \frac{\pi k S(i)}{Q_s} \cos(\pi S(i)) \right) \\
 &= - \sum_i \sin \frac{\pi(Q_s + k)S(i)}{Q_s} \quad (5.7)
 \end{aligned}$$

This leads to:

$$\left| \sum_i e^{j \frac{\pi(Q_s - k)}{Q_s} S(i)} \right| = \left| \sum_i e^{j \frac{\pi(Q_s + k)}{Q_s} S(i)} \right| \quad (5.8)$$

which means that the winding factors for $p = Q_s - k$ and $p = Q_s + k$, with $k = 1, 2, 3, \dots$ are identical.

- It has been noticed that the winding factor increases and decreases as shown in figure 5.3. Figure 5.3 shows also the symmetries and periodicity described previously.

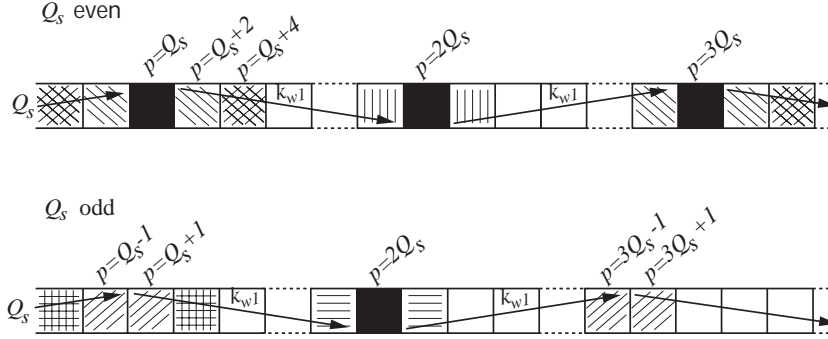


Figure 5.3: Evolution of the winding factor k_{w1} for even and odd slot numbers Q_s and different pole numbers p

(Boxes filled with the same pattern have the same winding factor and layout. Black boxes are combinations where concentrated windings are not possible.)

Figures 5.4 and 5.5 show that winding factors up to 0.954 can be reached. Some interesting winding layouts are described in table 5.3. In the following, the windings presenting high winding factors where p and Q_s are approximately equal will be investigated further.

$Q_s \backslash p$	4	6	8	10	12	14	16	18	20	22	24	26	28	30	32	34	36	38	40
6	0.866	0.866	0.866	0.5	0.866	0.5	0.866	0.5	0.866	0.5	0.866	0.5	0.866	0.5	0.866	0.5	0.866	0.5	0.866
9	0.617	0.866	0.945	0.866	0.617	0.328	0.866	0.328	0.866	0.617	0.866	0.945	0.945	0.866	0.617	0.328	0.866	0.328	0.617
12	$q=1$	0.866	0.933	0.866	0.933	0.951	0.866	0.866	0.933	0.866	0.933	0.933	0.933	0.866	0.866	0.933	0.933	0.933	0.866
15		0.621	0.866	0.866	0.866	0.951	0.951	0.866	0.866	0.621	0.866	0.647	0.866	0.866	0.866	0.866	0.866	0.621	0.866
18		$q=1$	0.647	0.866	0.866	0.902	0.945	0.866	0.945	0.902	0.866	0.647	0.866	0.866	0.866	0.866	0.866	0.866	0.866
21				0.866	0.866	0.866	0.89	0.866	0.953	0.953	0.866	0.89	0.866	0.866	0.866	0.866	0.866	0.866	0.866
24			$q=1$		0.866	0.76	0.866	0.866	0.933	0.95	0.866	0.95	0.933	0.866	0.866	0.76	0.866	0.866	0.866
27								0.866	0.877	0.915	0.945	0.954	0.954	0.945	0.915	0.877	0.866	0.874	0.866
30				$q=1$					0.866	0.874	0.866	0.936	0.951	0.866	0.951	0.936	0.866	0.874	0.866
33										0.866	0.866	0.903	0.928	0.866	0.954	0.954	0.928	0.928	0.903
36					$q=1$						0.866	0.867	0.902	0.933	0.945	0.953	0.866	0.953	0.945
39												0.866	0.863	0.866	0.918	0.936	0.866	0.954	0.954
42						$q=1$							0.866	0.866	0.89	0.913	0.866	0.945	0.953
45														0.866	0.859	0.886	0.866	0.927	0.945
48							$q=1$								0.866	0.857	0.866	0.905	0.933
51																0.866	0.88	0.88	0.901
54								$q=1$									0.866	0.854	0.877
57																		0.866	0.852
60									$q=1$										0.866

$q=1/2, 1/4$	$q=3/8, 3/10$	$Q_s=21+6k, p=Q_s \pm 1, k=0, 1, 2, \dots$
$q=3/7, 3/11$	$q=5/14, 5/16$	$Q_s=24+6k, p=Q_s \pm 2, k=0, 1, 2, \dots$
$q=2/5, 2/7$	not appropriate	$kw1 < 0.866$

Figure 5.4: Winding factors for different pole-slot number combinations.

$Q_s \backslash b$	42	44	46	48	50	52	54	56	58	60	62	64	66	68	70	72	74	76	78	80
33	0.866	0.866	0.867	0.866																
36	0.933	0.902	0.867	0.866																
39	0.936	0.918	0.863	0.866	0.863	0.866														
42	0.953	0.945	0.913	0.89	0.913	0.89		0.866												
45	0.951	0.955	0.955	0.951	0.945	0.927		0.886	0.859	0.866										
48	0.95	0.954	0.954	0.954	0.954	0.95		0.933	0.905	0.857	0.866									
51	0.933	0.944	0.944	0.944	0.955	0.955		0.944	0.933	0.901	0.88			0.866						
54	0.902	0.915	0.93	0.945	0.949	0.954		0.954	0.949	0.945	0.93	0.915	0.902	0.877	0.854	0.866				
57	0.932	0.912	0.937	0.946	0.937	0.946		0.955	0.955	0.946	0.937			0.912	0.932		0.852	0.866		
60	0.874	0.892	0.933	0.936	0.933	0.936		0.951	0.954	0.954	0.951			0.936	0.933		0.892	0.874		0.866
63	0.866	0.85	0.871	0.89	0.905	0.919		0.945	0.948	0.953	0.955	0.955	0.953	0.948	0.945		0.919	0.905	0.89	0.871
66	0.866	0.849	0.866	0.866	0.887	0.903		0.928	0.938	0.951	0.954			0.954	0.951		0.938	0.928		0.903
69	0.866	0.866	0.866	0.866	0.867	0.884		0.914	0.925	0.943	0.949			0.955	0.955		0.949	0.943		0.925
72	0.866	0.847	0.867	0.867	0.867	0.867		0.902	0.911	0.933	0.933	0.945	0.95	0.953	0.954		0.954	0.953	0.95	0.945
75	0.866	0.846	0.866	0.846	0.866	0.846		0.88	0.895	0.92	0.93			0.945	0.951		0.955	0.955	0.951	0.951
78	0.866	0.866	0.866	0.866	0.866	0.866		0.863	0.879	0.906	0.918			0.936	0.943		0.952	0.954	0.954	0.954
81	0.866	0.866	0.866	0.866	0.866	0.866		0.845	0.86	0.877	0.89	0.904	0.915	0.925	0.933	0.945	0.946	0.951	0.954	0.955
84	0.866	0.866	0.866	0.866	0.866	0.866		0.866	0.845	0.876	0.89			0.913	0.933		0.939	0.945		0.953
87	0.866	0.866	0.866	0.866	0.866	0.866		0.866	0.866	0.859	0.874			0.899	0.91		0.929	0.936		0.947
90	0.866	0.866	0.866	0.866	0.866	0.866		0.866	0.866	0.843	0.859	0.874	0.874	0.886	0.902		0.918	0.927	0.936	0.945

Figure 5.5: Winding factors for different pole-slot number combinations, continued.

Table 5.3: Winding layouts for some pole-slot number combinations

(A' stands for the return conductor corresponding to conductor A).

Q_s, p or q	Winding layout
$q = 2/5, 2/7$	$\dots C' A A' A' AB' BB' B'C' C'C' CA' AA A'B B'B' BC' CC \dots$
$q = 3/8, 3/10$	$\dots C' A A' A' AA A'B B'B' BB B'C' C'C' CC \dots$
$q = 3/7, 3/11$	$\dots C' A AB' BB' BB' B'C' CA A'A' AB' BC' CC C'A A'B B'B' BC' CA' AA A'B B'C' C'C' \dots$
$q = 5/14, 5/16$	$\dots C' A A' A' AA A'A' AA A'B B'B' BB B'B' BB B'C' C'C' CC C'C' CC \dots$
$Q_s = 12 + 6k, p = Q_s \pm 2$ if $p/2$ even	$\dots \underbrace{A A'A' A\dots A A'A' A'B' BB B'\dots B' BB B'C' C'C' C\dots C C'C' C}_{Q_s/6} \dots$
if $p/2$ odd	$\underbrace{A A'A' A\dots A' AA A'A' B BB B'\dots B' B' B'C' C'C' C\dots C' C' A'}_{Q_s/6} \underbrace{C' CC C' A'}_{Q_s/6} \underbrace{A B \dots B' C'\dots C'}_{Q_s/6}$
$Q_s = 9 + 6k, p = Q_s \pm 1$	$\underbrace{A A'A' A\dots A' AA A'A' B B' B' B\dots B' B' BB B'C' C'C' C\dots C' CC C'}_{Q_s/3} \underbrace{C' CC C'}_{Q_s/3}$

5.2.2 MMF and harmonics

Analysing the MMF and its harmonics is of interest since it can cause extra iron losses in the rotor compared to distributed windings. The MMF is calculated analytically with the method fully described in [37]. The harmonics are calculated by taking the periodicity of the MMF waveform into account, which corresponds to the number of symmetries in the winding. Independently of the number of poles, one period of the MMF waveform is taken as the base time frame. This has the advantage that the harmonic orders are integers. The harmonic interacting with the permanent magnet flux and producing the average value of the torque is then the harmonic, whose number is equal to the ratio between the number of poles and the number of periods in the MMF.

Figure 5.6 shows the harmonic content in the MMF for two machines with double-layer concentrated windings with 48 slots/40 poles ($q = 2/5$) and 51 slots/50 poles. The torque harmonics are the 10th and the 50th harmonics, for the 40-pole and 50-pole motor designs respectively. As can be seen in the figures, the MMFs contain many harmonics with high amplitude. The winding without symmetries also contains many more harmonics than the one with symmetries (figure 5.6).

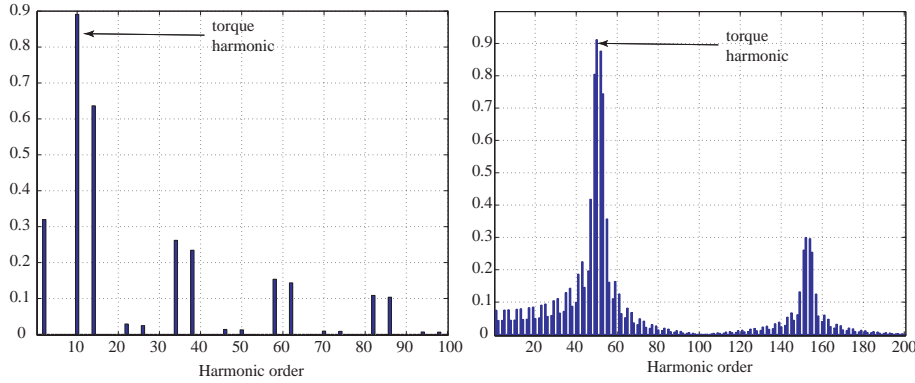


Figure 5.6: MMF harmonics in double-layer concentrated windings with 48 slots and 40 poles ($q = 2/5$) on the left and 51 slots and 50 poles on the right.

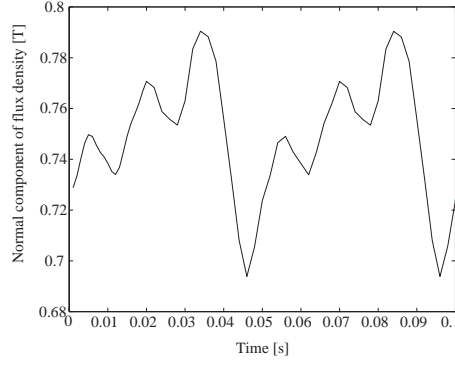


Figure 5.7: Time variation of the normal component of the total flux density in the middle of the rotor iron between two permanent magnets, for a motor with $Q_s = 72$ and $p = 64$.

Due to MMF harmonics, alternating magnetic fields appear in the rotor. As can be seen in figure 5.7, the flux density in the rotor is not constant. This gives rise to eddy currents in the permanent magnets as well as iron losses in the rotor iron. Therefore, these losses should be estimated during the design process when concentrated windings are applied. If they are too high, a laminated rotor and permanent magnets in smaller pieces can decrease the losses.

5.2.3 Torque ripple

Cogging torque

A very low cogging torque can be obtained if the slot and pole numbers are chosen so that the least common multiple (LCM) between them is large [37]. Windings with $q = 2/5$ and $q = 3/8$ have a lower LCM than other windings and consequently have a higher cogging torque (table 5.4). The closer the number of slots to the number of poles, the higher the LCM. Even though the combinations $p = Q_s - k$ and $p = Q_s + k$ have equal winding factors, the LCM is higher for $p = Q_s + k$ than for $p = Q_s - k$.

Table 5.4: Lowest common multiple and cogging torque in % of the rated torque of different SMPM motors.

p, Q_s, q	LCM	Cogging torque [%]
$p = 60, Q_s = 72, q = 2/5$	360	1.4
$p = 64, Q_s = 72, q = 3/8$	576	0.3
$p = 64, Q_s = 60, q = 5/14$	960	0.03
$p = 64, Q_s = 66, q = 11/32$	2112	0.003
$p = 62, Q_s = 63, q = 21/62$	3906	0.003

Torque ripple

FEM simulations were run to compute the torque for different winding layouts. Thereby, an important aspect is to determine the initial position of the rotor in relation to the applied currents. For a SMPM motor, the maximum torque is achieved when the angle β between the current vector and the PM flux vector is 90 electrical degrees. Choosing the current in phase A equal to zero at the initial rotor position, means that the airgap flux density should be at its maximum. Thus, the permanent magnet should be aligned to the tooth or the slot that is the axis of symmetry of the phase A coils, as shown in figure 5.8. Assuming that the first concentrated coil of phase A is around tooth number 1, and the teeth are numbered according to figure 5.8, then the tooth that should be aligned to a permanent magnet can be found in table 5.5 for different winding configurations. When the tooth number is not an integer, it means that the magnet faces a slot.

SMPM motors with different pole and slot numbers as those described in table 5.5 were simulated at nominal load. The results show that they have a torque ripple between 2 and 5 % of the rated torque (table 5.6). It can be noticed that a design with a high cogging torque can have a lower torque ripple than a design with a lower cogging torque, as shown in tables 5.4 and 5.6.

Whatever the investigated slot-pole number combination, the high pole-number PM machines with concentrated windings will have a much lower torque ripple than machines with distributed windings $q = 1$ without skewing. These machines can have a torque ripple over 15 % as was shown in chapter 4.

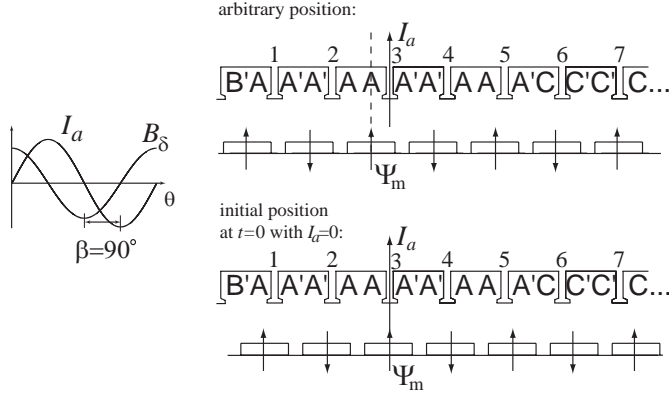


Figure 5.8: Initial position of a SMPM motor. I_a is the current in phase A, B_δ is the airgap flux density.

Table 5.5: Determination of the initial rotor position.

Q_s, p or q	Tooth number
$q = 2/5$	4.5
$q = 3/8$	2
$Q_s = 12 + 6k, k = 0, 1, 2, \dots$	$\frac{Q_s}{12} + \frac{1}{2}$
$p = Q_s \pm 2, p$ even	$\frac{Q_s}{12} + \frac{1}{2}$
$Q_s = 12 + 6k, k = 0, 1, 2, \dots$	$\frac{Q_s}{3} + \frac{1}{2}$
$p = Q_s \pm 2, p$ odd	$\frac{Q_s}{3} + \frac{1}{2}$
$Q_s = 9 + 6k, k = 0, 1, 2, \dots$	$\frac{Q_s}{6} + \frac{1}{2}$
$p = Q_s \pm 1$	$\frac{Q_s}{6} + \frac{1}{2}$

Table 5.6: Torque ripple of different SMPM motors.

p, Q_s, q	Torque ripple [%]
$p = 60, Q_s = 72, q = 2/5$	2.6
$p = 64, Q_s = 72, q = 3/8$	3.4
$p = 64, Q_s = 60, q = 5/14$	3.2
$p = 64, Q_s = 66, q = 11/32$	3.4
$p = 62, Q_s = 63, q = 21/62$	4.4

5.2.4 Magnetic noise

Magnetic noise results from magnetic forces that make the stator vibrate. Radial forces are undesirable attractive forces between the stator and the rotor while tangential forces act on the rotor to produce the torque. The forces that cause magnetic noise are mostly the radial forces [50]. FEM simulations are used to calculate the radial magnetic forces.

The computation of the radial magnetic forces is based on the Maxwell Stress method. For this computation, only the normal component of the flux density is taken into account (5.9).

$$\sigma(\theta, t) = \frac{1}{2\mu_0} B_n(\theta, t)^2 \quad (5.9)$$

where σ is the radial magnetic force density as a function of the angular coordinate θ and the time t , B_n is the normal, i.e. radial component of the airgap flux density.

The tangential component of the airgap flux density is neglected, since the permeability of the iron material is much higher than the one of air. Indeed, the flux lines enter and leave the stator respectively rotor surface almost perpendicularly.

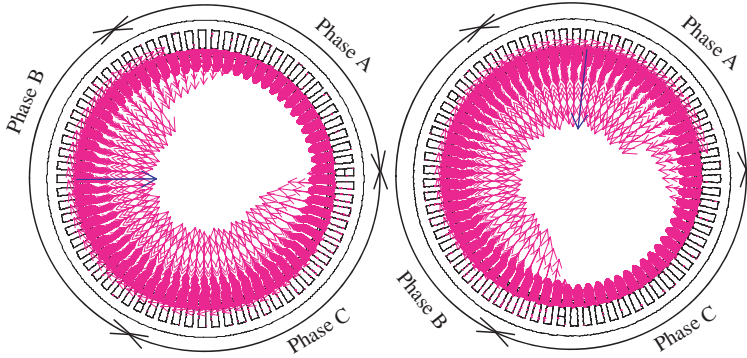


Figure 5.9: Radial magnetic forces on the stator of a SMPM motor with 68 poles and 69 slots, at different times.

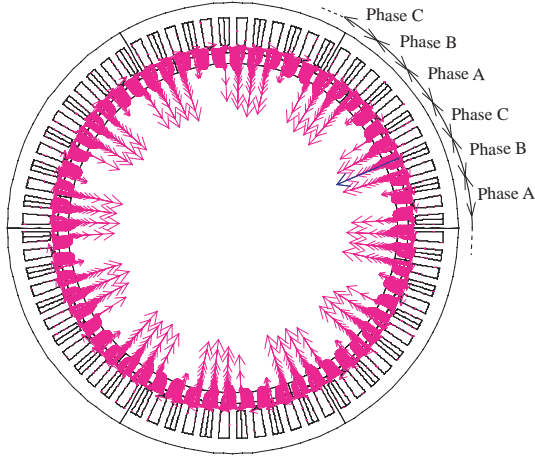


Figure 5.10: Radial magnetic forces on the stator of a SMPM motor with 60 poles and 72 slots.

Figure 5.9 shows the radial magnetic force densities on the stator surface of a SMPM motor with 68 poles and 69 slots at two different instances. It can be seen that the distribution of the magnetic forces on the stator is not symmetrical. The sum of these magnetic forces gives a resulting unidirectional pulling force that rotates with time and generates noise and vibration in the machine. This resulting force is due to the asymmetry in the windings. The pole-slot number combinations giving winding layouts without any symmetry such as combinations with $Q_s = 9 + 6k$ ($k = 0, 1, 2, \dots$) and $p = Q_s \pm 1$ are therefore not recommended. The radial magnetic forces for an SMPM motor design with 60 poles and 72 slots are shown in figure 5.10. As can be seen, its winding layout has a symmetry in one sixth of the machine. Therefore, there is no resulting force for this design, as the radial magnetic forces compensate each other.

5.3 Summary

Concentrated windings with $q = 0.5$ and irregular teeth distribution were investigated for high pole numbers.

The winding factors for different pole-slot number combinations were calculated. Some of the promising winding layouts with high winding factors were described. By choosing one of these layouts, the performances of the machine can be improved considerably. However, it should be taken into account that the concentrated windings cause alternating magnetic fields in the rotor giving rise to rotor losses. Depending on the pole-slot number combinations, the cogging torque can be reduced. The torque ripple at load is harder to predict from the slot-pole number combinations, but it was always very low compared to a distributed winding machine without skewing and $q = 1$. Magnetic noise is also an important issue for some PM machines with concentrated windings. The machine designs with winding layouts without any symmetry have unbalanced radial magnetic forces that make the stator vibrate and produce noise. Slot-pole number combinations with high winding factors and winding layouts with many symmetries give the best performances and avoid high magnetic noise.

Using a carefully chosen slot-pole number combination is more advantageous than using an irregular teeth distribution in terms of torque ripple and winding factor. Therefore, only results of designs with suitable slot-pole number combinations will be investigated in the next chapter.

6 Results and comparison of designs with concentrated windings

In this chapter, the concentrated windings are tested on SMPM, outer-rotor PM and tangentially-magnetized PM motors, which are the most promising motor designs (refer to chapter 4). For this purpose, the design procedure of chapter 3 is adapted to obtain a reliable analytical design:

- The number of slots being almost equal to the number of poles, the teeth of motors with concentrated windings are much larger than those with $q = 1$. As they saturate less easily, no flux leakage factor is used for the calculation of the flux density in the teeth.
- The factor k_{leak} , which is used to take the magnetic leakage into account for the calculation of the airgap flux density, is slightly changed. The FEM simulations give results that are between 4 and 8 % higher than the analytically calculated results with the modified k_{leak} .
- The slot fill factor f_s is set to 0.6 (0.45 for $q = 1$).
- The factor k_{coil} is set to 0.93, as the end-windings are much shorter than for designs with distributed windings. The winding factor now depends on the number of poles and slots (refer to tables 5.4 and 5.5).
- The limit on the magnet weight is reduced to 5 kg.

As shown in the previous chapter, there are many suitable pole-slot number combinations that give high winding factors. The tested combinations are those with many symmetries in the winding layout. They can be found in tables 5.4 and 5.5 and have the following number of slots per pole per phase q and winding factor k_{w1} :

- $q = 2/5$ and $2/7$, $k_{w1} = 0.933$

- $q = 3/8$ and $3/10$, $k_{w1} = 0.9452$
- $q = 5/14$ and $5/16$, $k_{w1} = 0.9514$

To begin with, the obtained results of inner-rotor SMPM, outer-rotor SMPM and tangentially-magnetized PM motor designs are analyzed separately. At first, the motor weight for different winding layouts with both concentrated and distributed windings is calculated as a function of the pole number. Then, the active weight, the permanent magnet weight as well as the torque and torque ripple of four 70-pole motors are calculated and simulated, among which one has distributed windings. Finally, two geometries of 70-pole motors, one with $q = 3/10$ and one with distributed windings ($q = 1$), are illustrated in scale 1:1.

6.1 SMPM motors

Figure 6.1 shows the active weight as a function of the pole number for different values of q . The tendency for SMPM motors with concentrated windings is that the active weight decreases with an increasing pole number. Some points do not follow this tendency due to the fact that the active weight also varies with the number of slots. Thus, the designs with $q = 2/5$ or $2/7$ are slightly heavier than the others, because of the lower winding factor.

Figure 6.1 reveals also that the motors with concentrated windings are about 15 kg lighter than those with distributed windings ($q = 1$). Since there are fewer teeth in designs with concentrated windings, both the slots and teeth can be wider, as figure 6.3 shows. The permanent magnets are allowed to be thicker and the airgap flux density to be higher without saturating the teeth. This allows the motors with concentrated windings to be shorter and therefore lighter. Furthermore, the motors with $q = 1$ were calculated with a higher permanent magnet weight of 5.5 kg, which reduced their total weight further (see figure 4.3).

Table 6.1 presents the results of the load simulations for four motors, of which three have concentrated windings and one has distributed windings. All these designs have equal copper losses (700 W). As can be seen, the torque ripple is reduced from 9.3 % to under 3 % for concentrated windings. The torque curves are displayed in figure 6.1.

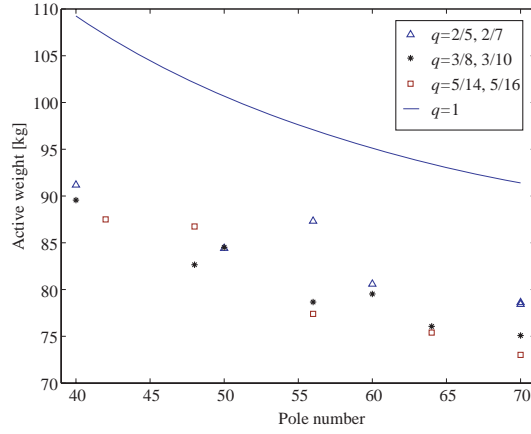


Figure 6.1: Active motor weight as a function of the pole number for SMPM motor designs with concentrated and distributed windings.

Table 6.1: Comparison of SMPM designs (FEM results).

Design q, p, Q_s	Active weight [kg]	PM weight [kg]	Torque [Nm]	Torque ripple [%]
$q = 3/10, p = 70, Q_s = 63$	76.1	5	833.6	2.4
$q = 2/5, p = 70, Q_s = 60$	78.6	5	842.6	2.4
$q = 5/14, p = 70, Q_s = 75$	73.0	5	825.2	2.6
$q = 1, p = 70, Q_s = 210$	91.4	5.5	833.0	9.3

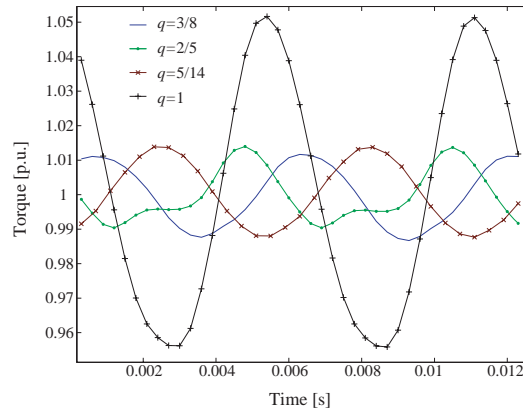


Figure 6.2: Torque of SMPM motors with concentrated and distributed windings at load conditions.

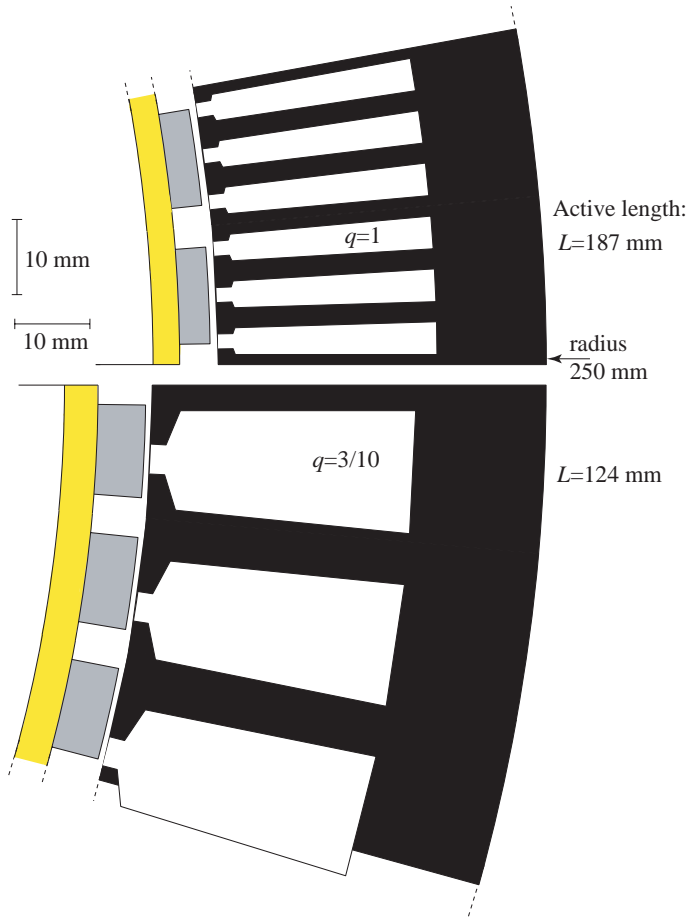


Figure 6.3: Geometries of two 70-pole SMPM motors, one with concentrated windings ($q = 3/10$) and one with distributed windings ($q = 1$) scaled 1:1.

6.2 Outer-rotor SMPM motors

With distributed windings, the outer-rotor SMPM motor designs are lighter than the inner-rotor SMPM motors, as shown in chapter 4. This is also the case with concentrated windings. With concentrated windings, the outer-rotor SMPM motors are approximately 20 kg lighter than with distributed windings, (compare figure 6.1 to figure 6.4). Two geometries are compared in figure 6.6. The drawback of the outer-rotor SMPM motors with $q = 1$ is their high torque ripple (table 6.2). With concentrated windings, it is successfully reduced from 26 % to under 5 %, as depicted in figure 6.5.

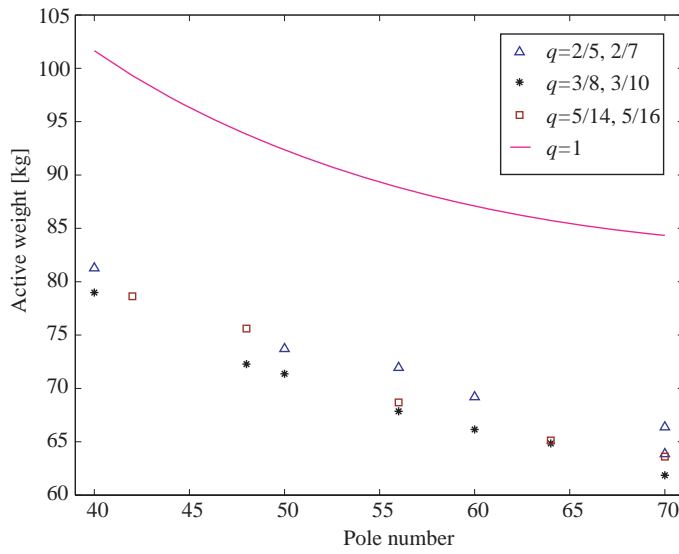
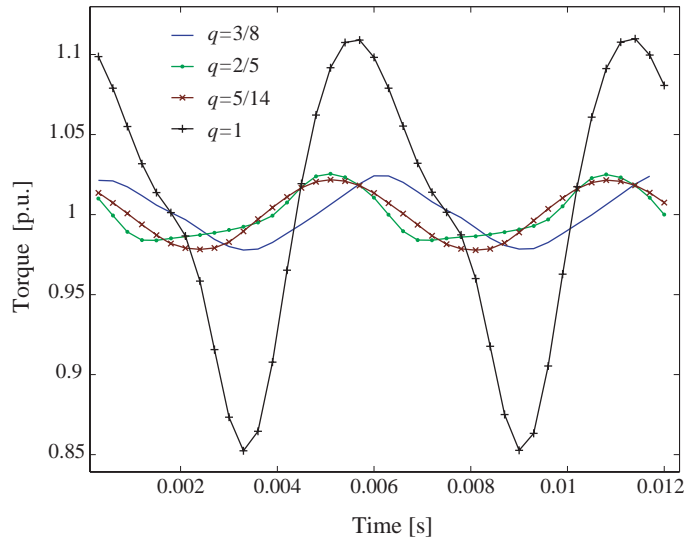


Figure 6.4: Active motor weight as a function of the pole number for outer-rotor SMPM motors with concentrated windings.

Table 6.2: Comparison of outer-rotor SMPM motor designs (FEM results).

Design q, p, Q_s	Active weight [kg]	PM weight [kg]	Torque [Nm]	Torque ripple [%]
$q = 3/10, p = 70, Q_s=63$	61.9	5	887.0	4.6
$q = 2/5, p = 70, Q_s=60$	63.9	5	899.9	4.2
$q = 5/14, p = 70, Q_s=75$	60.5	5	866.2	4.4
$q = 1, p = 70, Q_s=210$	83.0	5.5	839.6	25.7

**Figure 6.5:** Torque of outer-rotor SMPM motors with concentrated and distributed windings at load conditions.

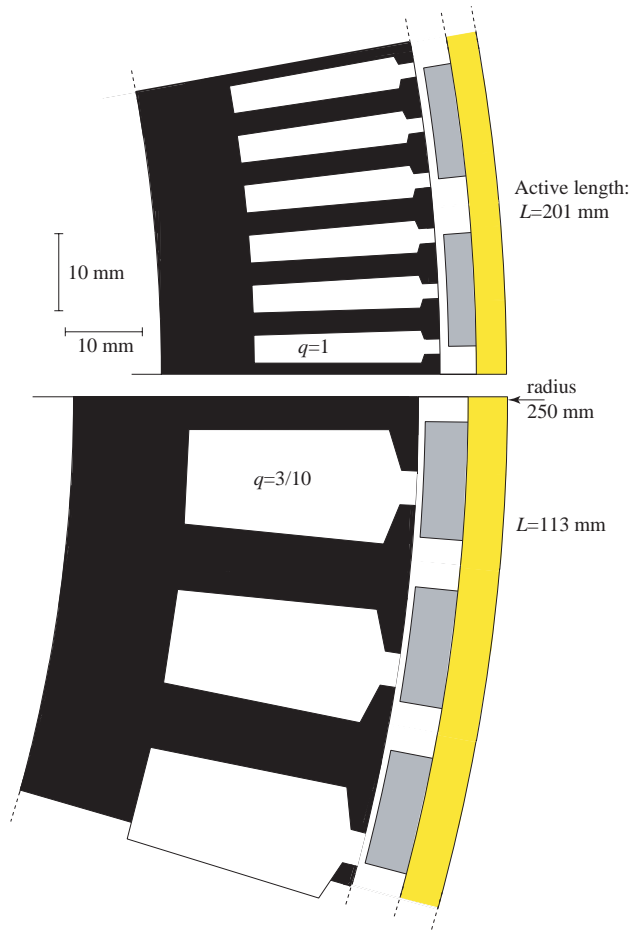


Figure 6.6: Geometries of two 70-pole outer-rotor SMPM motors, one with concentrated winding ($q = 3/10$) and one with distributed windings ($q = 1$) scaled 1:1.

6.3 Tangentially-magnetized PM motors

As for the two previous configurations, a figure is used to present the active weight of different motor designs with concentrated and distributed windings (figure 6.7). However, for the tangentially-magnetized PM motor designs, the difference is that the found optimized designs with concentrated windings have lower permanent magnet weights than the allowed 5 kg. Their permanent magnet weight is only between 3.5 and 4.5 kg. This is due to the constraint on the amplitude of the fundamental airgap flux density that is not allowed to exceed 1.1 T. Due to the flux concentration, the airgap flux density reaches easily 1.1 T with less than 5 kg permanent magnets. Furthermore, the lower bound of the constraint on the machine length, which is 100 mm, is reached for some designs. The external diameter is then reduced and becomes less than 500 mm. This can be observed in table 6.3 that presents different features of 70-poles tangentially-magnetized PM motors. Also in this case, the torque ripple is considerably reduced with concentrated windings, as shown in table 6.3 and figure 6.8.

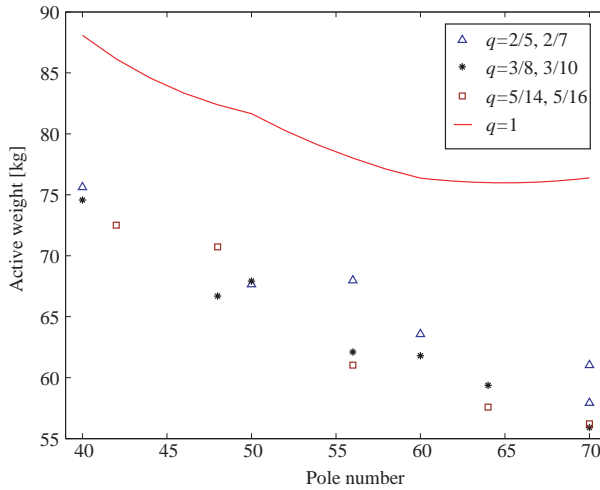
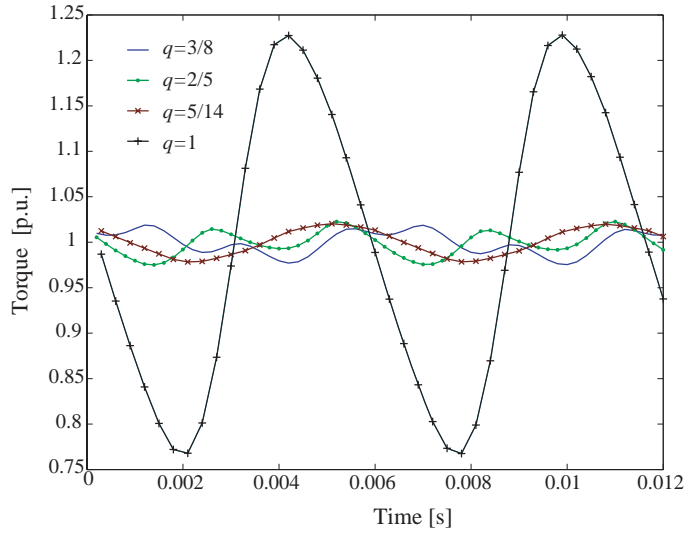


Figure 6.7: Active motor weight as a function of the pole number for tangentially-magnetized PM motors with concentrated windings.

Table 6.3: Comparison of 70-pole tangentially-magnetized PM motor designs (FEM results).

q	Active weight [kg]	PM weight [kg]	Torque [N.m]	Torque ripple [%]	Active length [mm]	Outer diameter [mm]
$q = 3/10$	55.9	3.4	876.3	4.2	101	500
$q = 2/5$	57.9	3.3	881.8	4.8	100	498
$q = 5/14$	56.2	4.1	868.6	4.2	119	500
$q = 1$	76.4	5.5	863.1	41.7	163	500

**Figure 6.8:** Torque with concentrated and distributed windings of tangentially-magnetized PM motors at load condition.

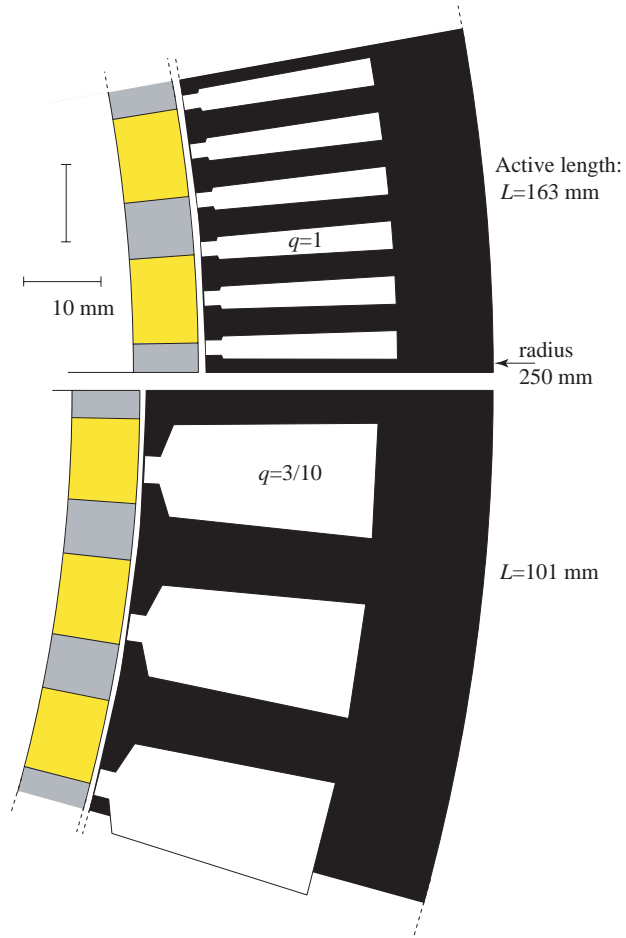


Figure 6.9: Geometries of two 70-pole tangentially-magnetized PM motors, one with concentrated windings ($q = 3/10$) and one with distributed windings ($q = 1$) scaled 1:1.

6.4 Choice of a design

A closer look is given on the 70-pole, 63-slot tangentially-magnetized PM motor. This design is chosen because the tangentially-magnetized PM motors are lighter than the other configurations. The weight of the permanent magnets is as well lower and their torque ripple, which is around 4 % of the nominal torque, is satisfactory. Furthermore, the choice of $q = 3/10$ is based on the number of symmetries in the winding layout that is 7 when $p = 70$, $q = 3/10$ against 5 for the two other considered windings ($q = 2/5$ and $q = 5/14$).

The design fulfills the requirements with a good margin: the active weight of 56 kg is far under 150 kg. With a 700 W value of copper losses, 490 W of other losses are allowed in order to keep the efficiency higher than the 73 % of the induction motor and its gearbox. The iron losses reach only 85 W according to the FEM calculations (appendix B), 78 W from the stator and 7 W from the laminated rotor . Even the price of the motor looks reasonable. If one kilogram of permanent magnet material costs 1000 SEK, then the permanent magnets will cost 3400 SEK that is less than what the gearbox costs.

6.5 Conclusions

Motors with distributed windings and $q = 1$ are unsatisfactory because of the high torque ripple. This drawback is reduced by using concentrated windings. For all motor configurations, the torque ripple is decreased under 5 %. The inner-rotor SMPM motor designs have the smallest torque ripple.

Furthermore, concentrated windings allow a higher airgap flux density without the teeth getting saturated, as the tooth width is larger compared to other motor designs. Thus, motor designs with concentrated windings are lighter and contain less permanent magnet material.

The lightest motors are the tangentially-magnetized PM motors. They allow designs with much lower permanent magnet weight than other motor configurations without increasing the total active weight.

However, it should not be forgotten that concentrated windings induce losses in the rotor. These losses have not been studied yet and further work is needed. A thermal study should be made to show that the permanent magnets are not subject to demagnetization due to high temperature induced by eddy currents.

7 Design and results of axial-flux PM motors

This chapter deals with the low-speed AFPM motors. The features used for the design are first presented. The design procedure is then described and followed by the results that are obtained analytically and from 3D-FEM simulations.

7.1 Main features of the Torus AFPM motor

In this section, the geometry of the Torus AFPM motor is described by defining its geometrical parameters. Then the flux densities are calculated. Finally the windings are described, including analytical calculations of the inductances, resistances and number of conductors. The equations given in this section are based on [22] and [51].

7.1.1 Dimensions of the motor

The geometry of the axial-flux PM motor is described in figure 7.1. It is a Torus AFPM machine without slots, as seen in section 2.2. The following dimensions are used during the design procedure:

Ratio of inner to outer stator radius:

$$\lambda = \frac{R_i}{R_o} \quad (7.1)$$

Axial length of the stator:

$$L_s = 2l_w + l_{sc} \quad (7.2)$$

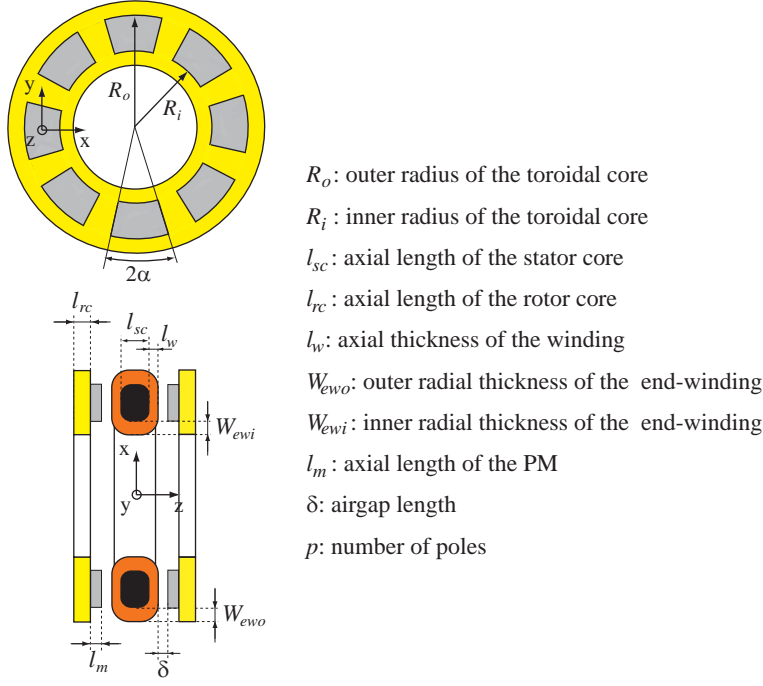


Figure 7.1: Definition of the geometrical parameters for the Torus AFPM machines.

Axial length of a rotor disc:

$$L_r = l_m + l_{rc} \quad (7.3)$$

Axial length of the machine:

$$L = L_s + 2L_r + 2\delta \quad (7.4)$$

Average diameter of the airgap:

$$D_g = R_o + R_i \quad (7.5)$$

Average pole pitch:

$$\tau = \pi D_g / p \quad (7.6)$$

Effective length of the stator core:

$$W_w = R_o - R_i \quad (7.7)$$

Average length of the stator end connection:

$$W_{ew} = \frac{1}{2}(W_{ewo} + W_{ewi}) \quad (7.8)$$

7.1.2 Flux densities

Flux density in the airgap

The particularity of the Torus AFPM motor without teeth is its large effective airgap, which includes the airgap δ and the axial thickness of the winding l_w . Owing to this large effective airgap, the airgap flux density created by the permanent magnets usually does not exceed 0.65 T [22].

The maximum of the airgap flux density B_m is calculated as:

$$B_m = \frac{B_r l_m}{l_m + \delta + l_w} \quad (7.9)$$

The amplitude of the fundamental airgap flux density B_δ is set equal to the maximum airgap flux density B_m :

$$B_\delta = B_m \quad (7.10)$$

This assumption is based on 3D-FEM simulations. The obtained results are gathered in figure 7.3 and table 7.1. Two components (B_y and B_z) of the flux density in the middle of the airgap length were investigated for three different geometries with various permanent magnet widths. B_z is the axial component of the airgap flux density whereas B_y is the ortho-radial component (the directions of the x-, y- and z-axis are defined in figure 7.2). Appendix B explains how the 3D-FEM simulations were conducted.

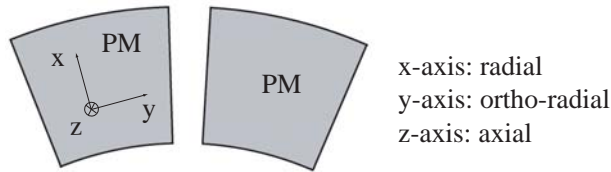


Figure 7.2: Definition of the x-, y- and z-axis.

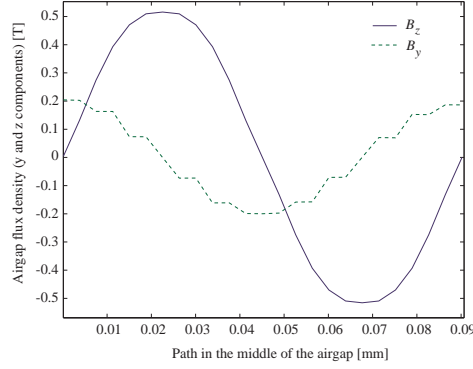


Figure 7.3: 3D-FEM simulated airgap flux densities, B_y , B_z components.

As shown in figure 7.3, the axial component of the airgap flux density B_z , which interacts with the current and generates the torque, is very smooth, quite close to sinusoidal. This justifies the rough assumption made in equation (7.10).

The ortho-radial component of the airgap flux density B_y is the flux leaking between two adjacent permanent magnets. Table 7.1 shows that the three investigated designs have almost the same axial component of the 3D-FEM simulated fundamental airgap flux density $B_{\delta z, FEM}$, whereas the permanent magnet width is very different. Indeed, when the PM width l_m is high, a considerable part of the flux density from the permanent magnets is wasted in the leakage flux between adjacent permanent magnets contained in B_y . Therefore, the permanent magnet thickness should not be too high in order to utilize the permanent magnets as efficiently as possible. The upper limit was chosen equal to 10 mm. As can be seen in table 7.1, the FEM simulated value of the fundamental airgap flux density $B_{\delta z1, FEM}$ is closed to the analytically calculated value $B_{\delta, an}$ when $l_m = 10 \text{ mm}$.

Table 7.1: Airgap flux densities of different 30-pole AFPM machine designs.

l_m [mm]	δ [mm]	l_w [mm]	$B_{\delta, an}$ [T]	$B_{\delta z1, FEM}$ [T]	$B_{\delta y1, FEM}$ [T]
20	1	10.7	0.680	0.533	0.202
13	1	9.1	0.608	0.538	0.181
10	1	8.9	0.544	0.526	0.120

Flux density in the stator and rotor cores

The flux densities in the stator and rotor cores are calculated with equations (7.11) and (7.12) respectively. As for the radial-flux PM machines, these flux densities are subject to some constraints to avoid saturation.

$$B_{sc} = \frac{\pi B_\delta D_o (1 + \lambda)}{2p l_{sc}} \quad (7.11)$$

$$B_{rc} = \frac{\pi B_\delta D_o (1 + \lambda)}{4p l_{rc}} \quad (7.12)$$

7.1.3 Windings

The windings are wound around the torus. As depicted in figure 7.1, the thickness of the winding and end-windings is defined with three parameters: l_w for the "working" part of the winding, W_{ewo} and W_{ewi} for the end-windings which are not contributing in the generation of the torque. In order to simplify the design, these three parameters are set equal to each other:

$$l_w = W_{ewo} = W_{ewi} \quad (7.13)$$

This assumption is possible because the outer and inner machine diameters are large.

The values of the reactances, resistance and number of turns per phase of the windings are needed for the design and thus their determination is described below.

Winding reactances

The motor is not salient, therefore the d- and q-axis reactances are equal. X_{md} is the magnetizing reactance:

$$X_{md} = 4m_1 \mu_0 f \frac{(N_s k_{w1})^2}{\pi p} \cdot \frac{\tau W_w}{\delta_{eq}} \quad (7.14)$$

where m_1 is the number of phases, N_s the number of turns per phase and δ_{eq} the equivalent airgap length given as:

$$\delta_{eq} = 2\delta + 2l_m/\mu_r \quad (7.15)$$

X_l is the leakage reactance:

$$X_l = 4\pi\mu_0 f \frac{N_s^2 W_w}{p q} \left(\frac{W_{ew}}{W_w} \lambda_{le} + \lambda_{ld} \right) \quad (7.16)$$

where λ_{le} is the end-connection leakage permeance (q is the equivalent to the number of slots per pole per phase):

$$\lambda_{le} = 0.3 q \quad (7.17)$$

and λ_{ld} the differential leakage permeance:

$$\lambda_{ld} = \frac{m_l q \tau k_{w1}^2}{\pi^2 \delta k_C k_{sat}} \tau_{dl} \quad (7.18)$$

τ_{dl} is the differential leakage factor:

$$\tau_{dl} = \left[\frac{\pi^2 (10q^2 + 2)}{27} \sin \frac{30^\circ}{q} \right] - 1 \quad (7.19)$$

The d- axis synchronous reactance is then given by:

$$X_d = X_l + X_{md} \quad (7.20)$$

Winding resistance

The stator winding resistance per phase is given by:

$$R = \frac{N_s l_{1av} \rho_{cu}}{a s_a} \quad (7.21)$$

where l_{1av} is the average length of a stator turn (7.22), a is the number of parallel paths or conductors and s_a is the cross-section of a conductor (7.23).

$$l_{1av} = 2W_w + W_{ewo} + W_{ewi} \quad (7.22)$$

$$s_a = \frac{\pi d_w^2}{4} \quad (7.23)$$

The wire diameter d_w , is given by:

$$d_w = \sqrt{\frac{4 l_w D_i f_s}{a m_1 N_s}} \quad (7.24)$$

Number of turns per phase

The number of turns per phase N_s of the Torus AFPM motor is calculated with the same method as the SMPM motor (section 3.3.7, equation (3.50)). The RMS value of the EMF is calculated as:

$$E = 2\pi f N_s k_{w1} \frac{\pi}{8p} B_\delta D_o^2 (1 - \lambda^2) \quad (7.25)$$

7.2 Design

7.2.1 The design procedure

The design of the Torus AFPM machines follows the same procedure as the radial-flux PM motors designs. The chart of figure 7.4 reminds of this design procedure.

The design starts by choosing a set of values for the eight variables to be optimized. These variables are p , R_o , R_i , l_m , α , l_{rc} , l_{sc} , δ and l_w . They describe the entire motor geometry and allow to calculate the different features of the motor.

The procedure then continues with the calculation of the flux densities in the airgap and the rotor and stator cores. The ampere-turns are then computed from the torque equation:

$$N_s I = \frac{4T}{m_1 k_{w1} B_\delta D_o^2 (1 - \lambda^2)} \quad (7.26)$$

Afterwards, the number of turns per phase can be deduced and the copper losses can be calculated. Finally, the objective function which is the active weight, is expressed as a function of the design variables. After some iterations of the optimization procedure, a minimum for the objective function is found.

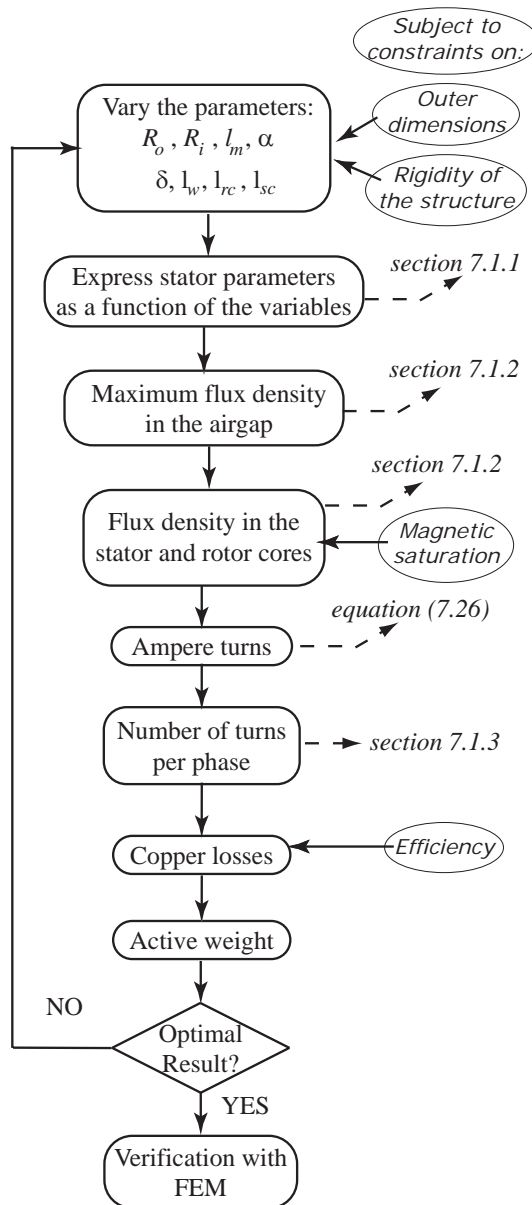


Figure 7.4: Followed procedure to optimize designs of low-speed Torus AFPM motors.

7.2.2 The design constraints

Geometry

The outer dimensions and the maximum motor weight are subject to the same limits as the RFPM machines.

The rigidity of the structure is guaranteed by setting lower limits on the geometrical parameters. Furthermore, the permanent magnet width should not exceed 10 mm to limit the leakage between two adjacent permanent magnets as seen in section 7.1.2. The effective airgap length is also limited by having an upper boundary of 10 mm on the winding thickness l_w .

The choice of the upper boundary for l_w is confirmed by looking at the magnetization curve of the PM material and the load lines (figure 7.5). Indeed, the PM material is best utilized when operating at the point where its energy product is maximum, thereby achieving minimum volume and cost of the PM material.

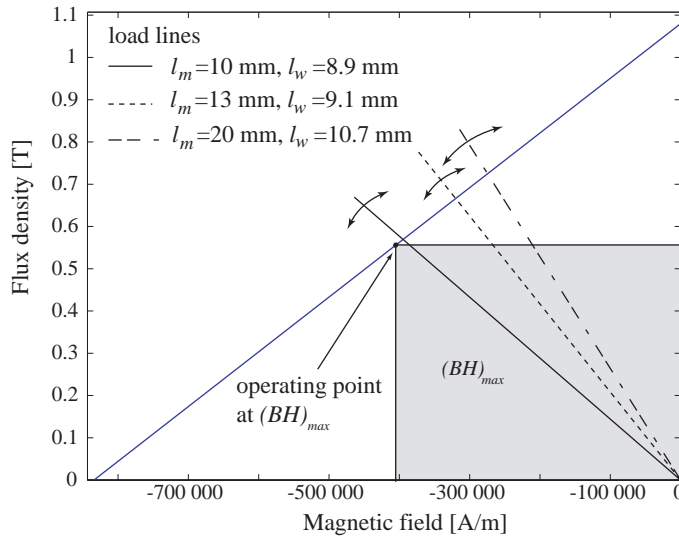


Figure 7.5: Magnetization curve of the PM material, its maximum energy product and the load lines of three different designs.

The load lines of three 30-pole Torus AFPM designs with different l_m and l_w (as given in table 7.1) are calculated from 3D-FEM simulations. The flux density and magnetic field are varying depending on the point in the permanent magnet where they are calculated. Therefore different points were checked, which is illustrated in figure 7.5 by the arrows across the load lines. The figure also shows the maximum energy product $(BH)_{max}$. For NdFeB permanent magnets in Torus AFPM machines, it corresponds to the case where $l_w \simeq l_m$. Therefore, the load line corresponding to the lowest permanent magnet width comes closest to the point where the energy product of the permanent magnets is maximum.

Magnetic saturation

Magnetic saturation in the rotor and stator cores is avoided by limiting the flux densities B_{sc} and B_{rc} to a maximum of 1.6 T and 1.4 T respectively. The winding temperature is assumed to be 80 °C.

Efficiency and cost

The copper losses are limited to 700 W to start with. The maximum permanent magnet weight is not subject to any constraints.

7.3 Results

7.3.1 Torus AFPM machine

At first, the design procedure for the Torus AFPM machine was run applying the constraints presented above. No solutions that fulfill these constraints were found. The number of poles was varied from $p = 10$ to 70. It was noticed that the optimization algorithm was not as efficient as for design of RFPM machines: The optimized solutions were depending a lot on the initial values, probably due to many local minima in the objective function. In order to find some solutions, the constraint on the outer diameter was

adjusted. Optimized designs are then found when the maximum allowed outer diameter is increased to 550 mm. The permanent magnet weight is around 122 kg, which is very high compared to the radial-flux PM machines. Another concession can be made by increasing the allowed copper losses while the maximum outer diameter is set back to 500 mm. Solutions fulfilling the requirements on the constraints are found for maximum copper losses of 1030 W. These designs have a significantly decreased efficiency. The permanent magnet weight is around 7 kg.

It can be concluded from these design attempts, that the torus AFPM machine without slots, with two rotors and one stator is not appropriate for the application. A way to achieve the nominal torque without exceeding the allowed outer diameter may be to have a multi-disk Torus AFPM machine. An investigation on such machines is made in the next section.

7.3.2 Multi-disk Torus AFPM machine

The multi-disk Torus AFPM machine is composed of at least two Torus AFPM machines as those described previously. The studied example consists thus of two stators and four rotor disks as shown in figure 7.6.

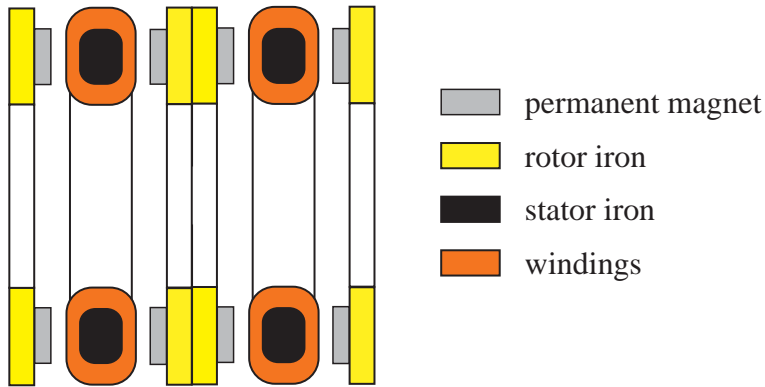


Figure 7.6: Multi-disk torus AFPM machine.

The multi-disk Torus AFPM machine is designed using the same procedure as for the Torus AFPM machine (refer to section 7.2.1): One of these two Torus AFPM machines is optimized for half the nominal torque. The total active weight of the machine is twice the active weight of the optimized Torus AFPM machine.

Figure 7.7 shows the active weight of different multi-disk AFPM motors as a function of the pole number. All the calculated designs have an outer diameter equal to 500 mm, 700 W copper losses and permanent magnets weight is 6 kg. As can be seen, the multi-disk AFPM machines are very light, under 40 kg for most of them.

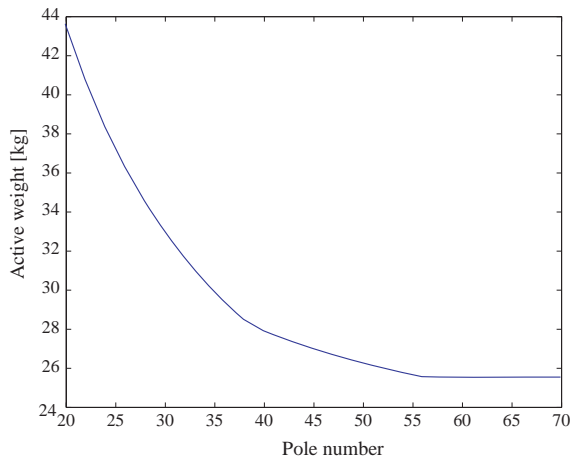


Figure 7.7: Active weight as a function of the pole number of multi-disk Torus AFPM machines.

For RFPM machines with constant copper losses, a lower permanent magnet weight, i.e. a lower airgap flux density from the permanent magnets, is compensated by a higher current loading. Therefore the conductors have a bigger diameter which causes the slots to be larger. For the AFPM machines, another factor has to be taken into account if the permanent magnet weight should be decreased. Indeed, a higher current loading is obtained with a higher number of turns or a larger conductor diameter. This implies an increase of the effective airgap, which leads to an even lower airgap flux density. The nominal torque would then not be achieved. Therefore, it was impossible to decrease the value of the permanent magnet weight for constant copper losses.

Figure 7.8 and 7.9 show the geometry of a calculated 36-pole multi-disk Torus AFPM motor design. The permanent magnet weight is 6 kg, the active weight is 30 kg and the axial length is 123 mm.

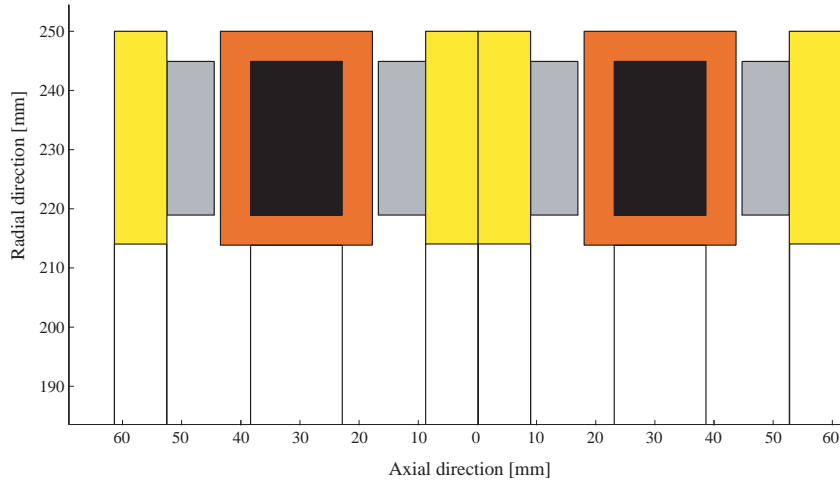


Figure 7.8: Part of the geometry of a 36-pole multi-disk Torus AFPM motor.

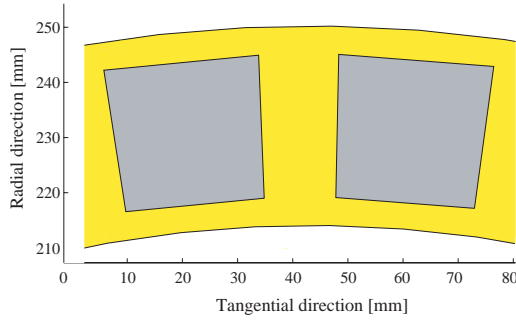


Figure 7.9: Two permanent magnets of a 36-pole multi-disk Torus AFPM motor.

7.3.3 Comparison with the investigated RFPM motors

The calculated multi-disk Torus AFPM motor designs are much lighter than the RFPM motors. The difference in the active weight is approximately 20 kg. Another advantage of the multi-disk AFPM machine is that it has no cogging torque due to the absence of teeth (but no attempt has been made to simulate the torque ripple).

However, some RFPM machines with concentrated windings have much lower permanent magnet weights than the multi-disk Torus AFPM machines: the difference in PM material between radial- and axial-flux machines is up to 2.5 kg. Table 7.2 recapitulates the obtained designs for the different investigated machine configurations. In this table however, it does not appear that the main drawback of the multi-disk Torus AFPM machine lies in its construction. The assembly of the four disks and two stators is tricky due to the attraction forces between the rotor discs [52].

Table 7.2: Comparison of the different investigated PM machines: Some calculated and FEM-simulated results.

(CW stands for concentrated windings and DW for distributed windings)					
Motor configuration	Winding type	Pole/Slot numbers	Active weight [kg]	PM weight [kg]	Torque ripple [%]
Inner-rotor	$q = 1$	70/210	91.4	5.5	9.3
SMPM	CW	70/63	76.1	5	2.4
Outer-rotor	$q = 1$	70/210	83	5.5	25.7
SMPM	CW	70/63	61.9	5	4.6
Inset PM	$q = 1$	70/210	90.7	5.5	22
V-shaped PM	$q = 2$	30/180	141.5	5.5	35
Tangentially-magnetized PM	$q = 1$	70/210	76.4	5.5	41.7
	CW	70/63	55.9	3.4	4.2
Torus AFPM	DW		no solution		
Multi-disk AFPM	DW	36/108*	29.4	6	**

* number of coils (corresponds to $q = 1$).

** not calculated because it requires a transient 3D-FEM simulation.

7.4 Summary

The Torus AFPM machines were investigated for the low-speed direct-drive application. At first, no designs that satisfy all the constraints were found. The main reason is the restriction on the outer diameter.

The solution that was investigated to achieve the nominal torque with a limited outer diameter was the multi-disk Torus AFPM machine. The calculated designs have very attractive active weight compared to the RFPM machine designs, but in contrast the permanent magnet weight is higher and difficult to minimize. Furthermore, the assembly of the multi-disk Torus AFPM machine is very delicate.

Another solution would be to consider a torus AFPM motor with teeth in the stator. The advantage is a higher achievable airgap flux density, since the effective airgap is much smaller with the teeth. However, this solution is not investigated in this thesis.

8 Conclusions and future work

8.1 Conclusions

Different motor configurations have been investigated in an attempt to replace an induction motor and its gearbox with a competing direct-driven PM machine. A design procedure based on an optimization program has been developed, taking the particularities of each configuration into account.

At first, designs with distributed windings and one slot per pole per phase are calculated and simulated with FEM. The designs of the inner- and outer-rotor SMPM motors and of the tangentially-magnetized PM motors are the most promising, since they are satisfying the requirements on the size, weight and efficiency. However, the torque ripple of these machines is very high. The tangentially-magnetized PM motors are found to be the lightest, while the V-shaped PM motor designs could not compete with the other motor configurations.

In order to improve these designs, concentrated windings for high pole number PM machines have been investigated. Winding layouts offering high winding factors and limiting the rotor losses as well as the noise and vibrations of the machine are identified and sorted out for further investigations with FEM simulations. The designs with concentrated windings are much lighter than the designs with distributed windings. The torque ripple is also much lower, under 5%. One of the best designs is a tangentially-magnetized PM motor, with 70 poles, 63 slots and concentrated winding. This motor has an active weight under 60 kg with only 3.4 kg of permanent magnet material.

At last, the Torus AFPM machine configuration was tested for the application. No designs fulfilling the requirements have been found. Therefore, multi-disk Torus AFPM machine designs were investigated. The design procedure results in very light machines regarding the active weight, around 30 kg. However, the permanent magnet weight is slightly higher than for the calculated RFPM machines. Additionally, the construction of this kind of machine is problematic.

Several designs that fulfill the requirements have been both calculated and simulated with FEM. Some of these designs are very promising, since the weight of the permanent magnets is reasonable for a sufficient efficiency. Furthermore, the active motor weight is far below the limit, leaving a comfortable margin for the weight of the mechanical parts.

8.2 Suggestions for future work

Different theoretical designs have been found to be very promising for the application. Thus, the future work could concentrate further on one particular design for the purpose of building a prototype. The iron losses, rotor losses and eddy-currents in the permanent magnets should be investigated further. The constraints applied during the design procedure should be improved, notably the constraints on the rigidity of the structure. They have to be adapted to the application. If a prototype is built, a lot of work would be required for designing the mechanical elements, testing the prototype and verifying if the machine fulfills the expectations.

Besides, the AFPM machines require more work. The optimization algorithm should be improved, as it was very dependent on the initial conditions. Other AFPM machine configurations could fulfill the requirements. A first one is the Torus AFPM machines with a slotted stator. A second one is an AFPM machine with concentrated windings and stator cores made of compact iron powder composites. These configurations could be an alternative to the investigated multi-disk Torus AFPM machine.

Bibliography

- [1] Grauers A., *Design of direct-driven permanent-magnet generators for wind turbines*, Doctoral thesis, Chalmers University of Technology, Göteborg, Sweden, 1996.
- [2] Carlson O., Grauers A., Williamson A., Engström S., Spooner E., *Design and test of a 40 kw directly driven permanent-magnet generator with a frequency converter*, European Wind Energy Conference and Exhibition, EWEC'99, Nice, France, 1999.
- [3] Chalmers B., Wu W., Spooner E., *An axial-flux permanent-magnet generator for a gearless wind energy system*, IEEE Transactions on Energy Conversion, Vol. 14, No. 2, pp. 251-257, 1999.
- [4] Hartkopf T., Hofmann M., Jöckel S., *Direct-drive generators for megawatt wind turbine*, European Union Wind Energy Conference, EWEC'97, Dublin, 1997.
- [5] Jöckel S., *Gearless wind energy converters with permanent magnet generators. an option for the future?*, European Union Wind Energy Conference, EWEC'96, Göteborg, Sweden, 1996.
- [6] Chen J., Nayar C., Xu L., *Design and finite-element analysis of an outer-rotor permanent-magnet generator for directly coupled wind turbines*, IEEE Transactions on Magnetics, Vol. 36, No. 5, pp. 3802-3809, 2000.
- [7] Hakala H., *Integration of motor and hoisting machine changes the elevator business*, ICEM 2000, Vol. 3, pp. 1242-1245, 2000.
- [8] Caricchi F., Crescimbeni F., Honorati O., *Modular axial-flux permanent-magnet motor for ship propulsion drives*, IEEE Transactions on Energy Conversion, Vol. 14, No. 3, pp. 673-679, 1999.

- [9] Parker D., Hodge C., *The electric warship*, Power Engineering Journal, Vol. 12, Issue 1, pp. 5-13, 1998.
- [10] Ficheux R., Caricchi F., Crescimbeni F., Onorato H., *Axial-flux permanent-magnet motor for direct-drive elevator systems without machine room*, IEEE Transactions on Industry Applications, Vol. 37, No. 6, pp 1693-1701, 2001.
- [11] ITT Flygt, *Product catalogue, slow speed mixer*, www.flygt.com.
- [12] Sitapati K., Krishnan R., *Performance comparisons of radial and axial field, permanent-magnet, brushless machines*, IEEE Transactions on Industry Applications, Vol. 37, No. 5, 2001.
- [13] Haring T., Forsman K., Huhtanen T., Zawadzki M., *Direct drive - opening a new era in many applications*, Pulp and Paper Industry Technical Conference, pp. 171-179, 2003.
- [14] Rosu M., Nahkuri V., Arkkio A., Jokinen T., Mantere J., Westerlund J., *Permanent magnet synchronous motor for ship propulsion drive*, Symposium on Power Electronics Electrical Drives Advanced Machines Power Quality (SPEEDAM'98), Sorrento, Italy, pp. C3-7:C3-12, 1998.
- [15] Lampola P., Perho J., *Electromagnetic analysis of a low-speed permanent-magnet wind generator*, Opportunities and Advances in International Power Generation, IEE, pp. 55-58, 1996.
- [16] Spooner E., Williamson A., *Direct coupled, permanent magnet generators for wind turbine applications*, IEE Electric Power Applications, Vol. 143, No. 1, pp. 1-8, 1996.
- [17] Chen J., Nayar C., *A direct-coupled, wind-driven permanent magnet generator*, Energy Management and Power Delivery, EMPD'98, Vol. 2, pp. 542-547, 1998.
- [18] Wu W., Ramsden V., Crawford T., Hill G., *A low-speed, high-torque, direct-drive permanent magnet generator for wind turbines*, IEEE Industry Applications Conference, Vol. 1, pp. 147-154, 2000.
- [19] Heikkilä T., *Permanent magnet synchronous motor for industrial inverter applications - analysis and design*, Doctoral thesis, Lappeenranta University of Technology, 2002.

-
- [20] Caricchi F., Crescimbinì F., *Axial-flux machines: design and applications*, Overheads of the Seminar at KTH, 2000.
 - [21] Cirani M., *Analysis of an innovative design of an axial flux torus-machine*, Licentiate Thesis, ISSN 1650-674X, 2002.
 - [22] Gieras J., Wing M., *Permanent magnet motor technology*, New York, Marcel Dekker, ISBN 0-8247-0739-7, 2002.
 - [23] Muljadi E., Butterfield C., Wan Y., *Axial flux, modular, permanent-magnet generator with a toroidal winding for wind turbine applications*, IEEE Transactions on Industry Applications, Vol. 35, No. 4, pp. 831-836, 1999.
 - [24] Söderlund L., Eriksson J., Salonen J., H.Vihriälä, Perälä R., *A permanent-magnet generator for wind power applications*, IEEE Transactions on Magnetics, Vol. 32, No. 4, pp. 2389-2392, 1996.
 - [25] Crescimbinì F., Carricchi F., Solero L., Chalmers B., Spooner E., Wu W., *Electrical equipment for a combined wind/pv isolated generating system*, Opportunities and Advances in International Power Generation IEE, Conference publication No. 419, pp. 59-64, 1996.
 - [26] Mitcham A., *Transverse flux motors for electric propulsion of ships*, IEE Colloquium on New Topologies for Permanent Magnet Machines, Digest No. 1997/090, pp. 3/1-3/6, 1997.
 - [27] Henneberger G., Bork M., *Development of a new transverse flux motor*, IEE Colloquium on New Topologies for Permanent Magnet Machines, Digest No. 1997/090, pp. 1/1-1/6, 1997.
 - [28] Lefevre L., Soulard J., Nee H.P., *Design procedure for line-start permanent magnet motors reversible modification of the no-load voltage of a line-start permanent magnet synchronous motor*, IEEE Nordic Workshop on Power and Industrial Electronics, NORpie 2000, Aalborg, Denmark, 2000.
 - [29] Chen Z., Spooner E., *A modular permanent-magnet generator for variable speed wind turbine*, Electrical Machines and Drives IEE, Conference publication No. 412, pp. 453-457, 1995.

- [30] Spooner E., Williamson A., *Modular, permanent-magnet wind-turbine generators*, Industry Applications Conference, IAS'96., Vol. 1, pp. 497-502, 1996.
- [31] Williamson A., Spooner E., Thompson L., *Large modular pm generators*, IEE Colloquium on New Topologies for Permanent Magnet Machines, Digest No. 1997/090, pp. 4/1-4/6, 1997.
- [32] Epskamp T., Hagenkort B., Hartkopf T., Jöckel S., *No gearing, no converter - assessing the idea of highly reliable permanent-magnet induction generators*, European Union Wind Energy Conference, EWEC'99, Nice, France, 1999.
- [33] Sadarangani C., *Design and analysis of induction and permanent magnet motors*, Book, Royal Institute of Technology, Stockholm, ISBN 91-7170-627-5, 2000.
- [34] Zhu Z., Howe D., Xia Z., *Prediction of open-circuit airgap field distribution in brushless machines having an inset permanent magnet rotor topology*, IEEE Transactions on Magnetics, Vol. 30, No. 1, pp 98-107, 1994.
- [35] Thelin P., Nee H.P., *Analytical calculation of the airgap flux density of pm synchronous motors with buried magnets including axial leakage, tooth and yoke saturations*, International Conference on Power Electronics and Variable Speed Drives, London, 2000.
- [36] Meier S., *Theoretical design of surface-mounted permanent magnet motors with field-weakening capability*, Master thesis, Royal Institute of Technology, Departement of Electrical Machines and Power Electronics, Stockholm, 2002.
- [37] Magnussen F., C. Sadarangani T.
- [38] Mohan N., Undeland T., Robbins W., *Power electronics, converters, applications, and design*, Book, ISBN 0-471-58408-8, 1995.
- [39] *Matlab help on optimization toolbox*.
- [40] Say M., *The performance and design of alternating current machines*, Book, Pitman, ISBN 999-184258-6, 1948.

-
- [41] Jack A., Mecrow C., Dickinson P., Stephenson D., Burdess J., Fawcett N., Evans J., *Permanent-magnet machines with powdered iron cores and prepressed windings*, IEEE Transactions on Industry Applications, Vol. 36, Issue 4, pp. 1077-1084, 2000.
 - [42] Patent No. 92958, *Mehrphasenmaschine mit ungleicher ankerspulen und polzahl*, Deutsches Reichspatent, 1895.
 - [43] Cros J., Viarouge P., *Synthesis of high performance pm motors with concentrated windings*, IEEE Transactions on Energy Conversion, Vol. 17 Issue 2, pp. 248-253, 2002.
 - [44] Koch T., Binder A., *Permanent magnet machines with fractional slot winding for electric traction*, International Conference on Electrical Machines, ICEM 2002, Brugge, Belgium, 2002.
 - [45] Magnussen F., Thelon P., Sadarangani C., *Performance evaluation of permanent magnet synchronous machines with concentrated and distributed windings including the effect of field-weakening*, IEE International conference on Power Electronics and Electrical Machines (PEMD), Edinburgh, United Kingdom, 2004.
 - [46] Ishak D., Zhu Z., Howe D., *Comparative study of permanent magnet brushless motors with all teeth and alternative teeth windings*, IEE International conference on Power Electronics and Electrical Machines (PEMD), Edinburgh, United Kingdom, 2004.
 - [47] Jack A., Mecrow C., Evans S., *Low cost smc brushless dc motors for high volume applications in the automotive sector*, IEE International conference on Power Electronics and Electrical Machines (PEMD), Edinburgh, United Kingdom, 2004.
 - [48] Pellegrino G., F. Villata P.G., Vagati A., *Design of direct-drive low-speed pm machines*, Industry Applications Conference, 38th IAS Annual Meeting, Vol. 2, pp. 1421-1428, 2003.
 - [49] Cros J., Viarouge P., *New structures of polyphase claw-pole machines*, IEEE Transactions on Industry Applications, Vol. 40, No. 1, pp. 113-120, 2004.

- [50] Maliti K., Sadarangani C., *Modelling magnetic noise in induction machines*, International Conference on Electrical Machines, pp. 406-410, Cambridge, U.K., 1997.
- [51] Huang S., Luo J., Leonardi F., Lipo T., *A comparison of power density for axial flux machines based on general purpose sizing equations*, IEEE Transactions on Energy Conversion, Vol. 14, No. 2, pp. 185-192, 1999.
- [52] Mbidì D., van der Westhuizen K., Wang R., Kamper M., Blom J., *Mechanical design considerations of a double stage axial-flux permanent-magnet machine*, Industry Applications Conference, Conference record of the 2000 IEEE, Vol. 1, pp. 198-201, 2000.
- [53] Cedrat, *www.cedrat.com*.
- [54] Surahammars Bruk, *Non-oriented fully processed electrical steels*.
- [55] Lundgren J., Rönqvist M., Värbrand P., *Optimeringslära*, Book, Studentlitteratur, ISBN 91-44-03104-1, 2003.
- [56] Bianchi N., Bolognani S., *Design optimisation of electrical motors by an adaptive model based optimisation technique*, 9th International Conference on Electrical Machines and Drives, Canterbury, 1999.

Glossary of symbols and acronyms

Symbols

a	number of parallel paths or conductors in the windings	-
A_{sl}	slot area	$[m^2]$
\hat{B}_δ	amplitude of the fundamental airgap flux density	$[T]$
B_n	radial component of the airgap flux density	$[T]$
B_m	maximum value of the airgap flux density	$[T]$
B_r	remanence flux density of the permanent magnet	$[T]$
B_{rc}	flux density in rotor cores (AFPM machine)	$[T]$
B_{ry}	flux density in the rotor yoke	$[T]$
B_{sat}	flux density in the saturated iron bridges of V-shaped PM motors	$[T]$
B_{sc}	flux density in stator core (AFPM machine)	$[T]$
b_{so}	stator slot opening	$[m]$
b_{ss1}	inner stator slot width	$[m]$
b_{ss2}	outer stator slot width	$[m]$
b_{t1}	small tooth width (when the teeth are irregularly distributed)	$[m]$
b_{t2}	large tooth width (when the teeth are irregularly distributed)	$[m]$
b_{ts}	stator tooth width	$[m]$
B_{ts}	flux density in a stator tooth	$[T]$
B_y	airgap flux density, y- (orthoradial) direction (AFPM machine)	$[T]$
B_z	airgap flux density, z- (axial) direction (AFPM machine)	$[T]$
d	denominator of the fraction used for the winding layout design	-
d_w	wire diameter	$[m]$
D	inner stator diameter	$[m]$
D_g	average diameter of the airgap (AFPM machine)	$[m]$
D_{rc}	outer rotor diameter	$[m]$
D_i	inner rotor diameter	$[m]$
D_o	outer stator diameter	$[m]$
E	fundamental of the induced voltage (RMS value)	$[V]$
\vec{E}_i	EMF phasor of conductor i	$[V]$
f	frequency	$[Hz]$
f_s	slot fill factor	-

H_m	coercive magnetic field intensity of the PM	$[A/m]$
h_{ry}	rotor yoke height	$[m]$
h_{ss}	stator slot height	$[m]$
h_{sw}	slot wedge height	$[m]$
I	line current	$[A]$
I_d	d-axis current	$[A]$
I_q	q-axis current	$[A]$
k	integer	-
k_C	Carter factor	-
k_{coil}	end-winding coefficient	-
J	current density	$[A/m^2]$
k_{cor}	correction factor for the calculation of the current loading	-
k_{leak}	correction factor for the airgap flux density calculation	-
$k_{leak\alpha}$	correction factor for the airgap flux density calculation	-
$k_{leaktooth}$	correction factor for the flux density in the teeth	-
k_{open}	ratio of the slot opening over the slot width	-
k_{w1}	fundamental winding factor	-
L	active length	$[m]$
L_d	d-axis inductance	$[H]$
l_{Fe}	length of the iron bridge (see figure 3.3)	$[m]$
l_i	airgap around the buried V-shaped permanent magnets	$[m]$
l_{iron}	width of a rotor iron piece	$[m]$
	of the tangentially-magnetized PM motor	$[m]$
L_l	leakage inductance	$[H]$
l_m	magnet thickness	$[m]$
L_{md}	d-axis magnetizing inductance	$[H]$
L_{mq}	q-axis magnetizing inductance	$[H]$
L_q	q-axis inductance	$[H]$
L_r	axial length of a rotor disc (AFPM machine)	$[m]$
l_{rc}	axial length of a rotor core (AFPM machine)	$[m]$
L_s	axial length of the stator (AFPM machine)	$[m]$
l_{sc}	axial length of the stator core (AFPM machine)	$[m]$
l_w	winding axial thickness (AFPM machine)	$[m]$
l_{1av}	average length of a stator turn	$[m]$
m_a	amplitude modulation ratio	-
m_1	number of phases	-

m_{tot}	total weight of the machine	[kg]
n	numerator of the fraction used for the winding layout design	-
n_l	number of layers of the winding	-
N_s	number of turns per phase	-
n_s	number of conductors per slot	-
p	number of poles	-
q	number of slots per pole per phase	-
Q_s	number of stator slots	-
R	resistance of one phase of the stator winding	[Ω]
R_i	inner radius of the toroidal core (AFPM machine)	[m]
\mathfrak{R}_m	reluctance of the PM	[At/Wb]
\mathfrak{R}_{gap}	airgap reluctance	[At/Wb]
R_o	outer radius of the toroidal core (AFPM machine)	[m]
s_a	conductor cross-section	[m ²]
S	vector describing a sequence of conductors of phase A	-
S_1	current loading	[A/m]
t	time	[s]
T	torque	[Nm]
T_{cu}	copper temperature	[°C]
V	external voltage	[V]
V_d	rectified voltage across the filter capacitor	[V]
W_{ewi}	end-winding inner radial thickness (AFPM machine)	[m]
W_{ewo}	end-winding outer radial thickness (AFPM machine)	[m]
W_w	effective length of the stator core (AFPM machine)	[m]
w_{Fe}	thickness of the iron bridge	[m]
w_m	PM length	[m]
X_{md}	armature reaction reactance	[Ω]
X_d	d-axis synchronous reactance	[Ω]
X_l	leakage reactance	[Ω]

Greek symbols

α	half pole angle in electrical degrees	[°]
α_v	"V" angle between the permanent magnets	[°]
β	angle between the d-axis and the current vector	[rad]
δ	airgap length	[m]
δ_{eq}	equivalent airgap	[m]

γ	current angle between the line current \underline{I} and the induced voltage \underline{E}	$[rad]$
λ	ratio of inner to outer stator radius (AFPM machine)	-
λ_1	specific permeance coefficient of the slot opening	-
λ_{le}	end connection leakage permeance (AFPM machine)	-
λ_{ld}	differential leakage permeance (AFPM machine)	-
μ_0	magnetic permeability of free space ($4\pi \cdot 10^{-7}$)	$[H/m]$
μ_r	relative magnet permeability	-
Φ	flux	$[Wb]$
Ψ_m	magnet flux linkage	$[Wb]$
ρ_{cu}	copper resistivity	$[\Omega m]$
σ	radial magnetic force density	$[N/m^2]$
τ	average pole pitch (AFPM machine)	$[m]$
τ_{dl}	differential leakage factor (AFPM machine)	-
τ_s	stator slot pitch	$[m]$
θ	angular coordinate	$[rad]$
ω	electrical angular frequency	$[Hz]$

Acronyms

AC	alternative current
AFPM	axial-flux permanent magnet
CW	concentrated windings
DC	direct current
DW	distributed windings
EMF	electro-motive force
FEM	finite element method
LCM	least common multiple
LSPM	line start permanent magnet
MMF	magneto-motive force
NdFeB	neodymium iron boron
RFPM	radial-flux permanent magnet
RMS	root mean square value
SMPM	surface-mounted permanent magnet
TFM	transverse-flux machine
PM	permanent magnet
p.u.	per unit
2D	two-dimensional
3D	three-dimensional

A Direct-driven machines manufacturers

Nowadays, low-speed direct-driven machines are both manufactured and sold. Some of the manufacturers are presented here.

A.1 Wind turbines

Enercon, www.enercon.de, wind turbines with synchronous wound-rotor generators.

Bergey, www.bergey.com, small wind turbines (≤ 10 kW) with RFPM generators.

Westwind, www.westwind.com.au, small wind turbines (≤ 20 kW) with outer-rotor RFPM generators.

Jeumont Industry, www.jeumont-framatome.com, 750 kW wind turbines with AFPM generators.

Zephyros, www.zephyros.com, 2 MW wind turbines with PM generators.

A.2 Other applications

Lynx Motion Technology, www.lynxmotiontechnology.com, modified AFPM motor manufacturer.

Kone, www.kone.com, elevators with different kinds of AFPM generators.

B Finite element methods simulations

All finite element simulations in this thesis were realized with the softwares Flux2D and Flux3D from Cedrat [53].

B.1 2D-FEM simulations

Magneto-static simulations

Magneto-static simulations are used for the verification of the flux density created by the permanent magnets in the airgap and the state of saturation in the teeth as well as the stator and rotor yokes. Figure B.1 shows an example of a meshed geometry used for the 2D simulations.

Simulations at no-load

No-load time-step simulations are used to verify the value of the induced voltage. An external electrical circuit is coupled to the meshed geometry. The coils representing the windings are connected to very high resistances.

Simulations at load

For time-step simulations at load conditions, the speed of the machine is set constant to 50 rpm. As for the no-load simulations, an external circuit is coupled to the meshed geometry. Thereby, current sources allow to define sinusoidal currents which are forced in the stator windings. With this

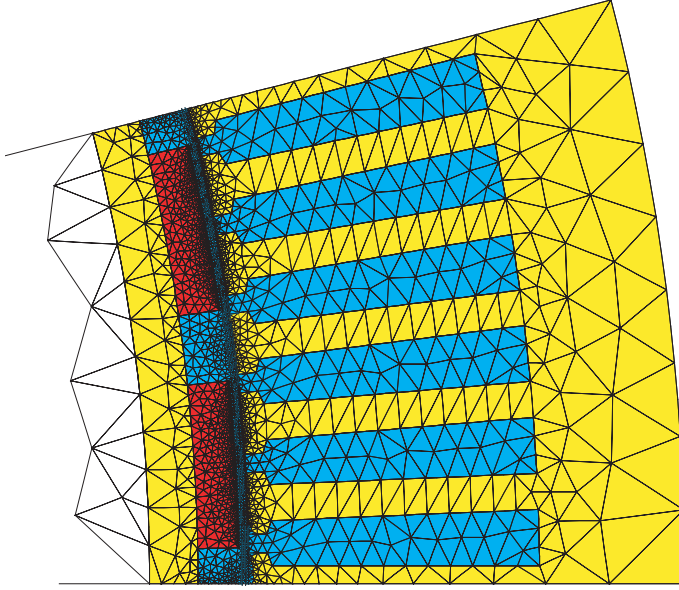


Figure B.1: Mesh of a 50-pole SMPM motor.

simulation, the torque and iron losses can be computed. The starting position has to be defined carefully in order to match the imposed currents.

Iron losses

In order to be able to compute the iron losses, the iron loss coefficients have to be calculated from the specific total loss data of the iron material, supplied by the lamination manufacturer. It was not possible to obtain this data for the iron material that is used in this thesis. Therefore, the iron loss coefficients of another iron material were used. This material has better magnetic properties, it saturates for higher values of the flux density. According to [54], a material with a magnetization curve that is better than another material, will also have higher iron losses. The iron losses that are calculated in this thesis may thus be overestimated.

The iron losses calculations with FEM simulations include the hysteresis, copper and excess losses, equation (B.1). They also take the

non-sinusoidal shape of the flux density into account :

$$P_{iron} = k_h B_m^2 k_f f + \frac{1}{T} \int_0^T \left[\sigma \frac{d^2}{12} \left(\frac{dB(t)}{dt} \right)^2 + k_e \left(\frac{dB(t)}{dt} \right)^{3/2} \right] k_f dt \quad (B.1)$$

where B_m is the maximum flux density in the concerned mesh element, f is the frequency, σ is the conductivity of the iron material ($4e6 (\Omega m)^{-1}$), d is the thickness of the lamination sheet (0.65 mm), k_h is the coefficient of hysteresis loss ($279.81 W.s/T^2/m^3$) and k_e is the coefficient of excess loss ($1.28 W.(s/T)^{3/2}/m^3$).

B.2 3D-FEM simulations

3D-FEM simulations are needed for the designs of the AFPM motors. Only static simulations are used since the time-step simulations demand a lot of time for both their implementation and computation. An example of a geometry used for the computations is given in figure B.2. Because of the symmetries, two poles are represented with only half the stator core and one rotor disc.

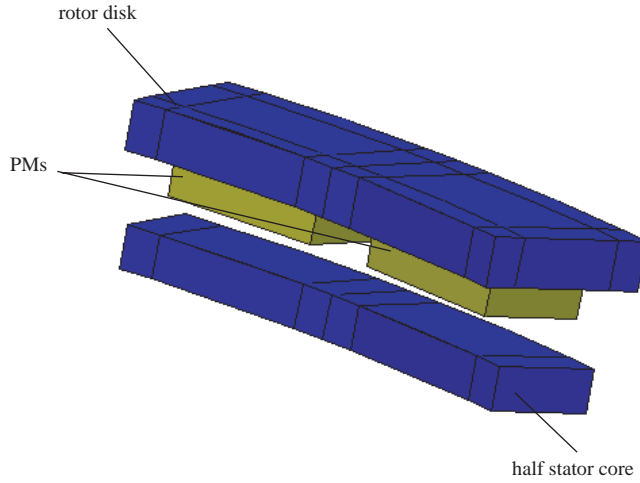


Figure B.2: Geometry of a 30-pole AFPM motor drawn in Flux3D.

C Optimization

Solving an optimization problem is to find the best possible values of the problem variables that lead to an optimum of the objective function (i.e. a minimum or a maximum value of the function). The objective function is the function that is to be optimized; it depends on the problem variables. These variables are subject to constraints and boundary conditions.

C.1 A simple example

The following example of an optimization problem illustrates the principles on a simple two-variables optimization problem. Thereby, let x_1 and x_2 be the two variables. The objective function to maximize is $x_1 + x_2$. The constraints consist of four inequalities:

$$x_1 + 3x_2 \leq 9$$

$$2x_1 + x_2 \leq 8$$

$$x_1 \geq 0$$

$$x_2 \geq 0$$

In this simple case with two variables and both a linear objective function and linear constraints, the solution can be found graphically (see figure C.1). It can be found that $x_1 = 3$ and $x_2 = 2$ gives the maximum value of the objective function which is 5.

C.2 Optimization program for the motor design

For the motor design, the optimization problem is much more complex:

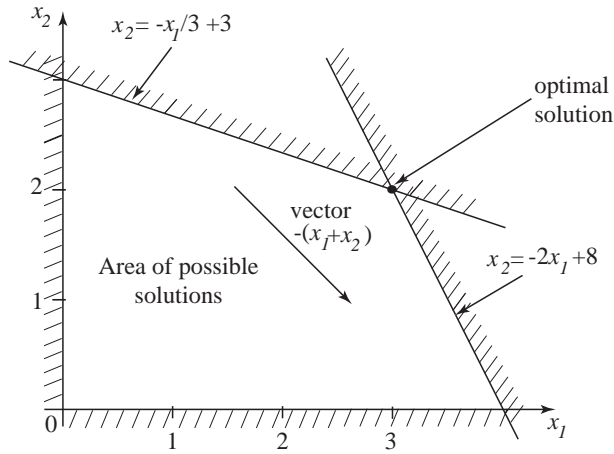


Figure C.1: Graphical solution of a two-variables optimization problem.

- There are 12 variables. Among these variables, two are integers, the number of slots and the number of poles, which also should be even.
- The objective function, in this case the motor weight, is a non-linear function of the variables.
- There are about 20 inequalities that describe the constraints. Some of them are non-linear.

C.2.1 How to deal with the integer variables

Solving an optimization problem with both integer and non-integer variables is tricky [55]. In order to avoid problems with integer variables, different values for p and Q_s are tested independently of the optimization problem, using a loop. The value of p is varied in a range between 20 and 80 in a loop exterior to the optimization program and is therefore a constant when solving the optimization problem. Q_s is chosen depending of the winding type that is tested (for example if $q = 1$ then Q_s is given by $Q_s = 3pq$).

C.2.2 How to deal with the non-linearities

Solving a non-linear optimization problem is also tricky. Different algorithms exist in this context. A description of some algorithms and optimization techniques including their advantages and drawbacks can be found in [56]. In Matlab, some algorithms are already implemented in the "optimization toolbox". The algorithm applied in the motor design is based on sequential quadratic programming. The method is described in detail in the Matlab help [39]. An initial solution is needed in order to start the optimization process. This can be seen as a drawback since the initial solution has to be guessed. However, as the algorithm proved to be stable and the Matlab toolbox very convenient, no other algorithms were investigated.

D Thermal study

The goal of the thermal study is to estimate the temperature in the windings. During the design procedure, this temperature is used to calculate the resistance of the windings.

A 62-pole SMPM motor with $q = 1$ is simulated in Flux2D. The simulation is static, magneto-thermal. Since the motor is placed under water in the considered application, no forced cooling is considered. The temperature of the water is assumed to be 25°C . The investigated motor geometry is displayed in figure D.1. The housing is surrounded by water at 25°C . A layer of air separates the stator iron and the housing. There is some air in the airgap as well.

The heat is created in the windings by the copper losses. Hence, heat sources are defined for each slot. They are constant and contribute equally to the total power loss (i.e. $700/Q_s \text{ W}$ each). The heat is then transmitted by conductivity from the copper into the stator iron. The transmission between the stator iron and the surrounding air is done by natural convection and conductivity. Most of the heat is then dissipated from the housing to the water by convection.

The conductivities and convective exchange coefficients used in the simulation are provided in tables D.1 and D.2 respectively.

The results of the simulation give a temperature in the winding of 81°C . The winding temperature for the calculation of the winding resistance was therefore set to 80°C . This value was compared with a measurement on a mixer with an induction motor. With 2.55 kW of total losses the winding temperature was measured to be 97°C , therefore the assumed temperature of the windings seems to be reasonable.

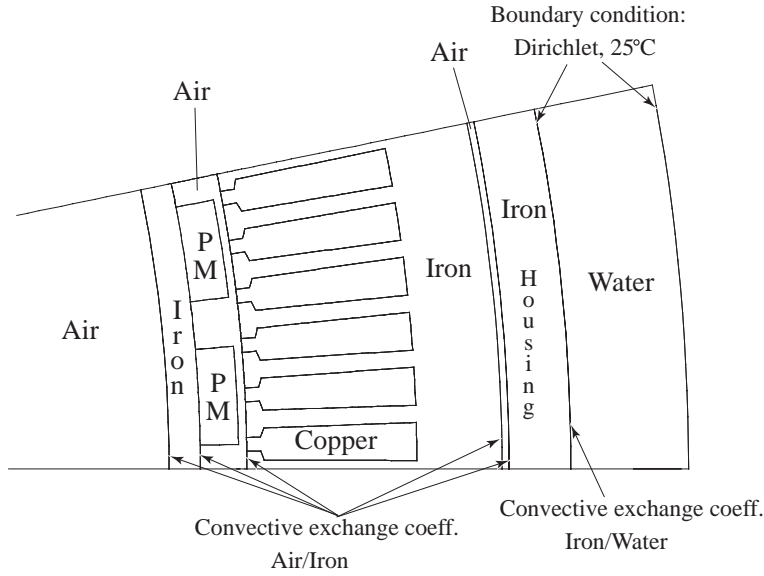


Figure D.1: Definition of the thermal features for FEM simulation.

Table D.1: Thermal conductivity of the materials.

Material	Thermal conductivity [W/mK]
Iron	43
Air	0.0287
Permanent magnet	9
Copper	385
Water	0.65

Table D.2: Convective exchange coefficient.

Materials	Convective exchange coefficient [W/m^2K]
Air/Iron	10
Iron/Water	50